



FEDERAL UNIVERSITY OF RIO GRANDE DO NORTE
CENTER OF TECHNOLOGY
GRADUATE PROGRAM IN CIVIL ENGINEERING

PEDRO HENRIQUE DOS SANTOS SILVA

NUMERICAL ANALYSIS OF A SEMI-INTEGRAL BRIDGE ABUTMENT
UNDERGOING CYCLIC LATERAL DISPLACEMENTS

NATAL/RN

2020

PEDRO HENRIQUE DOS SANTOS SILVA

NUMERICAL ANALYSIS OF A SEMI-INTEGRAL BRIDGE ABUTMENT
UNDERGOING CYCLIC LATERAL DISPLACEMENTS

Master's Thesis submitted to the Graduate Program in Civil Engineering of the Federal University of Rio Grande do Norte as a requirement for obtaining the degree of Master of Science in Civil Engineering.

Advisor: Prof. Yuri Daniel Jatobá Costa, Ph.D.
Co-Advisor: Prof. Carina Maia Lins Costa, Ph.D.

NATAL/RN

2020

Universidade Federal do Rio Grande do Norte - UFRN
Sistema de Bibliotecas - SISBI
Catalogação de Publicação na Fonte. UFRN - Biblioteca Central Zila Mamede

Pedro Henrique dos Santos Silva.

Numerical Analysis of a Semi-Integral Bridge Abutment
Undergoing Cyclic Lateral Displacements / Pedro Henrique dos
Santos Silva. - 2020.
114 f.: il.

Dissertação (mestrado) - Universidade Federal do Rio Grande do
Norte, Centro de Tecnologia, Programa de Pós-Graduação em
Engenharia Civil, Natal, RN, 2020.

Orientador: Prof. Dr. Yuri Daniel Jatobá Costa.

Coorientadora: Profa. Dra. Carina Maia Lins Costa.

1. Semi-integral bridge - Dissertação. 2. Bridge abutment -
Dissertação. 3. Soil-structure interaction - Dissertação. 4.
Cyclic loading - Dissertação. 5. Finite element method -
Dissertação. I. Costa, Yuri Daniel Jatobá. II. Costa, Carina Maia
Lins. III. Título.

RN/UF/BCZM

CDU 624.15

PEDRO HENRIQUE DOS SANTOS SILVA

NUMERICAL ANALYSIS OF A SEMI-INTEGRAL BRIDGE ABUTMENT
UNDERGOING CYCLIC LATERAL DISPLACEMENTS

Master's Thesis submitted to the Graduate Program in Civil Engineering of the Federal University of Rio Grande do Norte as a requirement for obtaining the degree of Master of Science in Civil Engineering.

EXAMINING COMMITTEE:

Prof. Yuri Daniel Jatobá Costa, Ph.D.
Advisor
Federal University of Rio Grande do Norte

Prof. Carina Maia Lins Costa, Ph.D.
Co-Advisor
Federal University of Rio Grande do Norte

Prof. Jorge Gabriel Zornberg, Ph.D.
Examining committee member
The University of Texas at Austin

Prof. José Antonio Schiavon, Ph.D.
Examining committee member
Aeronautics Institute of Technology

Natal/RN

September 18th, 2020

Dedicated to the memory of my father and
father-in-law.

ACKNOWLEDGMENTS

Firstly, I would like to thank my wife, parents, and sisters for their love, patience, encouragement, and support. Warm thanks to my wife's family for all kindness and confidence.

I would like to express my sincere gratitude to my advisors and friends, Prof. Yuri Costa, Ph.D., and Prof. Carina Costa, Ph.D., for their guidance and partnership. Their advice and lessons have been extremely important for the development and conclusion of this research, as well as in my life.

Special thanks to Prof. Jorge Zornberg, Ph.D., for the opportunity to know the research project which was the basis for this research.

I would also like to thank all my classmates for sharing the same feelings related to this journey.

Finally, I gratefully acknowledge the scholarship provided by the Coordinator for the Improvement of Higher Education Personnel, which made possible my full dedication to this research.

Hard work beats talent when talent fails to work hard.

Kevin Durant

ABSTRACT

Integral abutment bridges (IABs) and semi-integral abutment bridges (SIABs) are structural systems built without thermal expansion joints at the abutments. In view of this peculiar characteristic, the abutment undergoes combined movements of translation and rotation due to the expansion and contraction of the superstructure caused by temperature variations. Such behavior favors the increase of lateral earth pressures on the abutment and vertical displacements of the backfill surface, due to a complex soil-structure interaction mechanism associated with the cyclic lateral displacements of the abutment. The purpose of the present investigation is to assess the effects of cyclic lateral displacements on the response of the backfill-abutment system of a SIAB. A finite element model was developed and validated based on field data from an instrumented SIAB located in the State of Texas, USA. Field data were obtained from pressure cells installed against the abutment, and from temperature sensors positioned under the bridge superstructure. The soil stress-strain behavior was represented by a hyperbolic constitutive model, and the effects of expansion and contraction of the superstructure were simulated by prescribed horizontal displacements estimated from temperature variations measured by the temperature sensors. Predictions with the proposed numerical model were found to produce a good match with field data. After the validation phase, numerical simulations were performed to predict the daily and annual responses of the backfill-abutment system, as well as to analyze the influence of the completion season of the bridge construction, the pile foundation stiffness, and the lateral displacement amplitude on the response of the system. It was found that lateral earth pressures on the abutment and vertical displacements of the backfill surface increased with cycles. Lateral earth pressures presented a nonlinear distribution along the abutment height. The backfill experienced settlements near the abutment and heave at a certain distance from the abutment. The largest settlements occurred near the backfill-abutment interface and decreased with increasing distance from the abutment. While vertical displacements were not found to stabilize, earth pressures tended to reach a steady state after a few cycles. The completion season of the bridge construction influenced the vertical displacements but not the lateral earth pressures. Lateral earth pressures and vertical displacements were not affected by the pile foundation stiffness. However, the lateral displacement amplitude influenced both lateral earth pressures and vertical displacements.

Keywords: Semi-integral bridge. Bridge abutment. Soil-structure interaction. Cyclic loading. Finite element method.

RESUMO

Pontes de encontro integral (PEIs) e pontes de encontro semi-integral (PESIs) são sistemas estruturais construídos sem juntas de expansão térmica nos encontros. Dada essa característica, o encontro sofre movimentos combinados de translação e rotação devido à expansão e contração da superestrutura causada por variações de temperatura. Tal comportamento favorece o aumento das pressões laterais de terra no encontro e dos deslocamentos verticais da superfície do reaterro devido a um complexo mecanismo de interação solo-estrutura associado com os deslocamentos laterais cíclicos do encontro. O propósito da presente investigação é avaliar os efeitos de deslocamentos laterais cíclicos na resposta do sistema reaterro-encontro de uma PESI. Um modelo de elementos finitos foi desenvolvido e validado baseado nos dados de campo de uma PESI instrumentada e localizada no estado do Texas, EUA. Os dados de campo foram obtidos a partir de células de pressão instaladas no encontro e de sensores de temperaturas posicionados abaixo da superestrutura da ponte. O comportamento tensão-deformação do solo foi representado por um modelo constitutivo hiperbólico e os efeitos de expansão e contração da superestrutura foram simulados por deslocamentos horizontais prescritos estimados a partir das variações de temperatura medida pelos sensores de temperatura. Previsões com o modelo numérico proposto produziram boa correlação com dados de campo. Após a etapa de validação, simulações numéricas foram realizadas para prever a resposta diária e anual do sistema reaterro-encontro, bem como para analisar a influência da estação de conclusão da construção da ponte, da rigidez da fundação por estaca e da amplitude de deslocamento lateral na resposta do sistema. As pressões laterais de terra no encontro e os deslocamentos verticais da superfície do reaterro aumentaram com os ciclos. As pressões de terra apresentaram uma distribuição não linear ao longo da altura do encontro. O reaterro experimentou recalques próximo ao encontro e elevação em uma certa distância do encontro. Os maiores recalques ocorreram próximo a interface reaterro-encontro e diminuíram com o aumento da distância do encontro. Enquanto os deslocamentos verticais não foram estabilizados, as pressões de terra tenderam a atingir o estado estacionário após alguns ciclos. A estação de conclusão da construção da ponte influenciou os deslocamentos verticais, mas não as pressões de terra. As pressões de terra e os deslocamentos verticais não foram afetados pela rigidez da fundação por estaca. No entanto, a amplitude de deslocamento lateral influenciou as pressões de terra e os deslocamentos verticais.

Palavras-chave: Ponte semi-integral. Encontro de ponte. Interação solo-estrutura. Carregamento cíclico. Simulação numérica.

LIST OF TABLES

Table 3.1 –	TCP test results near the north abutment	43
Table 3.2 –	TCP test results near the south abutment	43
Table 4.1 –	Soil parameters used to validate the numerical model	56
Table 4.2 –	Structural parameters used to validate the numerical model	57
Table 5.1 –	Relationship between numerical predictions and field measurements for different values of R_{inter}	61
Table 6.1 –	Structural parameters of the sheet pile profiles	87
Table 6.2 –	Lateral displacement of the abutment from several sources in the technical literature	90

LIST OF FIGURES

Figure 2.1 –	Scheme of a conventional abutment bridge	19
Figure 2.2 –	Evolution of IABs and SIABs in the United States	21
Figure 2.3 –	Proportion of IABs and SIABs in the United Kingdom	21
Figure 2.4 –	Scheme of an integral abutment bridge	22
Figure 2.5 –	Scheme of a semi-integral abutment bridge	22
Figure 2.6 –	Problems experienced with IABs and SIABs in the United States	24
Figure 2.7 –	Illustration of the subsidence zone in the backfill-abutment system	25
Figure 2.8 –	Scheme of the stress-strain behavior of a material upon cyclic loading illustrating the phenomenon of ratcheting	26
Figure 2.9 –	Scheme of the backfill behavior in a typical cycle of lateral displacement of the abutment: a) passive condition; b) active condition	27
Figure 2.10 –	Scheme of backfill shape: a) before cyclic loading; b) after cyclic loading	27
Figure 2.11 –	Scheme of the three-element model illustrating the concept of soil granular flow	28
Figure 2.12 –	Cyclic stress variations in the soil elements: a) element A; b) element B	29
Figure 2.13 –	Stress-strain behavior and shapes of elements A and B	30
Figure 2.14 –	Scheme of the stress-strain behavior of a material upon cyclic loading illustrating the elastic shakedown	31
Figure 2.15 –	Scheme of the stress-strain behavior of a material upon cyclic loading illustrating the plastic shakedown	32
Figure 3.1 –	“Mack Creek” Bridge location	40
Figure 3.2 –	Schematic view of the bridge: a) plan view; b) elevation view	41
Figure 3.3 –	Photographs of the bridge after construction: a) top view; b) bottom view	42
Figure 3.4 –	Backfill material as used in the field	44
Figure 3.5 –	Triaxial setup used in the testing program	45
Figure 3.6 –	Results of the triaxial tests: a) stress x strain curves; b) volumetric strain x axial strain curves	46
Figure 3.7 –	Triaxial specimen at failure	47

Figure 3.8 –	Schematic view of the position of the devices in the bridge: a) plan view; b) elevation view	48
Figure 3.9 –	Devices used in the field monitoring: a) pressure cell; b) datalogger	49
Figure 3.10 –	Devices installed in the field: a) pressure cells; b) dataloggers	49
Figure 3.11 –	Lateral earth pressures on the north abutment and ambient air temperatures	50
Figure 3.12 –	Lateral earth pressures on the south abutment and ambient air temperatures	50
Figure 4.1 –	Numerical model geometry (dimensions in meters)	51
Figure 4.2 –	Zoom of the numerical model geometry in the region of the abutment (dimensions in meters)	52
Figure 4.3 –	Scheme of the representation of the effects of loads and displacements on the abutment-pile cap system	54
Figure 4.4 –	Finite element mesh used in the numerical simulations	55
Figure 4.5 –	Ambient air temperatures recorded on July 14, 2017	58
Figure 5.1 –	Prescribed horizontal displacements used to validate the numerical model	59
Figure 5.2 –	Comparison between field and numerical lateral earth pressures	60
Figure 5.3 –	Dispersion of the lateral earth pressures	61
Figure 5.4 –	Distributions of maximum lateral earth pressures along the abutment height for selected daily cycles	62
Figure 5.5 –	Distributions of minimum lateral earth pressures along the abutment height for selected daily cycles	62
Figure 5.6 –	Shadings of relative shear stress in the backfill for a typical daily cycle: a) passive condition; b) active condition	64
Figure 5.7 –	Arrows of resultant displacement in the backfill for a typical daily cycle: a) passive condition; b) active condition	65
Figure 5.8 –	Shadings of accumulated deviatoric strain (in %) in the backfill at the end of selected daily cycles: a) 1st cycle; b) 33rd cycle; c) 66th cycle; d) 100th cycle	66
Figure 5.9 –	Lateral earth pressure coefficients for daily cycles	67
Figure 5.10 –	Vertical displacement profiles of the backfill surface along the distance from the abutment for selected daily cycles	68

Figure 5.11 –	Vertical displacements at the top of the backfill-abutment interface for daily cycles	69
Figure 5.12 –	Arrows of accumulated resultant displacement in the backfill after the daily cyclic lateral loading	70
Figure 5.13 –	Shadings of accumulated compressive volumetric strain (in %) in the backfill at the end of selected daily cycles: a) 1st cycle; b) 33rd cycle; c) 66th cycle; d) 100th cycle	71
Figure 5.14 –	Distributions of maximum lateral earth pressures along the abutment height for selected annual cycles	73
Figure 5.15 –	Distributions of minimum lateral earth pressures along the abutment height for selected annual cycles	73
Figure 5.16 –	Shadings of relative shear stress in the backfill for a typical annual cycle: a) passive condition; b) active condition	74
Figure 5.17 –	Arrows of resultant displacement in the backfill for a typical annual cycle: a) passive condition; b) active condition	74
Figure 5.18 –	Shadings of accumulated deviatoric strain (in %) in the backfill at the end of selected annual cycles: a) 1 st cycle; b) 33 rd cycle; c) 66 th cycle; d) 100 th cycle	75
Figure 5.19 –	Lateral earth pressure coefficients for annual cycles	76
Figure 5.20 –	Lateral earth pressure coefficients during the cyclic process for selected annual cycles	77
Figure 5.21 –	Vertical displacement profiles of the backfill surface along the distance from the abutment for selected annual cycles	78
Figure 5.22 –	Vertical displacements at the top of the backfill-abutment interface for annual cycles	78
Figure 5.23 –	Shadings of accumulated compressive volumetric strain (in %) in the backfill at the end of selected annual cycles: a) 1 st cycle; b) 33 rd cycle; c) 66 th cycle; d) 100 th cycle	79
Figure 5.24 –	Arrows of accumulated resultant displacement in the backfill after the annual cyclic lateral loading	80
Figure 6.1 –	Schemes of annual cycles of lateral displacements of the abutment for all analyzed scenarios: a) spring; b) autumn; c) summer; d) winter	82

Figure 6.2 –	Distributions of maximum lateral earth pressures along the abutment height for the analyzed scenarios after 50 annual cycles	83
Figure 6.3 –	Maximum lateral earth pressure coefficients for annual cycles considering the analyzed scenarios	83
Figure 6.4 –	Vertical displacement profiles of the backfill surface along the distance from the abutment for the analyzed scenarios after 50 annual cycles	84
Figure 6.5 –	Vertical displacements on the top of the backfill-abutment interface for annual cycles considering the analyzed scenarios	85
Figure 6.6 –	Distributions of maximum lateral earth pressures along the abutment height after 50 annual cycles considering the selected values of foundation stiffness	87
Figure 6.7 –	Maximum lateral earth pressure coefficients for annual cycles considering the selected values of foundation stiffness	88
Figure 6.8 –	Vertical displacement profiles of the backfill surface along the distance from the abutment for the different values of foundation stiffness after 50 annual cycles	89
Figure 6.9 –	Vertical displacements on the top of the backfill-abutment interface for annual cycles considering the different values of foundation stiffness ...	89
Figure 6.10 –	Distributions of maximum lateral earth pressures along the abutment height for the selected values of δ_h/h after 50 cycles of lateral displacements of the abutment	91
Figure 6.11 –	Shadings of deviatoric strains (in %) in the backfill accumulated after 50 cycles of δ_h/h equal to: a) 1 mm; b) 2 mm; c) 3 mm; d) 4 mm; e) 5 mm	92
Figure 6.12 –	Maximum lateral earth pressure coefficients with cycles considering the selected values of δ_h/h	93
Figure 6.13 –	Variation of the maximum lateral earth pressure coefficients at the steady state with the relative lateral displacements	94
Figure 6.14 –	Vertical displacement profiles of the backfill surface along the distance from the abutment for the different values of δ_h/h after 50 cycles	95
Figure 6.15 –	Vertical displacements on the top of the backfill-abutment interface with cycles considering the different values of δ_h/h	95

Figure 6.16 – Variation of the vertical displacement on the top of the backfill-abutment interface with the relative lateral displacements after 50 cycles	97
Figure 6.17 – Shadings of compression volumetric strains (in %) in the backfill accumulated after 50 cycles of δ_h/h equal to: a) 1 mm; b) 2 mm; c) 3 mm; d) 4 mm; e) 5 mm	98

CONTENTS

1	INTRODUCTION	16
2	LITERATURE REVIEW	19
2.1	Conventional abutment bridge	19
2.2	Integral and Semi-integral abutment bridge	20
2.3	Backfill behavior during cyclic lateral displacements of the abutment	25
2.4	Previous studies on the response of backfill materials upon cyclic loadings	32
3	THE “MACK CREEK” BRIDGE PROJECT	40
3.1	Bridge location and description	40
3.2	Subsoil characteristics	42
3.3	Backfill characteristics	44
3.4	Field instrumentation and monitoring	48
4	NUMERICAL MODELING CHARACTERISTICS	51
4.1	Numerical model description	51
4.2	Material properties	55
4.3	Approach for calculating the prescribed horizontal displacements	57
5	BACKFILL-ABUTMENT SYSTEM NUMERICAL RESPONSE	59
5.1	Numerical model validation	59
5.2	Analysis of the daily cyclic response	61
5.3	Analysis of the annual cyclic response	71
6	PARAMETRIC ANALYSIS	81
6.1	Bridge completion season	81
6.2	Sheet pile stiffness	86
6.3	Lateral displacement amplitude	90
7	LESSONS LEARNED FROM THE SIAB NUMERICAL INVESTIGATION	99
8	CONCLUDING REMARKS	100
8.1	Summary	100
8.2	Recommendations for future research	103
	REFERENCES	104

1 INTRODUCTION

Integral abutment bridges (IABs) and semi-integral abutment bridges (SIABs) have recently become an alternative adopted in several countries to transpose natural obstacles, such as rivers and lakes, and/or artificial obstacles, such as highways and railways. The increase in the number of IABs and SIABs has been attributed to a better understanding and acceptability of their benefits, as well as the acquired knowledge on design and construction. However, the use of IABs and SIABs' concepts is not yet widespread due to some issues regarding the long-term behavior and the involved complex soil-structure interaction mechanism.

IABs and SIABs are structural systems that have the superstructure totally integrated to the abutment. The main benefit of IABs and SIABs is the reduction of construction and maintenance costs because of the absence of thermal expansion joints. However, the lack of expansion joints causes variations in the length of the superstructure to be integrally transferred to the abutment and, consequently, to the retained backfill behind it. Such behavior favors the increase of lateral earth pressures on the abutment and vertical displacements on the backfill surface, due to the complex soil-structure interaction mechanism associated with the cyclic lateral displacement of the abutment.

Understanding the behavior of the backfill behind the abutment of IABs and SIABs under cyclic horizontal displacements is essential to properly address the involved soil-structure interaction mechanisms. Several studies in the technical literature have observed a tendency of increasing lateral earth pressures on the abutments due to cyclic lateral displacements. A tendency of increasing vertical displacements on the backfill surface with cyclic lateral displacements has also been noted, which includes downward vertical displacement (settlement) near the abutment and upward vertical displacement (heave) at a distance from the abutment (AL-QARAWI; LEO; LIYANAPATHIRANA, 2020; BANKS; BLOODWORTH, 2018; BREÑA et al., 2007; CLAYTON; XU; BLOODWORTH, 2006; ENGLAND; TSANG; BUSH, 2000; FROSCHE; LOVELL, 2011; GABRIELI; ZORZI; WAN, 2015; KIM; LAMAN, 2012; KIM et al., 2014; RAVJEE, et al., 2018; TATSUOKA et al., 2009; ZORZI; ARTONI; GABRIELI, 2017).

Although the response of the backfill-abutment system upon cyclic lateral displacements of the abutment has been investigated by several studies in the technical literature, additional aspects of interest, which were not significantly explored, can be identified. Most investigations have been related to IABs while studies involving SIABs are rather limited. Understanding the behavior of the backfill-abutment system of SIABs upon

cyclic loadings contributes to the improvement of knowledge about this structural system, which can be used as an alternative for IABs.

Acknowledged research gaps on the behavior of IABs and SIABs include studying the influence of: (1) the season when the construction of the bridge was completed, (2) the bridge foundation stiffness, and (3) the amplitude of the abutment's lateral displacements. Relevant issues regarding the design, construction, and service life of IABs and SIABs can be addressed from consistent analyses of these topics. Identifying the best season to complete the bridge construction is important to reduce the lateral earth pressures on the abutment and/or the vertical displacements on the backfill surface. The effect of the bridge foundation stiffness on the backfill-abutment system performance can contribute to identifying the best type of foundation (rigid or flexible) for the backfill-abutment system. The behavior of the backfill-abutment system upon different lateral displacement amplitudes allows to understand variations of lateral earth pressures on the abutment and vertical displacement on the backfill surface with lateral displacement amplitudes, as well as can even result in length limitations for the bridge superstructure.

The purpose of the present work is to assess the effects of cyclic lateral displacements on the response of the backfill-abutment system of an instrumented SIAB located near the city of Palestine, Texas, United States of American. Specific objectives of this investigation are as follows:

- a) Developing and validating a finite element model for the backfill-abutment system upon imposed cyclic lateral displacements at the abutment.
- b) Analyzing the response of the backfill-abutment system upon daily cyclic lateral displacements at the abutment.
- c) Analyzing the response of the backfill-abutment system upon annual cyclic lateral displacements at the abutment.
- d) Assessing the influence of the period of the year (season) of completion of the bridge construction on the response of the backfill-abutment system upon imposed cyclic lateral displacements at the abutment.
- e) Investigating the effect of the bridge foundation stiffness on the response of the backfill-abutment system upon imposed cyclic lateral displacements at the abutment.
- f) Studying the impact of the amplitude of lateral displacements on the response of the backfill-abutment system upon imposed cyclic lateral displacements at the abutment.

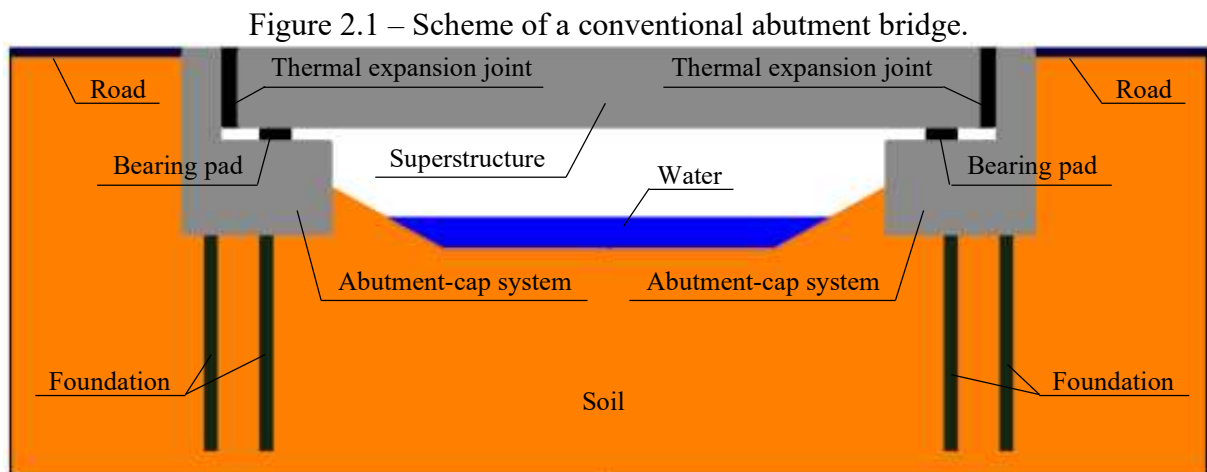
This thesis consists of eight sections. Following the introductory section (Section 1), the remainder of the thesis includes the following:

- Section 2 - Literature Review: This section presents a brief description on conventional abutment bridges, IABs, and SIABs. It also addresses previous studies on the backfill behavior during cyclic lateral displacements of the abutment and on the response of backfill materials upon cyclic loading.
- Section 3 - The “Mack Creek” Bridge Project: This section presents a brief description and the location of the bridge evaluated in this research, as well as the subsoil and backfill characteristics, and field instrumentation and monitoring.
- Section 4 – Numerical Model Characteristics: This section describes the numerical model, the material properties, and the approach adopted to calculate the prescribed horizontal displacements used to represent the effects of expansion and contraction of the superstructure on the abutment due to temperature changes.
- Section 5 – Backfill-Abutment System Numerical Response: This section presents the numerical model validation and analyses of the daily and annual cyclic responses of the backfill-abutment system.
- Section 6 – Parametric Analysis: This section presents analyses on the influence of the completion season of the bridge construction, foundation stiffness, and displacement amplitude on the response of the backfill-abutment system upon imposed cyclic lateral displacements.
- Section 7 – Lessons learned from the SIAB numerical investigation: This section presents a brief discussion about some aspects of interest regarding the SIAB design.
- Section 8 – Concluding Remarks: This section presents a summary of the conducted research, the main findings, and suggestions for future studies.

2 LITERATURE REVIEW

2.1 Conventional abutment bridge

Conventional abutment bridges are structural systems built with thermal expansion joints, which are installed between the superstructure and the abutment, and bearing pads, which are placed between the superstructure and the substructure. Expansion joints and bearing pads can accommodate horizontal displacements of the superstructure due to thermal, shrinkage, and creep effects, preventing the abutment and the substructure from being significantly affected by these displacements (OLSON et al., 2013; WALTER, 2018). Figure 2.1 shows a scheme of a conventional abutment bridge.



Source: Elaborated by the author (2020).

Walter (2018) relates some advantages that have been attributed to conventional abutment bridges based on “idealized” conditions that often do not exist in actual bridge systems:

- Primarily vertical loads from the superstructure are transferred to the abutment and substructure.
- The development of secondary loads derived from expansion and contraction of the superstructure due to temperature changes are minimized with the use of thermal expansion joints.
- Experience in the design and construction for these types of bridges is widespread.

Despite these apparent benefits, several disadvantages have been reported regarding conventional abutment bridges (ABENDROTH; GRIMANN, 2005; ARSOY; BARKER; DUNCAN, 1999; HASSIOTIS et al., 2006; LAMAN; KIM, 2009):

- Bearing pads and thermal expansion joints increase the initial costs with construction materials, as well as the maintenance costs of the bridge.
- Thermal expansion joints are susceptible to deterioration and damage due to environmental conditions, defrost services, and traffic.
- Although thermal expansion joints allow free expansion and contraction of the superstructure, foreign objects or debris can fill joint voids and block the superstructure movement, resulting in loads that were not initially considered in the design.
- Bearing pads are highly susceptible to corrosion and replacing them is expensive and complex.

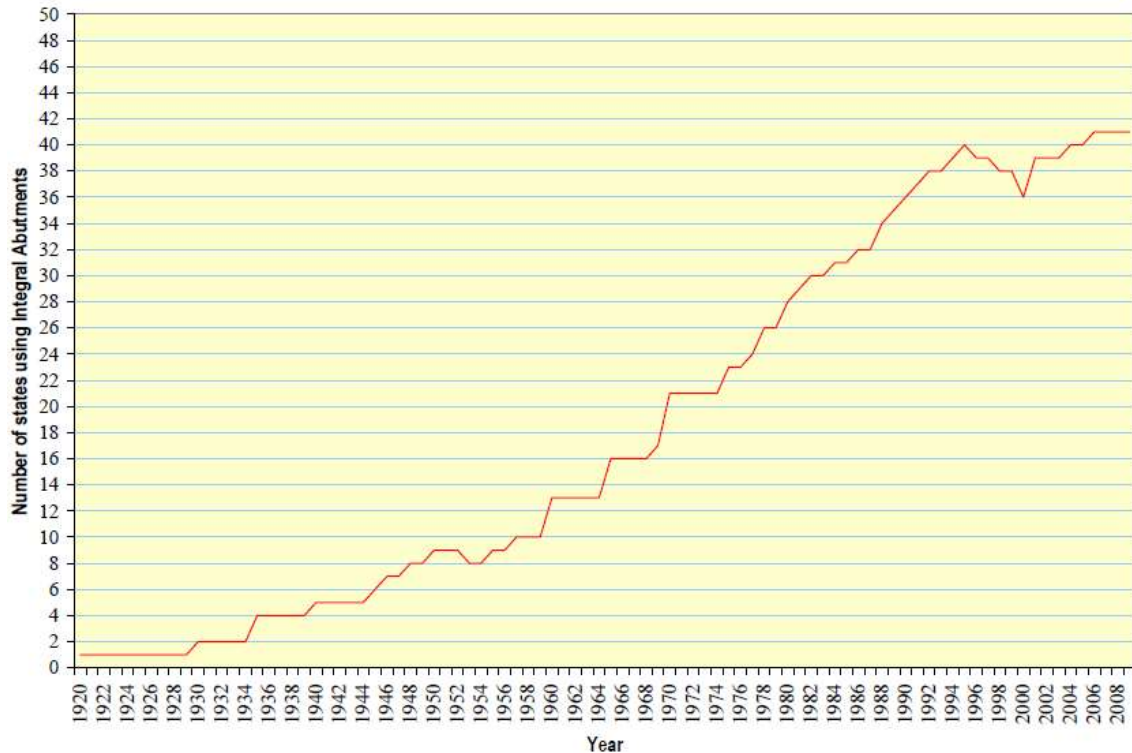
Although conventional abutment bridges have been quite common in engineering practice, other types of structural systems have been developed to overcome the disadvantages of using thermal expansion joints and bearing pads. In this context, the concept of integral abutment bridge (IABs) and semi-integral abutment bridges (SIABs) have emerged and have recently become an alternative to the use of conventional abutment bridges (AHN et al., 2011; AL-ANI et al., 2018; BURKE JR, 2009; DAVID; FORTH, 2011; FRANCHIN; PINTO, 2014; GANGONE et al., 2012; KANG et al., 2018; MARURI; PETRO, 2005; WHITE, 2007; ZORDAN; BRISEGHIELLA; LAN, 2011).

2.2 Integral and semi-integral abutment bridge

The beginning of the use of IABs and SIABs dates from the late 1930s and early 1940s, and, since then, it has increased along the years (BURKE JR, 2009). According to Maruri and Petro (2005), a survey conducted in 2004 showed that there were approximately 13,000 IABs and SIABs in the United States, of which approximately 9,000 are IABs and approximately 4,000 are SIABs. In Canada, several provinces have reported good experiences with IABs and SIABs (BAKEER et al., 2005; KUNIN; ALAMPALLI, 2000). In Europe, the experience with IABs and SIABs is significantly less, but the recent gains have been positive, which have led towards making IABs and SIABs a larger percentage of all newly constructed bridges (WHITE, 2007). In Asia and Oceania, despite limited experience, excellent performances in service of IABs and SIABs have been reported with no maintenance problems in the past decade (LAN,

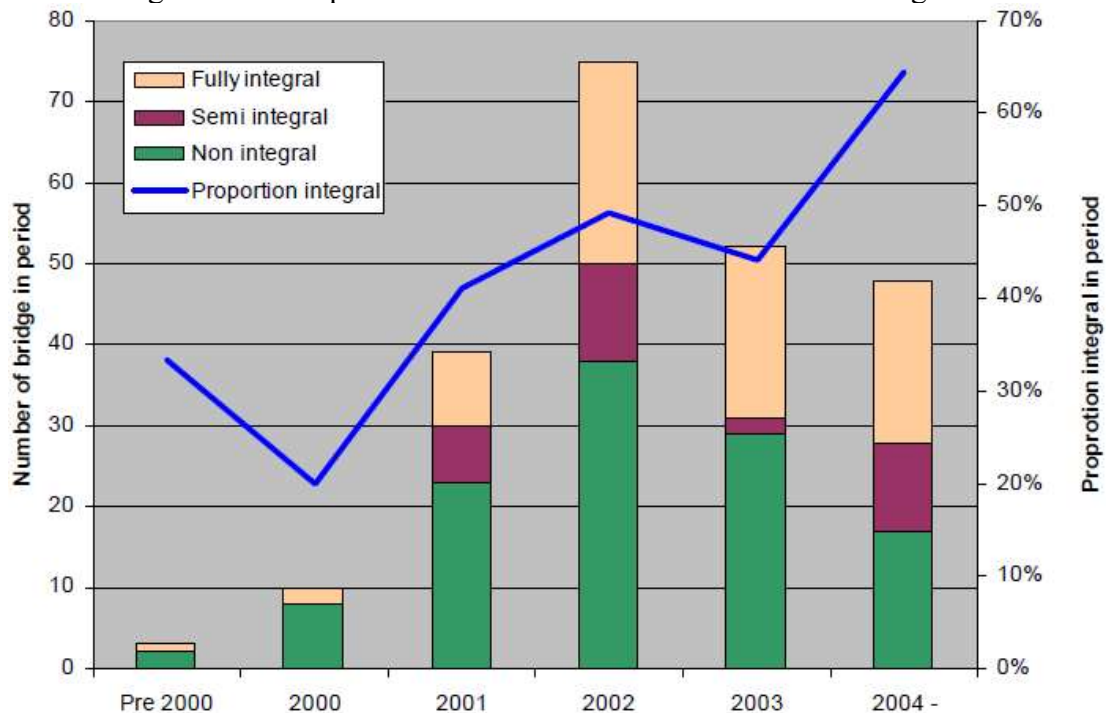
2012). Figure 2.2 shows the evolution of the number of IABs and SIABs in the United States, and Figure 2.3 shows the proportion of IABs and SIABs in the United Kingdom.

Figure 2.2 – Evolution of IABs and SIABs in the United States.



Source: Paraschos and Amde (2011).

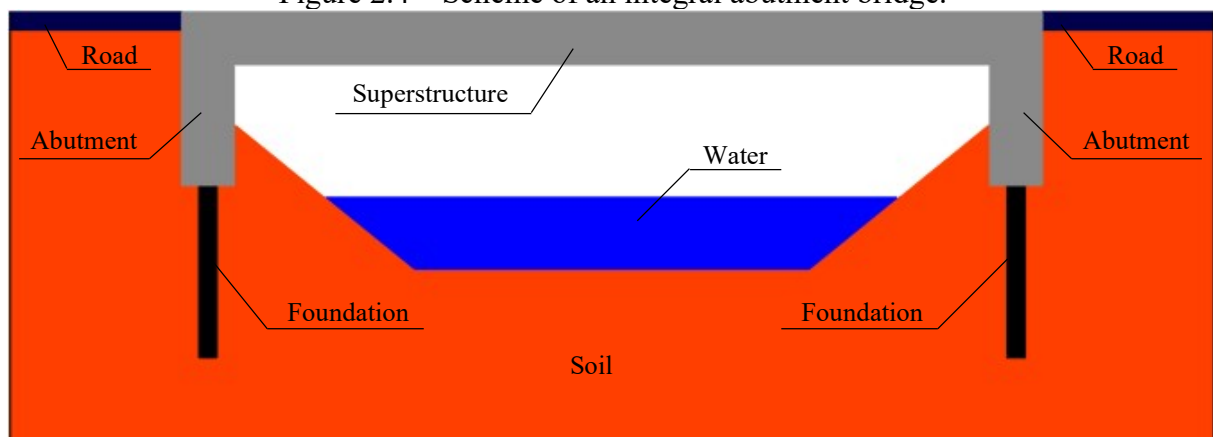
Figure 2.3 – Proportion of IABs and SIABs in the United Kingdom.



Source: Iles (2006).

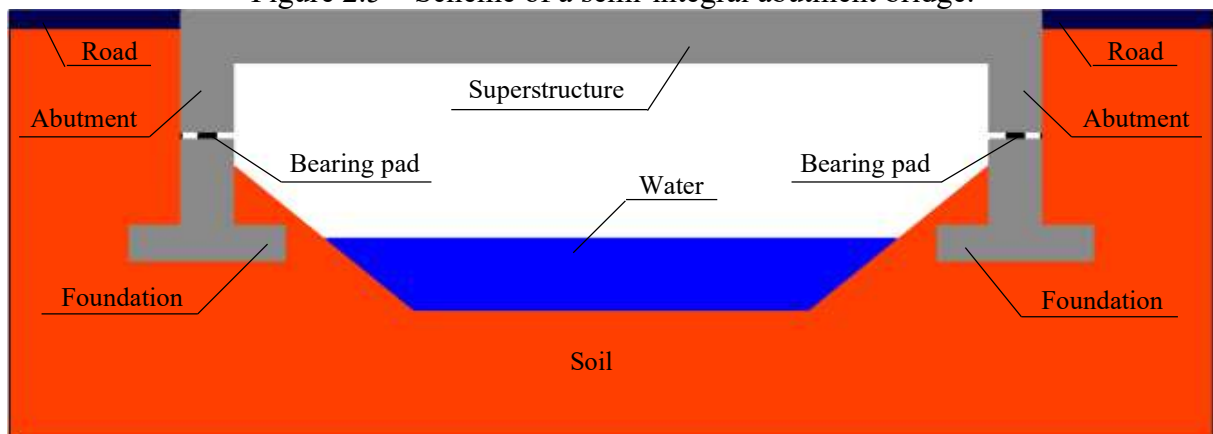
The difference between IABs and SIABs is related to the method of integration between the superstructure, abutment, and substructure of the bridge. IABs are structural systems of single or multiple spans, normally supported by flexible foundations, constructed without thermal expansion joints, and bearing pads. In other words, a structural connection between the superstructure, abutment, and substructure exists, resulting in a fully integrated continuous system. On the other hand, SIABs are structural systems of single or multiple spans, normally supported by rigid foundations, built without thermal expansion joints, but with bearing pads. In this case, there is a structural connection between the superstructure and the abutment, which results in a continuous system that is not integrally connected to the substructure (AL-ANI et al., 2018; ARSOY; DUNCAN; BARKER, 2004; BURKE JR, 2009; HUSAIN; BAGNARIOL, 1996, 1999; KIM et al., 2014; STEINBERG; SARGAND; BETTINGER, 2004; WHITE, 2007). Figures 2.4 and 2.5 show schemes of an integral abutment bridge and a semi-integral abutment bridge, respectively.

Figure 2.4 – Scheme of an integral abutment bridge.



Source: Elaborated by the author (2020).

Figure 2.5 – Scheme of a semi-integral abutment bridge.



Source: Elaborated by the author (2020).

Several benefits related to the use of IABs and SIABs have been listed in the technical literature (ARSOY; DUNCAN; BARKER, 2004; BURKE JR, 2009; HOPPE; GOMEZ, 1996; MARURI; PETRO, 2005; MISTRY, 2005; SOLTANI; KUKRETI; 1992; YANG; WOLDE-TINSAE; GREIMANN, 1985):

- lower construction and maintenance costs;
- improved seismic performance;
- foundation support with less piles;
- simple and rapid construction;
- greater achievable end-span ratios;
- smooth, uninterrupted deck of the bridge (which is aesthetically pleasing and improves vehicular riding quality);
- simplified widening and replacement;
- better live load distribution, reducing superstructure service load stresses.

Among all, the main benefit is the reduction of construction and maintenance costs related to the absence of thermal expansion joints. Frequent maintenance programs are required for thermal expansion joints due to their low durability, as compared to other bridge components. Moreover, no thermal expansion joint means no problem related to malfunctioning joints. Chemical agents used in the defrost services and heavy vehicles can cause damage to bridge with malfunctioning joints, reducing the ride quality. Therefore, elimination of thermal expansion joints has directly been associated not only with the reduction in the total cost of the bridge but also with the improvement in the ride quality (AHN et al., 2011; AL-ANI et al., 2018; AL-QARAWI; LEO; LIYANAPATHIRANA, 2020; LAN et al., 2017; MURPHY; YARNOLD, 2018; OESTERLE; TABATABAI, 2014).

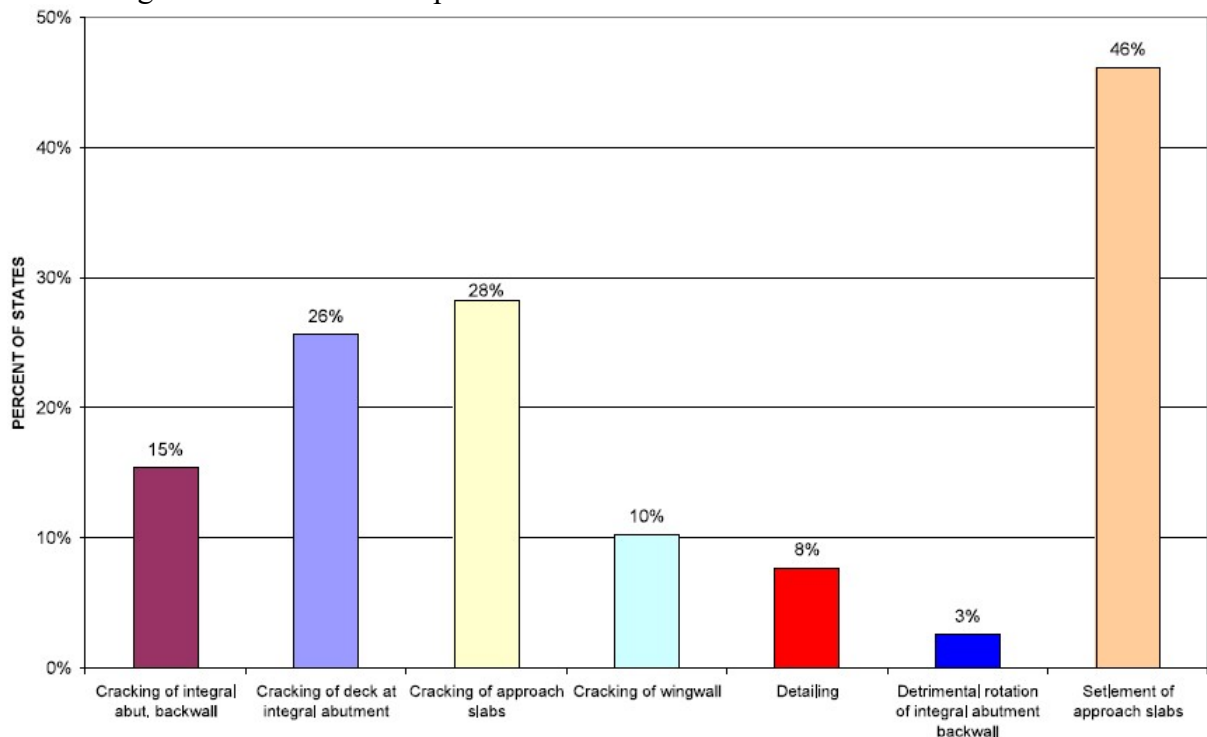
Despite the several benefits, some limitations related to the use of IABs and SIABs have been listed in the technical literature as presented below (BURKE JR 2009):

- The foundation can be subjected to greater horizontal and flexural stresses, which can result in the formation of plastic hinges that may limit the flexural resistance of piles.
- The bridge length must be limited to avoid high horizontal deformations of the bridge superstructure due to temperature changes.
- Extreme skews (greater than 30°) should not be used.
- The abutment can be subjected to an increase of lateral earth pressures due to cyclic lateral displacements.

- The approach slab and road can be subjected to downward (settlement) and upward (heave) vertical displacements due to backfill deformations because of cyclic lateral displacements of the abutment.
- Current bridge design mostly depends on idealizations and simplifications of soil-structure interaction relationships, which probably do not accurately reflect field conditions.

A great source of concern with IABs and SIABs is the complex soil-structure mechanisms associated with cyclic lateral displacements of the bridge abutment, which can result in unacceptable lateral earth pressures on the abutment and unacceptable vertical displacements of the backfill surface (BURKE JR, 2009). Walter (2018) states that backfill performance can have a major impact on the performance of IABs and SIABs throughout the entire design life. Maruri and Petro (2005) conducted a survey and compiled information regarding backfill requirements for IABs and SIABs in the United States. The results showed that settlement and cracking of approach slabs have been the main issues with IABs and SIABs (Figure 2.6). Both situations can be caused by inadequate compaction of the backfill.

Figure 2.6 – Problems experienced with IABs and SIABs in the United States.

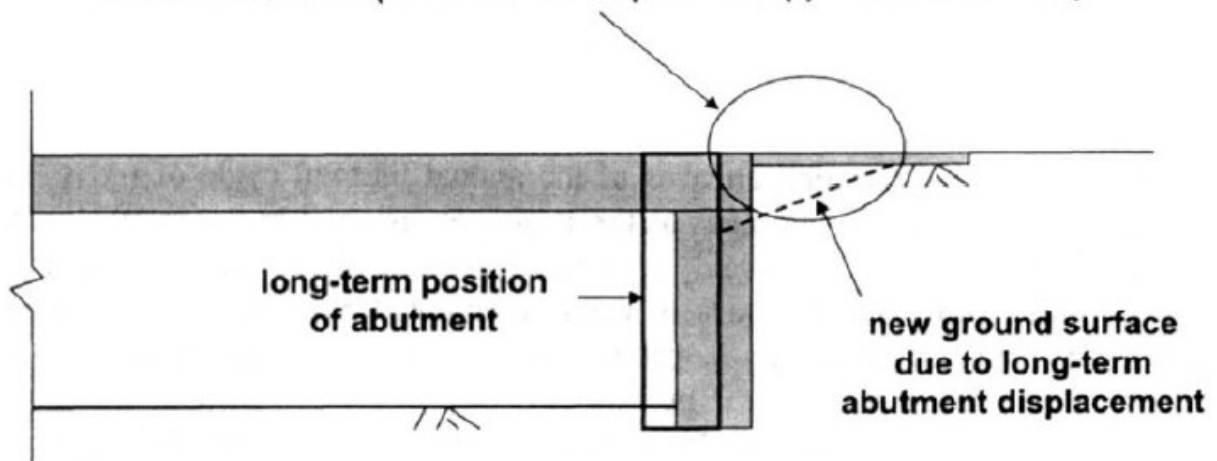


Source: Maruri and Petro (2005).

According to Walter (2018), approach slabs and roads have received important attention in recent years due to deformations in the backfill upon cyclic lateral displacements

of the abutment. Horvath (2004) discussed the formation of a subsidence zone below approach slabs and road. Its development is associated with a soil wedge that slips towards the abutment during the bridge contraction in winter periods and does not return to its initial position during the bridge expansion in summer periods due to the plastic behavior of the soil. Figure 2.7 illustrates the location of the subsidence zone in the backfill-abutment system.

Figure 2.7 – Illustration of the subsidence zone in the backfill-abutment system.
subsidence zone (and void development if approach slab used)



Source: Horvath (2004).

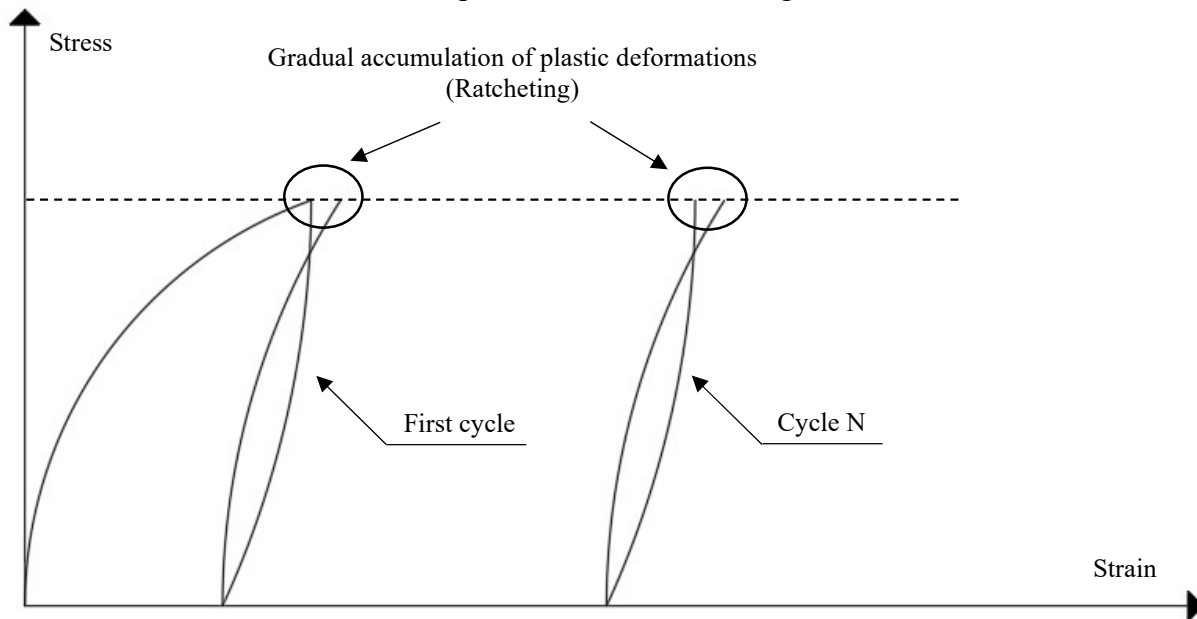
Another characteristic represented in Figure 2.7 is the inward position of the abutment in the long-term in relation to the originally constructed position. Walter (2018) attributed this position change to the increase in lateral earth pressures on the abutment upon cyclic lateral displacements from seasonal temperature fluctuations. However, this change in position can be better related to the plastic behavior of the soil (HOVARTH, 2004).

2.3 Backfill behavior during cyclic lateral displacements of the abutment

Recently, several authors have attributed the behavior of granular backfills of IABs and SIABs upon cyclic loading to a phenomenon called “ratcheting” (AL-QARAWI; LEO; LIYANAPATHIRANA, 2020; ALONSO-MARROQUÍN; HERRMANN, 2004; ARGYROUDIS et al., 2016; BLOODWORTH et al., 2012; CARISTO; BARNES; MITOULIS, 2018; CIVJAN et al., 2013; ENGLAND; TSANG; BUSH, 2000; FROSCHE; LOVELL, 2011; GABRIELI; ZORZI; WAN, 2015; JIA; KONG, 2015; MITOULIS et al., 2016; TATSUOKA et al., 2009; ZORZI; ARTONI; GABRIELI, 2017). In continuous mechanics, ratcheting is the gradual accumulation of plastic deformations which arises from cyclic mechanical or thermal

stresses (BREE, 1967; GABRIELI; ZORZI; WAN, 2015; HOULSBY et al., 2017; JIA; KONG, 2015; ROESLER; HARDERS; BAEKER, 2007; ZHENG et al., 2017; ZORZI; ARTONI; GABRIELI, 2017). The extent of ratcheting is influenced by several factors, such as load condition, mean stress, stress amplitude, stress ratio, load history, plastic slip, dislocation movement, and container deformation (ABDOLLAHI; CHAKHERLOU, 2019). Figure 2.8 illustrates the phenomenon of ratcheting.

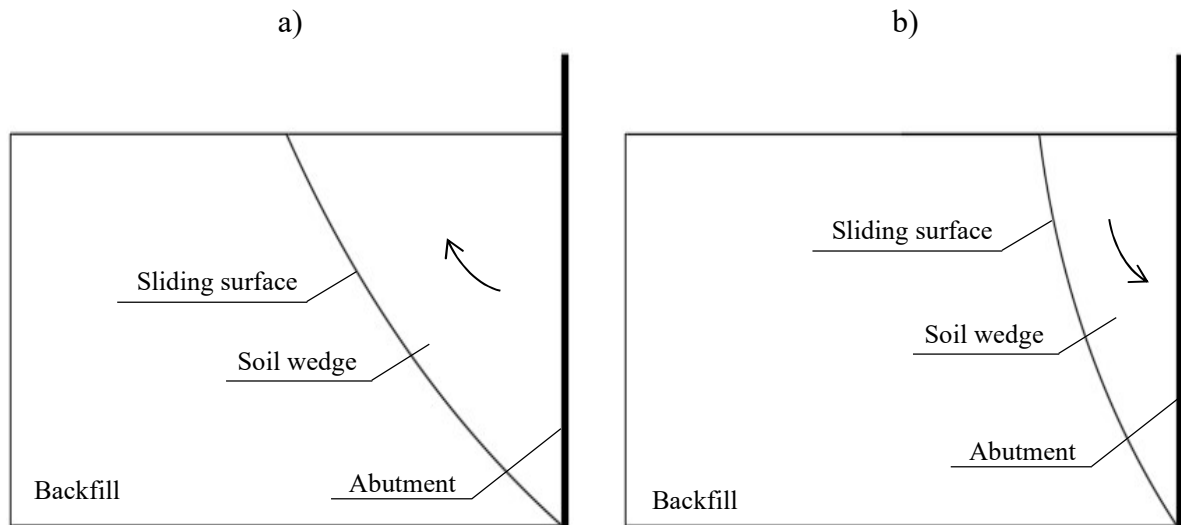
Figure 2.8 – Scheme of the stress-strain behavior of a material upon cyclic loading illustrating the phenomenon of ratcheting.



Source: Elaborated by the author (2020).

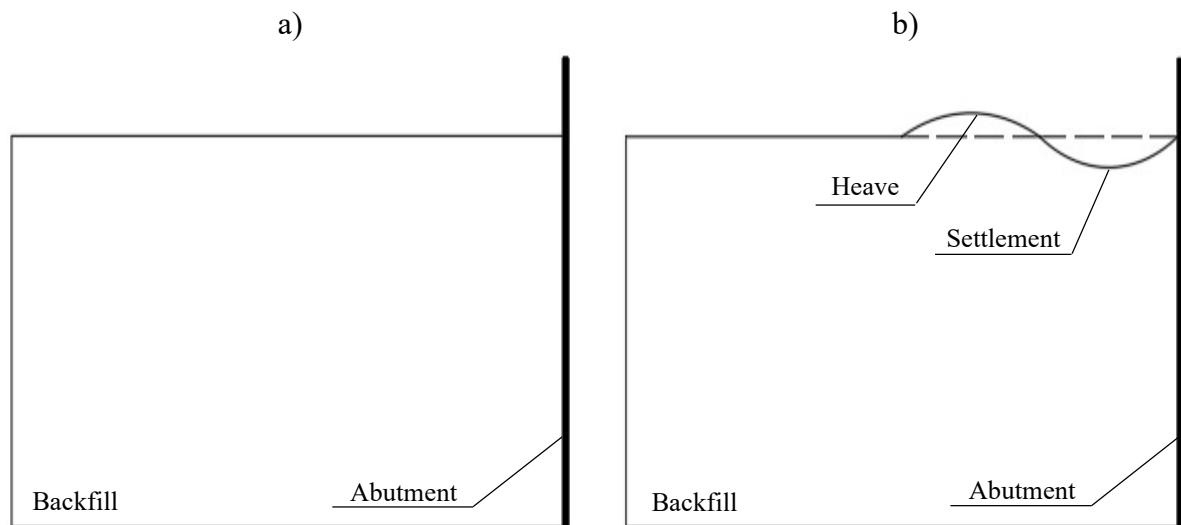
In a typical cycle of lateral displacement of the abutment, there are basically two movement directions: passive and active directions. In the passive direction, the abutment displaces against the backfill, and a large soil wedge slips upward toward the backfill surface (Figure 2.9a). On the other hand, in the active direction, the abutment displaces away from the backfill, and a small soil wedge slips downward toward the gap developed between the abutment and the backfill (Figure 2.9b). The initial position of the backfill surface in each cycle is not significantly recovered during cyclic lateral displacements of the abutment due to the plastic behavior of the soil (HOVARTH, 2004). Since there is no loss of soil mass in the backfill-abutment system, a portion of the backfill adjacent to the abutment is densified while another portion is displaced upwards. Hence, the backfill surface undergoes settlements adjacent to the abutment and heave away from the abutment (Figure 2.10), which increase with the cycles due to soil densification and granular flow (ENGLAND; TSANG; BUSH, 2000).

Figure 2.9 – Scheme of the backfill behavior in a typical cycle of lateral displacement of the abutment: a) passive direction; b) active direction.



Source: Elaborated by the author (2020).

Figure 2.10 – Scheme of backfill shape: a) before cyclic loading; b) after cyclic loading.

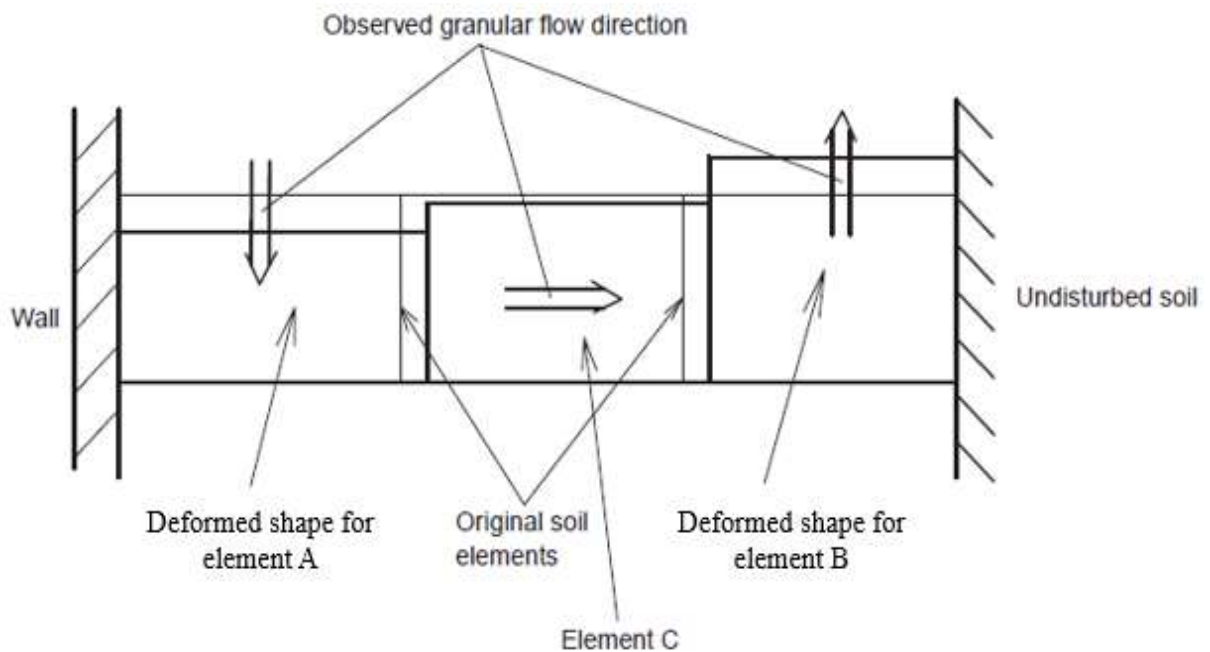


Source: Elaborated by the author (2020).

Numerical simulations using the discrete element method and laboratory experiments have revealed soil densification and granular flow behind the abutment upon cyclic lateral displacements (AL-QARAWI; LEO; LIYANAPATHIRANA, 2020; ENGLAND; TSANG; BUSH, 2000; GABRIELI; ZORZI; WAN, 2015; MUNOZ et al., 2012; RAVJEE et al., 2018; TATSUOKA et al., 2009; ZADEHMOHAMAD; BAZAZ, 2019; ZORZI; ARTONI; GABRIELI, 2017). England, Tsang and Bush (2000) proposed a model (the three-element model) to illustrate the concept of soil granular flow. In the proposed model, a soil element adjacent to the abutment (element A) accumulates compressive vertical strains and extensional

horizontal strains, while a soil element far from the abutment (element B) accumulates compressive horizontal strains and extensional vertical strains. An intermediary soil element (element C) connects elements A and B and permits the granular flow without presenting any strain. Despite the different behavior, the three elements undergo densification during cycling. Figure 2.11 shows a scheme of the three-element model illustrating the concept of soil granular flow.

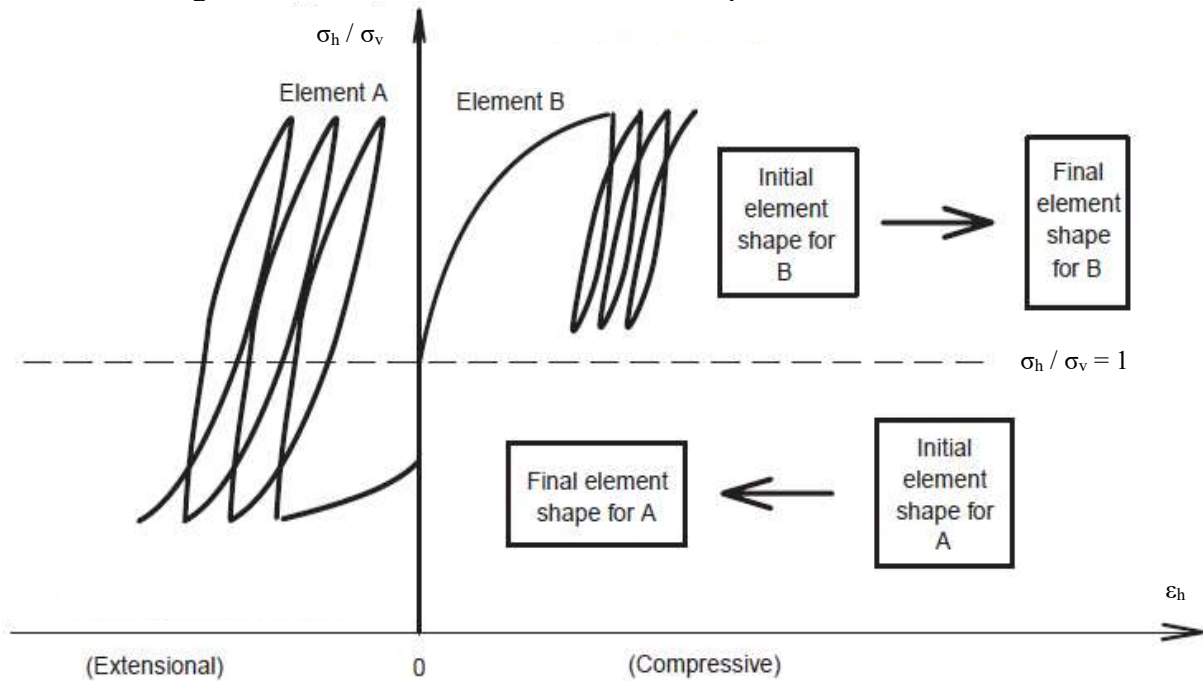
Figure 2.11 – Scheme of the three-element model illustrating the concept of soil granular flow.



Source: England, Tsang and Bush (2000).

According to England, Tsang and Bush (2000), the cyclic behavior of elements A and B is related to the stress state of these elements during cyclic loading. Element A is subjected to 90° jump changes in the principal stress directions while element B is subjected to stress increment reversals. In other words, during cyclic loading, the horizontal and vertical stresses of element A alternate between major and minor principal stresses while horizontal and vertical stresses of element B remain as major and minor principal stresses, respectively. Figure 2.12 shows the Mohr's circles of the cyclic stress variations in the soil elements.

Figure 2.13 – Stress-strain behavior and shapes of elements A and B.



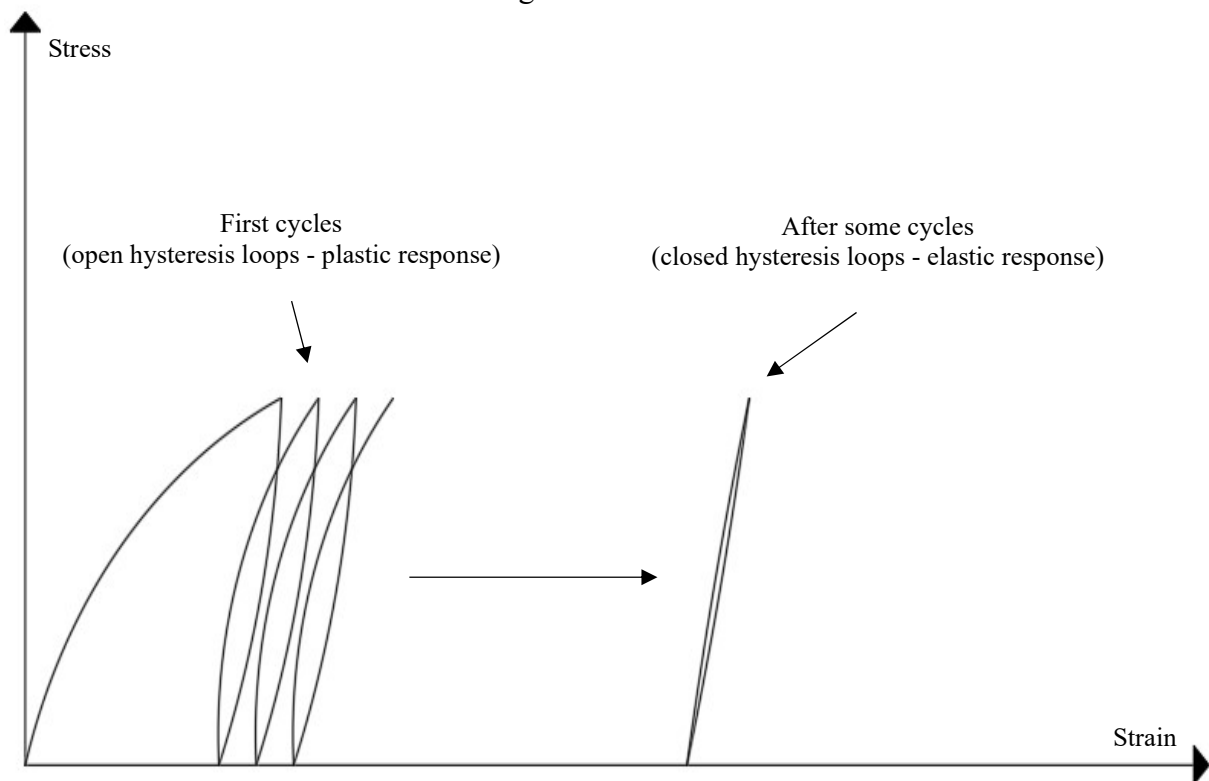
Source: Modified after England, Tsang and Bush (2000).

According to Al-Qarawi, Leo and Liyanapathirana (2020), England, Tsang and Bush (2000), and Tatsuoka et al. (2009), soil densification increases the stiffness of the backfill behind the abutment and, consequently, increases the lateral earth pressure on the abutment with the cycles. On the other hand, the soil granular flow reduces the soil mass adjacent to the abutment and, hence, tends to reduce the lateral earth pressure on the abutment with the cycles. England, Tsang and Bush (2000) state that a balance between the opposite effects of soil densification and granular flow can be reached when both effects are of comparable magnitude, which can lead the lateral earth pressures to a steady state. At this moment, residual volumetric strain changes become insignificant with increasing cycles (AL-QARAWI; LEO; LIYANAPATHIRANA, 2020), resulting in closed hysteresis loops, what means that the shakedown state has been reached (BOULBIBANE; WEICHERT, 1997; COLLINS; BOULBIBANE, 1998; GHADIMI; NIKRAZ; ROSANO, 2016; PANAGIOTOU; SPILIOPOULOS, 2015; ZHENG et al., 2017).

Shakedown is a state that solid and granular materials can reach when submitted to long-term cyclic loadings. In this state, the cyclic response of the material depends on the magnitude of the load applied during the cycles. If the material is subjected to cyclic loading with a load less than a critical load, so-called “shakedown load”, the long-term cyclic response of this material will be elastic, although the cyclic response can well be plastic for a finite number of initial load applications. In this case, the cyclic loading produces closed stress-strain

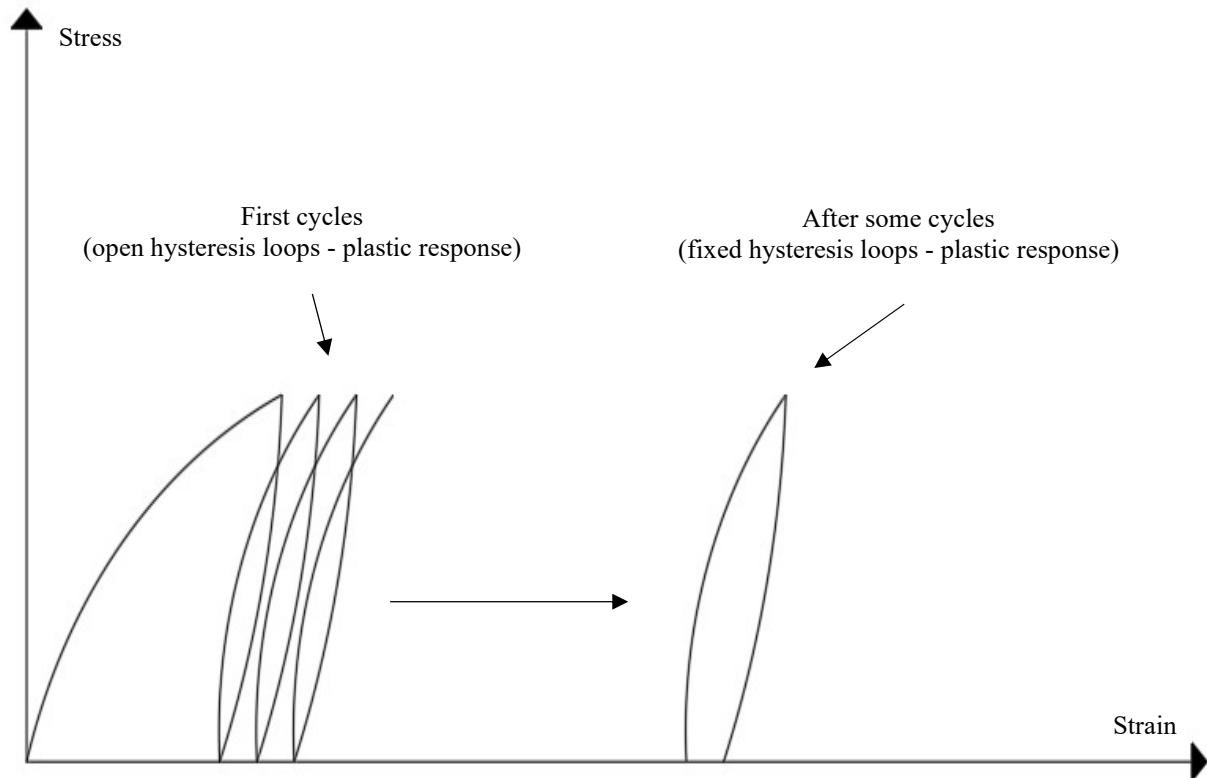
hysteresis loops when sufficient loading cycles are applied. This is referred to as elastic shakedown. On the other hand, if the load level exceeds the shakedown load, the long-term cyclic response of the material will be plastic for all load applications. In this case, the cyclic stress-strain behavior of the material becomes a fixed hysteresis loop when sufficient loading cycles are applied. This is referred to as plastic shakedown. In both elastic and plastic shakedown conditions, some residual plastic strain can be accumulated, but the total plastic strain will be bounded when sufficient loading cycles are applied (BOULBIBANE; WEICHERT, 1997; COLLINS; BOULBIBANE, 1998; GHADIMI; NIKRAZ; ROSANO, 2016; PANAGIOTOU; SPILIOPOULOS, 2015; ZHENG et al., 2017). Figure 2.14 and 2.15 illustrate the shakedown.

Figure 2.14 – Scheme of the stress-strain behavior of a material upon cyclic loading illustrating the elastic shakedown.



Source: Elaborated by the author (2020).

Figure 2.15 – Scheme of the stress-strain behavior of a material upon cyclic loading illustrating the plastic shakedown.



Source: Elaborated by the author (2020).

2.4 Previous studies on the response of backfill materials upon cyclic loadings

As previously mentioned, in view of the peculiar characteristic of IABs and SIABs, expansion and contraction cyclic longitudinal deformations of the superstructure due to temperature variations in the bridge induce cyclic lateral displacements at the abutment and the retained backfill. Such behavior favors the development of two important detrimental effects, which diminishes the benefits of the use of IABs and SIABs, as the result of a complex soil-structure interaction mechanism associated with the cyclic lateral displacements of the abutment: (1) the long-term build-up of lateral earth pressures on the abutment and (2) significant deformations in the backfill behind the abutment. Because of these effects, the abutment can undergo lateral earth pressures larger than those predicted by established theories, and the backfill surface can experience vertical displacements that can lead to safety and riding-quality issues for bridge users (AL-QARAWI; LEO; LIYANAPATHIRANA, 2020; BANKS; BLOODWORTH, 2018; PAK; BIGELOW; FELDMANN, 2017; RAVJEE et al., 2018; ZADEHMOHAMAD; BAZAZ, 2019).

For a better understanding of the previously mentioned detrimental effects, as well as the complex soil-structure interaction mechanism associated with the cyclic lateral displacements of the abutment, several studies involving physical measurements and numerical simulations have analyzed the response of the backfill-abutment system upon cyclic lateral displacements of the abutment (ABDEL-FATTAH; ABDEL-FATTAH, 2019; ABDEL-FATTAH; ABDEL-FATTAH; HEMADA, 2018; AL-QARAWI; LEO; LIYANAPATHIRANA, 2020; ARGYROUDIS et al., 2016; BANKS; BLOODWORTH, 2018; BLOODWORTH et al., 2012; BREÑA et al., 2007; CARISTO; BARNES; MITOULIS, 2018; CLAYTON; XU; BLOODWORTH, 2006; CIVJAN et al., 2013; DAVIDS et al., 2010; ENGLAND; TSANG; BUSH, 2000; FROSCH; LOVELL, 2011; GABRIELI; ZORZI; WAN, 2015; HUNTLEY; VALSANGKAR, 2013; KIM; LAMAN, 2012; KIM et al., 2014; KONG; CAI; KONG, 2015; LEHANE, 2011; MITOULIS et al., 2016; MUNOZ et al., 2012; RAVJEE, et al., 2018; TATSUOKA et al., 2009; ZADEHMOHAMAD; BAZAZ, 2019; ZORZI; ARTONI; GABRIELI, 2017). The results of these studies have shown the development of these detrimental effects, whose severity depends on many factors, such as displacement amplitude and backfill stiffness.

In general, from a physical point of view, it is exceedingly difficult to describe the behavior of soils upon cyclic loading, since the response depends strongly on several subtle properties of state (e.g. distribution, contacts, and arrangement of the grains) which cannot be expressed by the customary state variables (stress and strain ratios) only (DAFALIAS; HERRMANN, 1982). England, Tsang and Bush (2000) developed an instrumented physical model and a bi-dimensional finite element model to analyze the response of a granular material retained by a wall upon cyclic lateral displacements. The study evaluated the influences of the bridge completion date, the material stiffness, and the lateral displacement amplitude on the lateral earth pressures on the wall and the vertical displacements of the retained material surface. Three season starts (winter, spring, and summer) were chosen for the bridge completion date, two initial void ratio (e_0 equal to 0.56 and 0.64) were selected for the material stiffness and four amplitudes (0.17%, 0.25%, 0.45%, and 0.70% of the wall height) were adopted for the lateral displacement amplitude.

The results of the study of England, Tsang and Bush (2000) showed that the lateral earth pressures on the wall and the vertical displacements of the retained material surface increased with cycles. The lateral earth pressures presented a nonlinear distribution along the wall height with the largest values of pressure occurring within the middle third of the wall. The largest settlements occurred near the material-wall interface and decreased with the

distance from the wall, forming a heave at a distance from the wall. The lateral earth pressures showed a tendency of reaching a steady state after some cycles, while no tendency of steady state was reported for the vertical displacement of the retained material surface. The results also showed that the lateral earth pressures on the wall were not significantly affected by either the initial degree of compaction or the bridge completion date, especially in the long-term. However, the lateral displacement amplitude influenced the lateral earth pressures on the wall. On the other hand, the vertical displacements of the retained material surface were influenced by the initial degree of compaction, the bridge completion date, and the lateral displacement amplitude. The lateral earth pressures on the wall and the vertical displacements of the retained material surface increased with the lateral displacement amplitude, and no tendency of steady state was observed. In addition, settlements were generally smaller for denser materials than for looser materials. Finally, winter service-life starts led to slightly greater settlements than the other analyzed scenarios. The authors associated the obtained results with the mechanism of material densification and granular flow due to the phenomenon of ratcheting.

Clayton, Xu and Bloodworth (2006) conducted a series of cyclic triaxial tests with both granular and non-granular soils. Specimens were subjected to stress paths and strain levels that would be expected in soil elements behind an integral abutment undergoing cyclic lateral displacements due to temperature changes. This scenario was achieved by imposing radial strains on the specimens. Moreover, the study analyzed the impact of the initial density of the granular soil samples on deviator stresses with cycles. The results showed that the granular soil presented an increase of deviator stresses with cycles, in both loose and dense configuration, while the non-granular soil presented a decrease of deviator stresses with cycles. The authors attributed the increase in the deviator stresses to the rearrangement of irregularly shaped particles instead of soil densification.

Breña et al. (2007) instrumented and monitored an integral abutment bridge for a period of three years from 2002 to 2004. Several instruments were installed to capture selected parameters of bridge behavior during seasonal thermal fluctuations. Earth lateral pressures were measured by pressure cells placed behind the abutments at different heights. The monitoring showed that the maximum lateral earth pressures increased with cycles, while the minimum lateral earth pressures remained constant with cycles, in all depths. The authors stated that the increase in the maximum lateral earth pressures is indicative of an increase in the backfill density that contributes to a higher abutment restraint.

Tatsuoka et al. (2009) presented the results of a series of cyclic lateral loading tests under plane-strain conditions to evaluate the effects of cyclic lateral displacements of an

integral abutment on the performance of a compacted backfill. The tests were carried out with a lateral displacement amplitude of 0.6% of the abutment height. The backfill, which was produced by air pluviation, was composed of a poorly sub-angular sand with a relative density equal to 90%. The results showed that the lateral earth pressures on the abutment and the vertical displacement of the backfill surface increased with cycles. The largest settlements occurred near the backfill-abutment interface and decreased with distance from the wall, forming a heave at a certain distance from the abutment. The lateral earth pressures presented a tendency of reaching a steady state after some cycles, while no steady state tendency was reported for the vertical displacement of the backfill surface. The authors related the obtained results to the mechanism of soil densification and granular flow, which was named by the authors as dual ratcheting mechanism.

Frosch and Lovell (2011) reported the results of a 7-year field monitoring program to understand the in-service behavior of IABs. Three bridges were highly instrumented to analyze several parameters of interest, including the lateral earth pressures on the abutment. The monitoring showed an increase in the maximum lateral earth pressures within the first four years, followed by a tendency of steady state. On the other hand, the minimum lateral earth pressures remained virtually constant since the beginning of the monitoring. The authors associated the obtained results with ratcheting and concluded that increases in lateral earth pressures upon integral abutments may exist, but for limited periods of time.

Huntley and Valsangkar (2013) presented and discussed data of field monitoring of an instrumented IAB with abutments retaining a backfill composed of a free-draining material. Instruments were installed to monitor the lateral earth pressures on the abutment, the vertical displacements of the backfill surface, and the ambient temperature. The study analyzed the data of seasonal lateral earth pressure variation throughout a period of three years. It was observed a slight tendency of lateral earth pressure increase with seasonal temperature cycles during the monitored period. Furthermore, the pressures presented a nonlinear distribution along the abutment height, with the largest values within the upper third of the abutment. The authors concluded that a greater monitoring period is necessary to better understand the actual behavior of seasonal lateral earth pressure variations behind the abutment.

Gabrieli, Zorzi and Wan (2015) performed experimental and numerical analyses to investigate the phenomenon of ratcheting in different granular materials after 50 cycles of lateral displacements. Different amplitudes were used in the investigation: 0.75 mm, 1.5 mm, 3 mm, and 6 mm. An instrumented physical model monitored by a digital camera and a tri-dimensional 1:1 scale discrete element model of a glass box with a movable vertical retaining

wall were used to analyze the lateral thrusts on the wall and the displacements of the grains of the tested materials. Results showed the occurrence of ratcheting in both physical and numerical models. The largest deformations of the retained materials took place near the material-wall interface and decreased with distance from the wall. Three different zones with three different behaviors were identified: (1) a static zone (far from the wall), (2) an alternating active-passive wedge (next to the wall), and (3) a passive wedge (in the middle between zones (1) and (2)). Moreover, the values of volumetric strains increased with the displacement amplitude.

The results of the study by Gabrieli, Zorzi and Wan (2015) also showed that the lateral thrusts increased with the cycles and reached the steady state after some cyclic lateral displacements of the wall, in both physical and numerical models. The lateral thrust increased with displacement amplitude. The authors concluded that simulations with the discrete element method proved to be a good tool to provide insight into the micromechanical variables that are linked to the macroscopic phenomena. Furthermore, the authors associated the obtained results with the material densification, due to ratcheting, and the self-organization of the particle contacts.

Zorzi, Artomi and Gabrieli (2017) studied the effects of cyclic loadings on a granular material retained by a wall using a physical model and a bi-dimensional discrete element model. Experimental tests were carried out by applying 50 cycles of lateral displacements of the wall with amplitudes of ± 0.75 mm and ± 1.5 mm. Numerical simulations were performed by applying 100 cycles of lateral displacement of the wall with amplitudes of ± 0.75 mm and ± 1.5 mm. The authors analyzed the horizontal force on the wall and the vertical displacements on the surface of the retained material. The results showed an increase of the horizontal force on the wall and an increase of the vertical displacements of the soil with cycles, in both physical and numerical models. Forces and displacements were higher for the ± 1.5 mm amplitude than for the ± 0.75 mm amplitude. Moreover, it was possible to observe that the largest settlements occurred near the material-wall interface and decreased with distance from the wall. A heave was noticed at a distance from the wall, in both physical and numerical models. The authors associated the obtained results with the mechanism of material densification and microstructural changes.

Banks and Bloodworth (2018) carried out numerical simulations to examine the lateral earth pressures on an integral bridge abutment. A bi-dimensional finite-difference model was developed based on the laboratory test results of Xu, Clayton and Bloodworth (2007) to predict the lateral earth pressures acting on an integral abutment with granular backfill. One hundred and twenty cycles of prescribed horizontal displacements were applied to simulate four different bridge overall lengths ranging from 15 m to 100 m. The prescribed displacements corresponded

to 0.1%, 0.25%, 0.37% and 0.62% of the abutment height. The results showed that the lateral earth pressures presented a nonlinear distribution along the abutment height, with the largest values occurring within the middle third of the abutment for all analyzed bridge lengths. In addition, the study analyzed the effect of daily cycles on the annual response of the backfill-abutment system and observed that daily plus annual cycles produced lateral earth pressures higher than annual cycles only. In all numerical simulations, the lateral earth pressures increased with cycles. The authors associated the obtained results with small rotations of non-spherical particles that take place in the active state during bridge contraction.

Caristo, Barnes and Mitoulis (2018) performed numerical simulations using finite elements to analyze the complex soil-structure interaction between an integral bridge abutment and a compacted sand backfill. The study analyzed the lateral earth pressures on the abutment and the vertical displacements of the backfill surface by applying 120 cycles of prescribed horizontal displacements ranging from -27 mm to +27 mm to simulate the seasonal effects to which the bridge would be exposed during its lifespan. The displacements were applied in two different loading sequences to assess the influence of the initial movement of the abutment on the backfill behavior. In one loading sequence, the abutment first moved away from the backfill and subsequently pushed back against the backfill (case 1), while the opposite occurred in the other loading sequence (case 2). The results of the study showed an increase of lateral earth pressures on the abutment and an increase of vertical displacements of the backfill surface with the number of cycles. Soil pressures presented a nonlinear distribution along the abutment height, with the largest values occurring within the middle third of the abutment. Pressures built up quickly during the first 15 cycles, and higher values were recorded for case 1, as compared to case 2. However, no difference between both loading sequences could be observed from the 30th cycle when a tendency of steady state was reached in both cases. The displacements were practically unaffected by the initial direction of the abutment movement. Moreover, it was possible to observe that the largest settlements occurred near the backfill-abutment interface and decreased with the distance from the abutment, forming a heave at a certain distance from the abutment. The authors associated the obtained results with the ratcheting phenomenon and the nonlinear behavior of the soil.

Ravjee et al. (2018) studied the effects of six different particle shapes (tetrahedrons, triangular prisms, truncated tetrahedrons, cubes, dodecahedrons, and spheres) on the backfill response upon cyclic loading behind an integral abutment using a discrete element model. Twenty-five cycles of 0.154° -angular rotation were applied to simulate the angular rotation of an integral abutment due to temperature variations. The results of all analyzed particle shapes

showed considerable densification near the material-abutment interface, which decreased with increasing distance from the abutment. The material densification of all analyzed particle shapes presented a nonlinear increase with a decreasing rate within the first cycles and then reached the steady state after a few more cycles. Moreover, the differences in density between the zones near the material-abutment interface and far from the abutment reduced linearly with increasing sphericity of the particles. The study also showed that the lateral earth pressures on the abutment, with all analyzed particle shapes, presented a nonlinear increase with a decreasing rate within the first cycles and then reached the steady state after a few more cycles. In addition, the increase in the lateral earth pressures reduced linearly with increasing sphericity of the particles. The authors concluded that the increase in the lateral earth pressures on the abutment is related to material densification and particle interlocking and reorientation, and that prevalence of effects depends on particle sphericity. Densification with highly spherical particles extended over the entire backfill domain, while densification with highly angular particles became more localized near the material-abutment interface. In this case, accumulation of lateral earth pressures with shapes of higher angularity is suggested to be a result of not only localized densification but also the evolution of the structure within the particulate mass due to particle interlocking and reorientation.

Abdel-Fattah and Abdel-Fattah (2019) presented a finite-element study on the behavior of IABs under alternate cycles of expansion and contraction of the bridge due to seasonal temperature variation. The study assessed the lateral earth pressures on the abutment for different amplitudes of lateral displacements. The results showed lateral earth pressures with a nonlinear distribution along the abutment height. The maximum pressures occurred within the bottom third of the abutment, with the lowest displacement amplitude. However, the locus of the maximum pressures moved toward the middle third of the abutment with increasing displacements. Furthermore, the increase of the lateral pressure was directly proportional to the increase of the displacement amplitude.

Al-Qarawi, Leo and Liyanapathirana (2020) analyzed the response of a backfill-abutment system upon cyclic lateral displacements of the abutment with both laboratory tests and numerical simulations. An instrumented physical model and a bi-dimensional finite element model of a small wall retaining loose sand were used to assess the effects of cyclic lateral displacements on lateral earth pressures on the abutment and vertical displacements of the backfill surface. Thirty cycles of lateral displacements equal to $\pm 0.67\%$ of the wall height were applied to simulate the expansion/contraction of the bridge superstructure due to temperature changes. Results of both physical and numerical models showed that the lateral

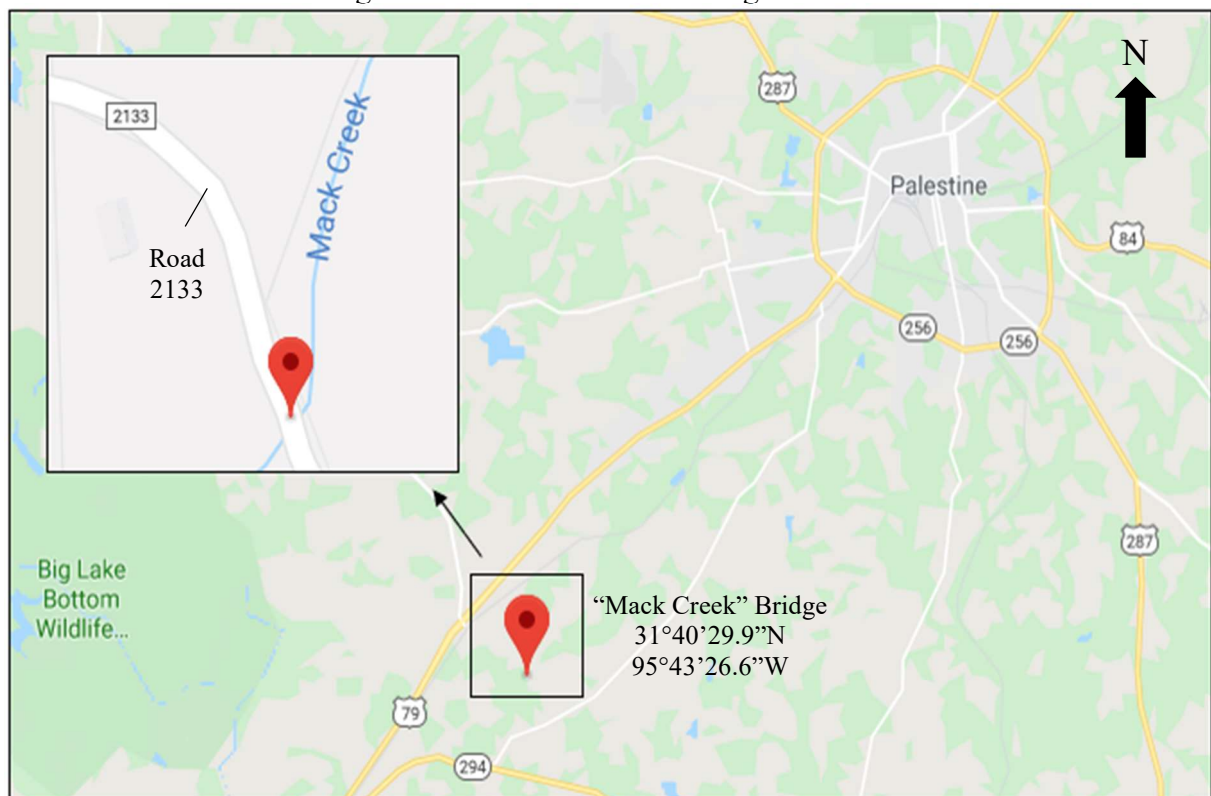
earth pressures on the abutment and the vertical displacements of the backfill surface increased with the cycles. The largest settlements occurred near the backfill-abutment interface and decreased with increasing distance from the abutment. A heave was detected at a certain distance from the abutment, in both physical and numerical models. The authors associated the obtained results with the mechanism of soil densification and granular flow, named as dual ratcheting mechanism after Tatsuoka et al. (2009).

3 THE “MACK CREEK” BRIDGE PROJECT

3.1 Bridge location and description

The bridge evaluated in this research, commonly referred to as “Mack Creek” Bridge, was completed in July 2017 and is located at the intersection between Road 2133 and the Mack creek, near the city of Palestine, Texas, United States of American. Figure 3.1 shows the location of the “Mack Creek” Bridge.

Figure 3.1 – “Mack Creek” Bridge location.



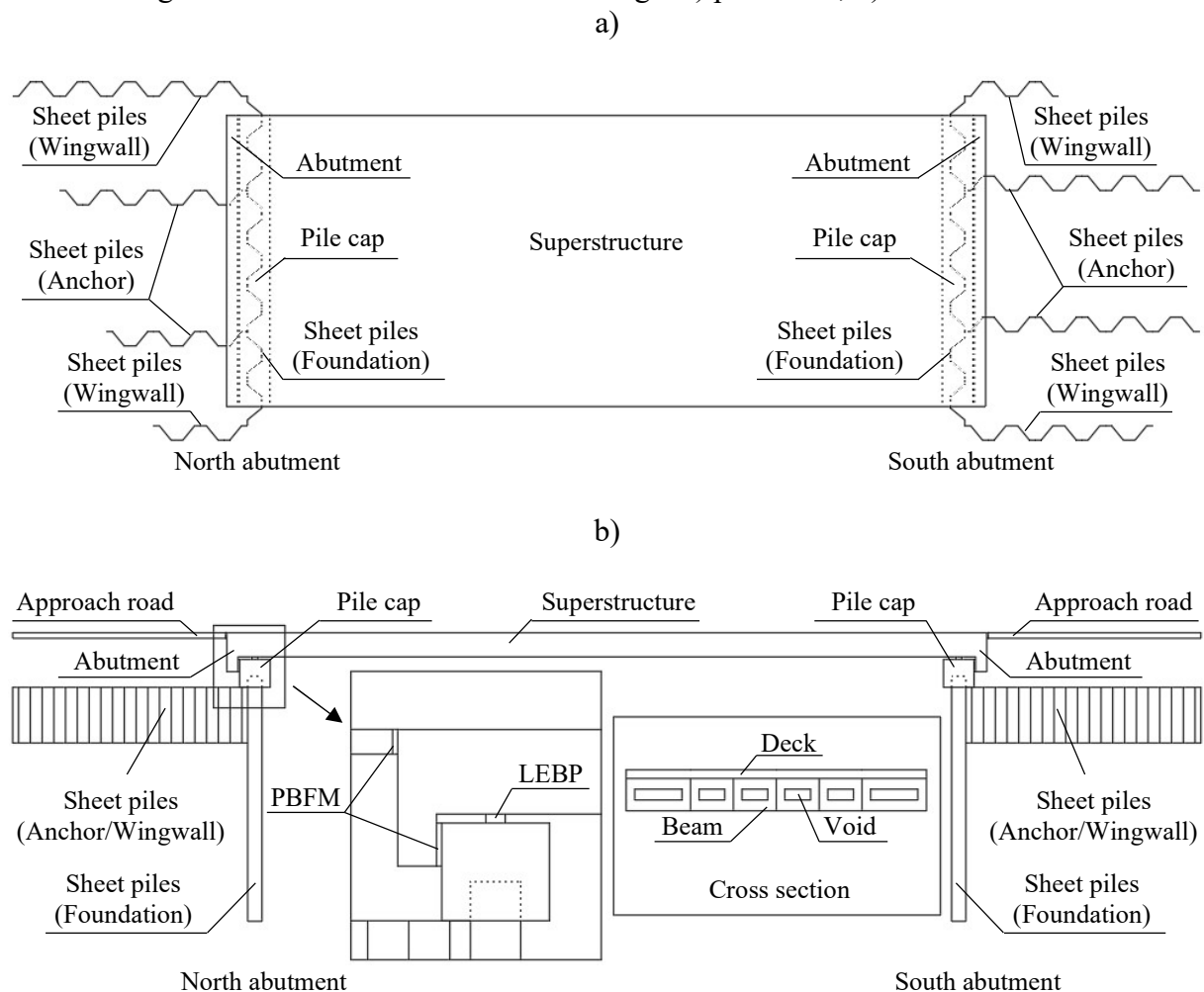
Source: Modified after Google Maps (2019).

The “Mack Creek” Bridge is a semi-integral abutment bridge (SIAB) with a total length of 20.53 m and a total width of 7.85 m. The superstructure is a 19.93-m long by 0.65 m wide single-span, composed of a 0.15-m thick reinforced concrete deck and 0.5-m high prestressed concrete box beams. The superstructure is integrally connected to 1.05-m high and 0.3-m thick reinforced concrete abutments. The superstructure-abutment system is supported by 6.6-m long driven steel sheet piles. The sheet piles are connected to 0.83-m wide and 0.75-m high reinforced concrete pile caps. The pile caps are separated from the abutments by a sheet

of preformed bituminous fiber material (PBFM) with a thickness of 40 mm and a width of 0.33 m. Laminated elastomeric bearing pads (LEBP) with a thickness of 70 mm separate the pile caps and the abutment.

The foundation sheet piles are connected to 1.5-m long driven steel sheet piles, which serve as anchor walls inside the soil, and 2.1-m long driven steel sheet piles, which serve as wingwalls embracing the backfill. The anchor walls and the wingwalls have variable lengths in the longitudinal direction of the bridge. All sheet piles are made of PZC-18 profiles manufactured by Gerdau (GERDAU, 2019). The approach roads are composed of a 0.15-m thick asphalt concrete pavement and are separated from the abutments by a sheet of PBFM with a thickness of 40 mm and a width of 0.15 m. Further details about the “Mack Creek” Bridge Project can be found in TxDOT (2016). Figure 3.2 shows a schematic view of the bridge, and Figure 3.3 shows photographs of the bridge after construction.

Figure 3.2 – Schematic view of the bridge: a) plan view; b) elevation view.



Source: Elaborated by the author (2020).

Figure 3.3 – Photographs of the bridge after construction: a) top view; b) bottom view.



Source: Walter (2018).

3.2 Subsoil characteristics

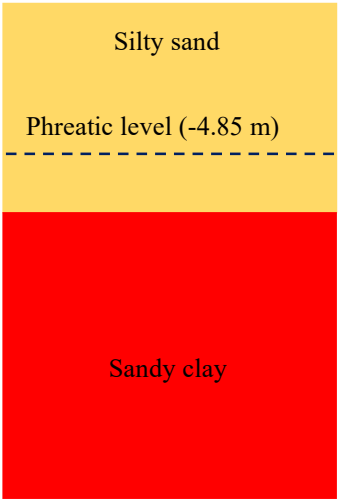
Subsoil investigation included Texas Cone Penetrometer (TCP) tests carried out nearby each abutment (TxDOT, 2016). The TCP test is a prospection method used by the Texas Department of Transportation (TxDOT) and was developed in cooperation with Materials & Tests and Equipment & Procurement Divisions (PALLA et al., 2008). This prospection method is a dynamic field penetration test that can be used to evaluate geomaterials encountered during geotechnical investigations through the penetration resistance of a cone (MOGHADDAM, 2016).

The TCP test procedure is described in TxDOT Designation: Tex-132-E – Test Procedure for Texas Cone Penetration (TxDOT, 1999). The procedure consists of dropping, with a 0.6-m drop height, a 77-kg hammer to drive a 76-mm diameter penetrometer cone attached to a 60-mm drill stem in soil or rock. The penetration is performed in three separate increments, and the first increment is completed after 12 blows or 0.15 m, whichever happens first. The result consists of the sum of the number of blows needed to achieve the second and the third 0.15-m increments of cone penetration. In hard materials, including rocks, after the first increment is completed, the cone is driven 100 blows, and the penetration value for the first and second 50 blows is recorded. Further details about the TCP test can be found in TxDOT (1999).

According to the TCP test results, the subsoil in the north abutment region is composed of a 6.5-m thick silty sand layer over a sandy clay layer. A 2.5-m thick clayey sand layer,

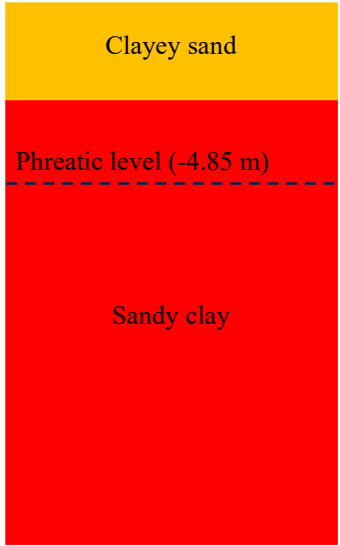
followed by a sandy clay layer, was found in the south abutment region. The phreatic level was located at a depth of 4.85 m at the time of ground prospection. Tables 3.1 and 3.2 show the TCP test results (TxDOT, 2016).

Table 3.1 – TCP test results near the north abutment.

Number of blows (Penetration in cm)		Depth	Profile
2nd increment	3rd increment		
-	-	0 m (Approach road surface)	
-	-	-2 m (Beginning of TCP test)	
10 (15)	12 (15)	-3.5 m	
8 (15)	7 (15)	-5 m	
8 (15)	9 (15)	-6.5 m	
34 (15)	50 (15)	-8 m	
50 (7.5)	50 (11.25)	-9.5 m	
50 (7.5)	50 (11.25)	-11 m	
50 (3.75)	50 (2.5)	-12.5 m	
50 (2.5)	50 (2.5)	-14 m	
50 (3.75)	50 (2.5)	-15.5 m (End of TCP test)	

Source: Modified after TxDOT (2016).

Table 3.2 – TCP test results near the south abutment.

Number of blows (Penetration in cm)		Depth	Profile
2nd increment	3rd increment		
-	-	0 m (Approach road surface)	
-	-	-1 m (Beginning of TCP test)	
7 (15)	7 (15)	-2.5 m	
4 (15)	2 (15)	-4 m	
10 (15)	8 (15)	-5.5 m	
42 (15)	50 (13.75)	-7 m	
50 (12.5)	50 (12.5)	-8.5 m	
50 (12.5)	45 (15)	-10 m	
44 (15)	50 (3.75)	-11.5 m	
50 (1.25)	50 (0)	-13 m	
50 (2.5)	50 (1.25)	-14.5 m	
50 (2.5)	50 (1.25)	-16 m (End of TCP test)	

Source: Modified after TxDOT (2016).

3.3 Backfill characteristics

The bridge backfill is composed of a crushed-rock identified as D-Rock by the contractors of the project (TxDOT, 2016). The gravel particles were industrially produced by crushing larger pieces of rock and are not a naturally occurring aggregate. Poor compaction techniques for the selected backfill material were implemented during bridge construction (ZORNBERG et al., 2019). Figure 3.4 shows the backfill material being placed in the field.

Figure 3.4 – Backfill material as used in the field.

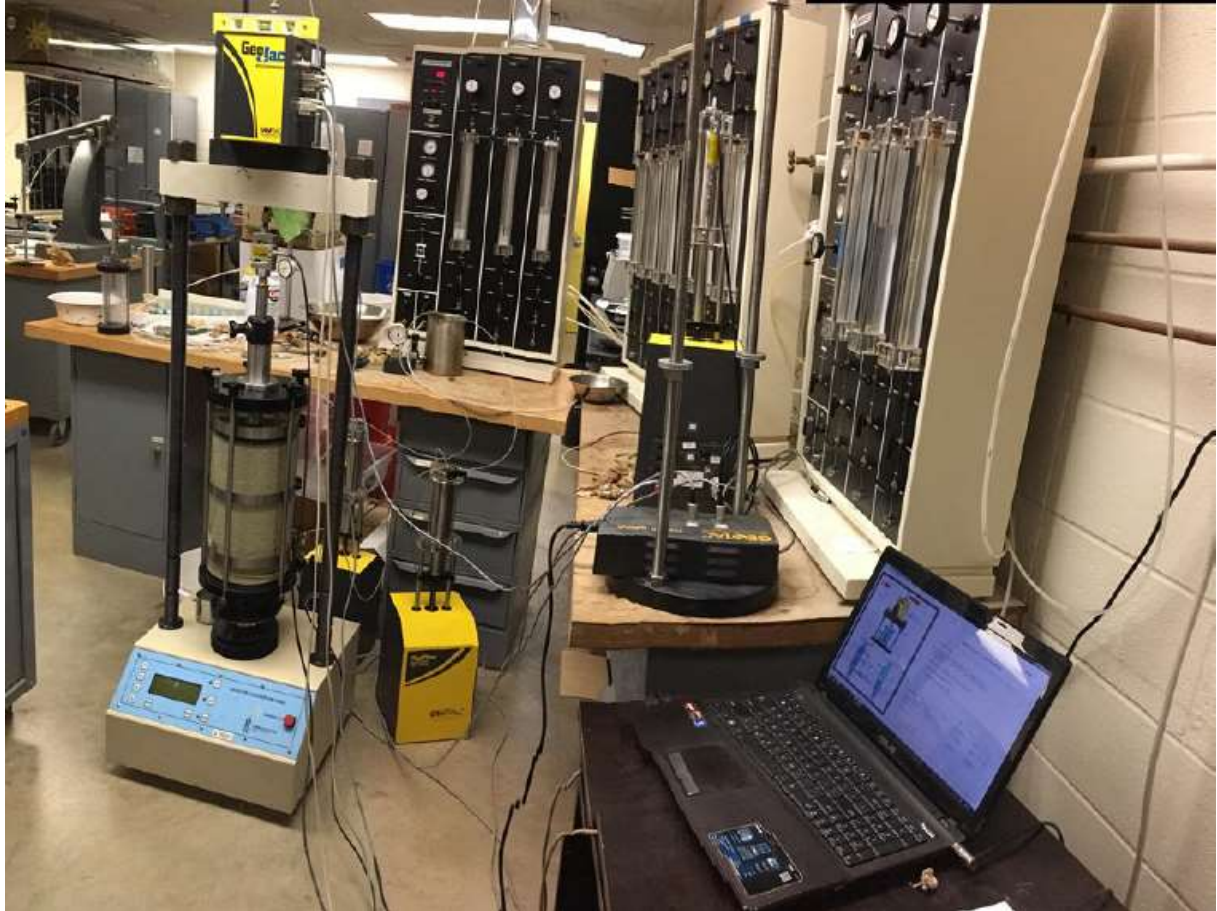


Source: Walter (2018).

A large quantity of backfill material was collected and taken to the Geotechnical Laboratory of The University of Texas at Austin for subsequent testing. A series of consolidated drained triaxial tests were performed to estimate the parameters of the backfill material. Among the different modes of triaxial testing, consolidated drained testing was chosen as the most appropriate mode to represent the field conditions since the tested material is made of large and relatively clean aggregates (high hydraulic conductivity), and the loading rate is very small (small level of displacement over the course of a day). Since the grains of the backfill material can be as big as 13 mm, a triaxial cell larger than 76 mm in diameter was needed (ASTM, 2011).

For this purpose, a 152-mm diameter triaxial cell was assembled to accommodate the testing program. This triaxial setup provided 10% axial strain and 500-kPa load capacity (ZORNBERG et al., 2019). Figure 3.5 shows the triaxial setup used in the testing program.

Figure 3.5 – Triaxial setup used in the testing program.

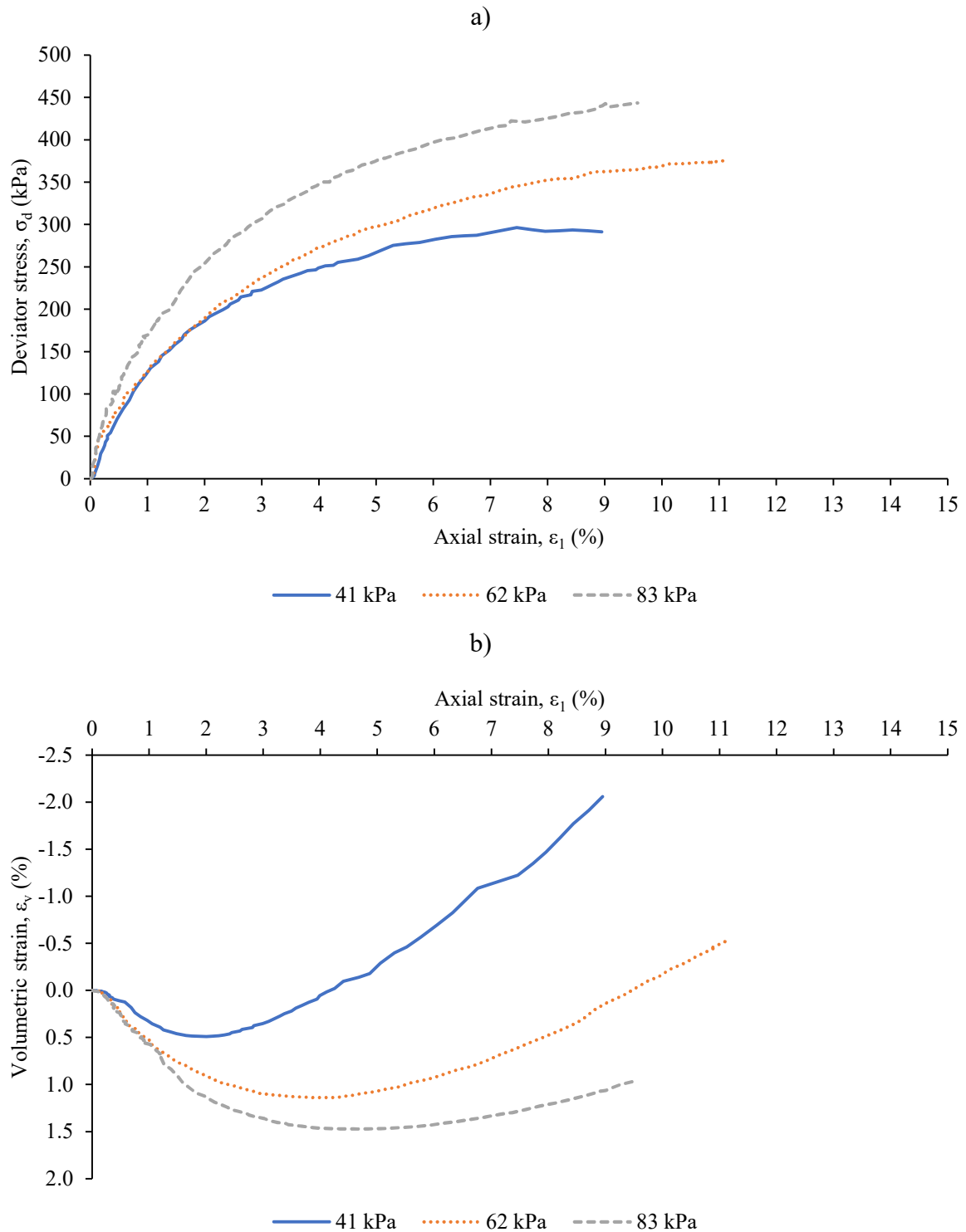


Source: Zornberg et al. (2019).

Compaction efforts were minimized to prevent membrane puncture (the membrane was punctured twice during the tests) since the material had grains with high angularity, and therefore the presented results are for lightly compacted material. The specimens were fully saturated so that the volume of outflow/inflow was equal to changes in pore volume and also in order to be able to sustain a constant pore and cell pressure during shearing as the specimens undergo volume change. To this end, the specimens in each test were backpressure saturated to 414-483 kPa, followed by a final B-value check. The calculated B-value for each specimen was 94%, and it was found that a higher B-value was not obtainable due to the stiffness of the crushed rock aggregates. After backpressure saturation was completed, the shearing phase was started. Overall, three tests at effective confining pressures of 41 kPa, 62 kPa, and 83 kPa were

carried out to estimate the Mohr-Coulomb's failure envelope. Figure 3.6 shows the results of the triaxial tests.

Figure 3.6 – Results of the triaxial tests: a) stress x strain curves; b) volumetric strain x axial strain curves.



Source: Modified after Zornberg et al. (2019).

The tested material presented a typical stress-strain behavior of a loose granular material (Figure 3.6a). However, it showed a typical dilative behavior of a dense granular material (Figure 3.6b) despite having been lightly compacted, and this was most likely due to the high degree of angularity of the grains. The inspection of a specimen after the cell was drained showed no clear shear failure plane observable with the naked eye, and the samples appeared to have experienced a bulging failure, as is typical in granular materials. Figure 3.7 shows a post-shearing specimen.

Figure 3.7 – Triaxial specimen at failure.



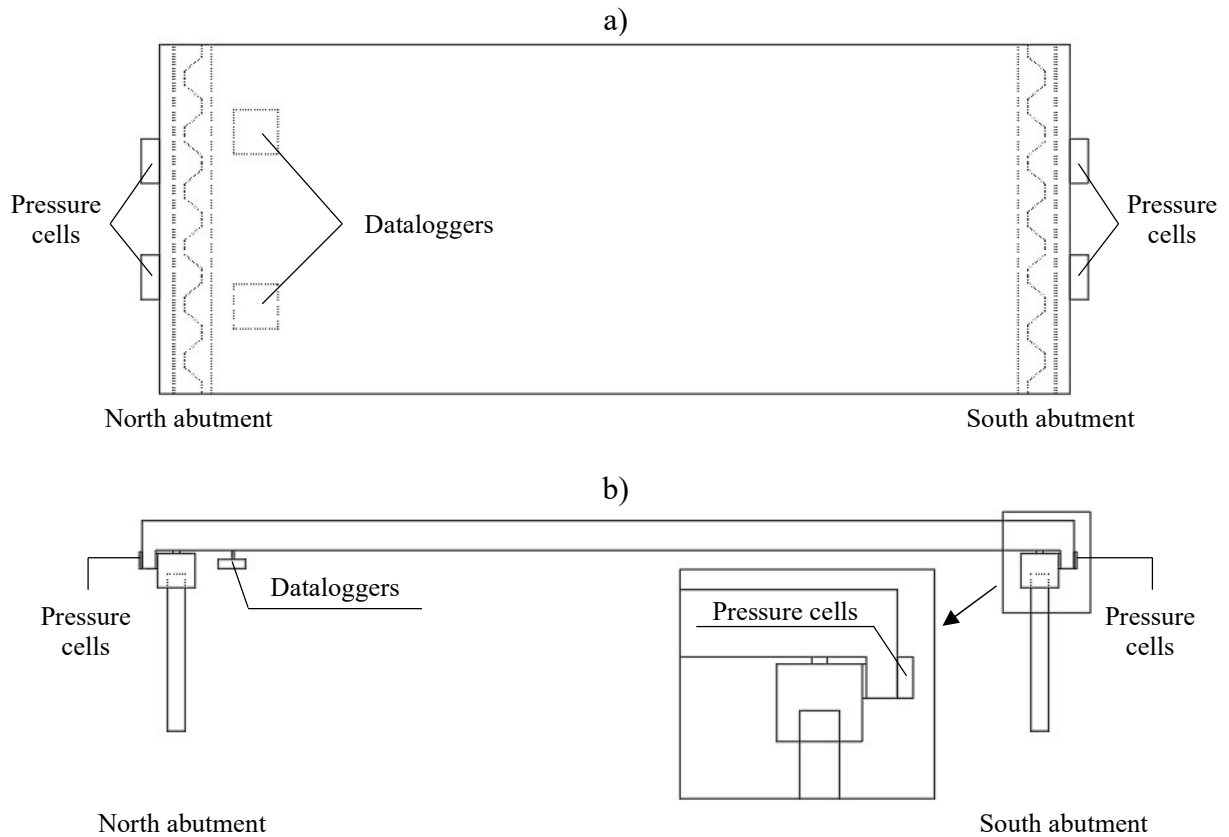
Source: Zornberg et al. (2019).

Values of effective friction angles (ϕ') were calculated by $\phi' = 2 \left(\tan^{-1} \sqrt{\frac{\sigma'_1}{\sigma'_3}} - 45^\circ \right)$, where σ'_1 and σ'_3 are the maximum values in the curves shown in Figure 3.6a. The estimated values of ϕ' were equal to 48° , 45° , and 42° for effective confining pressures equal to 41 kPa, 62 kPa, and 83 kPa, respectively.

3.4 Field instrumentation and monitoring

Lateral earth pressures on the abutments and ambient air temperature have been monitored in the field by pressure cells and temperature sensors, respectively. Four Geokon model 4810 vibrating wire (VW) contact pressure cells with 230 mm in diameter and 12 mm in thickness (GEOKON, 2019a) were installed vertically against the abutment-backfill interface (two pressure cells were used in each abutment) prior to backfilling. Two Geokon model 8002 LC-2x4 VW dataloggers with temperature sensors (GEOKON, 2019b) were used to record the readings from the pressure cells and temperature sensors. All pressure cells were buried at the same depth in the abutment, and the dataloggers were positioned under the superstructure near the north abutment. Further details about the instrumentation of the bridge in the field can be found in Walter (2018). Figure 3.8 shows a schematic view of the position of the devices in the bridge, Figure 3.9 shows the devices used in the field monitoring, and Figure 3.10 shows the devices installed in field.

Figure 3.8 – Schematic view of the position of the devices in the bridge: a) plan view; b) elevation view.



Source: Elaborated by the author (2020).

Figure 3.9 – Devices used in the field monitoring: a) pressure cell; b) datalogger.



Source: Walter (2018).

Figure 3.10 – Devices installed in the field: a) pressure cells; b) dataloggers.

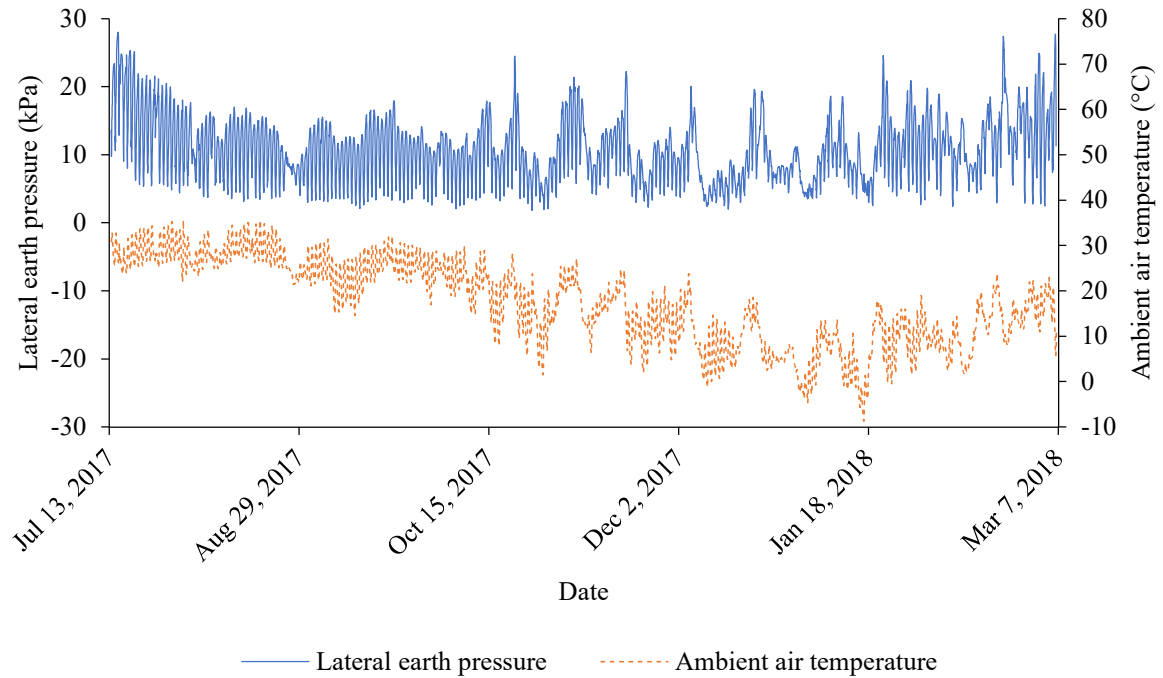


Source: Walter (2018).

Pressure and temperature data were recorded by the dataloggers on an hourly basis during the field survey. The temperature values provided by the temperature sensors were compared to the data of ambient air temperature collected by a weather station at the city of Palestine, Texas, United States of American. A good match between the temperature values collected by both the weather station and the temperature sensors was obtained, which indicates that the temperatures recorded by the dataloggers were representative of the site ambient air temperatures. Since significant differences between readings from the temperature sensors were not observed, the ambient air temperature was assumed as the average between the readings from both temperature sensors. Similarly, the lateral earth pressure was assumed as the average between readings from both pressure cells at each abutment. Further details about the field

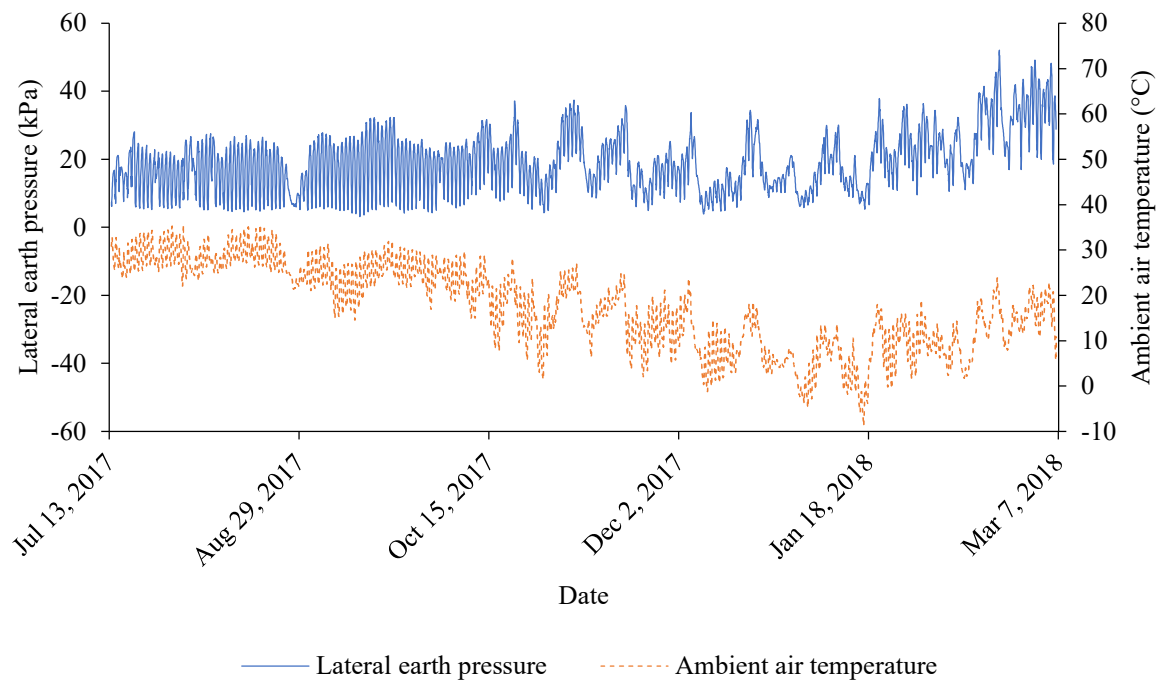
monitoring can be found in Walter (2018). Figures 3.11 and 3.12 show the lateral earth pressures on the abutments and the ambient air temperature.

Figure 3.11 – Lateral earth pressures on the north abutment and ambient air temperatures.



Source: Modified after Walter (2018).

Figure 3.12 – Lateral earth pressures on the south abutment and ambient air temperatures.

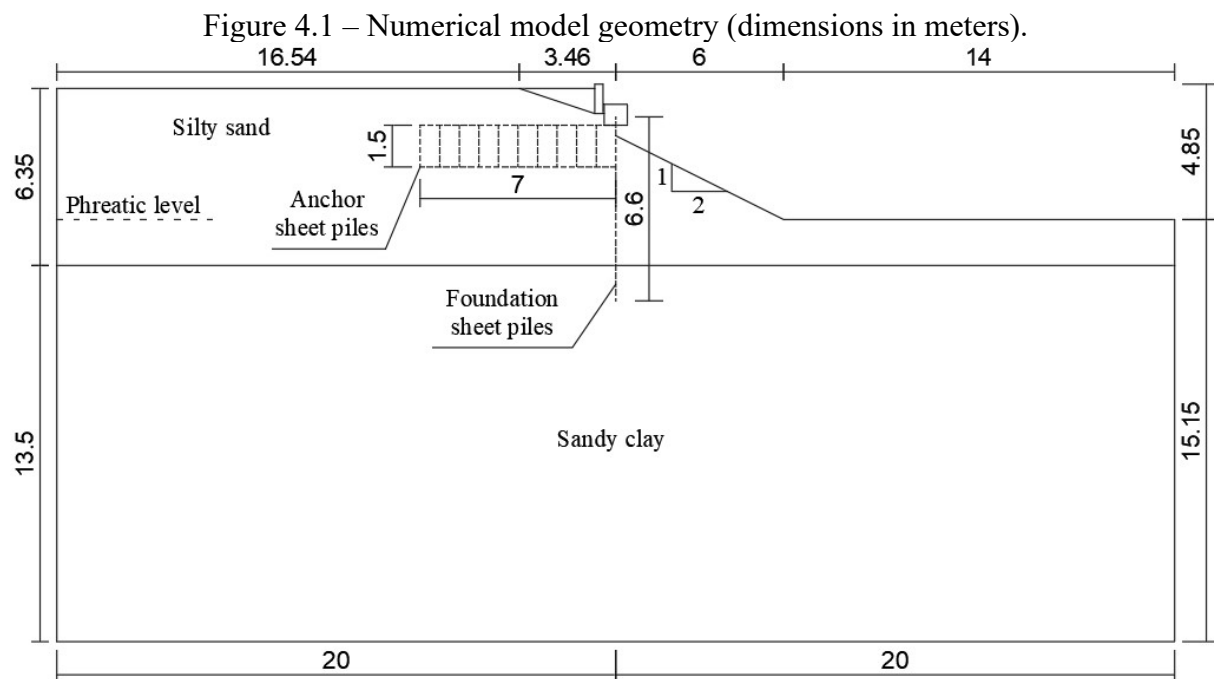


Source: Modified after Walter (2018).

4 NUMERICAL MODELING CHARACTERISTICS

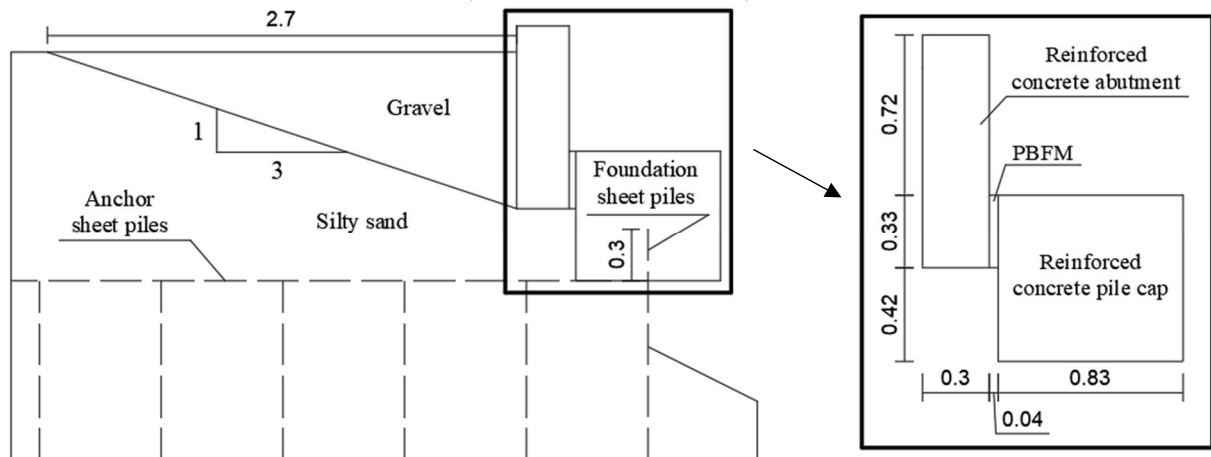
4.1 Numerical model description

A finite element numerical model was developed for the north abutment by using the software Plaxis 2D version 2016 (PLAXIS BV, 2016). Plane strain conditions were used in a two-dimensional finite element analysis since the measured lateral earth pressures were virtually constant in the direction of the bridge width. The geometry of the numerical model was defined based on the information provided by TxDOT (2016). The model boundaries extended to a length of 40 m in the horizontal direction and 20 m in the vertical direction. These dimensions were assumed to be enough to exclude boundary effects (KNAPPETT et al., 2016; RAWAT; GUPTA, 2017). Figure 4.1 shows the geometry of the numerical model, and Figure 4.2 shows a zoom of the model in the region of the abutment.



Source: Elaborated by the author (2020).

Figure 4.2 – Zoom of the numerical model geometry in the region of the abutment (dimensions in meters).



Source: Elaborated by the author (2020).

The soil materials (sandy clay, silty sand, and gravel), the reinforced concrete, and the preformed bituminous fiber material (PBFM) were represented by soil clusters, which can be used in the software to model volumes of materials. The foundation sheet piles were represented by plate elements while the anchor sheet piles were represented by fixed-end anchor elements with a vertical spacing of 150 mm and a horizontal length of 7 m. Plate elements are structural objects, with flexural and normal stiffness, which can be used to simulate the influence of slender structures (walls, plates, shells, or linings) in the ground extending in the out-of-plane direction. Fixed-end anchor elements are point elements, attached to a structure at one side and fixed at the other side, which can be used to model anchor or props, with spacing in the out-of-plane direction, to support retaining walls (BRINKGREVE; KUMARSWAMY; SWOLFS, 2016b). The vertical spacing of the anchor elements was defined by discretizing the height of the anchor walls in ten equal parts, and the horizontal length of the anchor elements was assumed to be the average length of the anchor walls.

The soil-structure interaction was modeled by interface elements with strength reduction factors (R_{inter}) equal to 0.5 for soil-steel interface and 0.7 for soil-concrete interface. Interface elements are joint elements, created next to structural elements or between soil clusters, which can be used to simulate a thin zone of intensely shearing material at the contact between a structure and the surrounding soil (BRINKGREVE; KUMARSWAMY; SWOLFS, 2016b). The R_{inter} values were chosen based on the suggestions made by Brinkgreve, Engin and Swolfs¹ (2012 apud MUSZYNSKI; WYJADLOWSKI, 2019) and Naval Facilities Engineering

¹ BRINKGREVE, R. B. J.; ENGIN, E.; SWOLFS, W. M. **Plaxis 2D version 2012 manual**. Rotterdam: Balkema, 2012.

Command (1986). A virtual thickness factor of 0.1, which is the default value of the software, was applied to the interface boundaries. An interface with R_{inter} equal to 1 was applied to the steel-concrete interaction to avoid punching problems detected in preliminary simulations.

The effects of the superstructure on the abutment-pile cap system were represented by static equivalent loads calculated with the software Ftool (Martha, 2018). This approach was adopted for simplicity, to avoid excessive calculation periods. A simplified structural analysis was conducted to find the load on the pile cap, as well as the shear force and the bending moment at the section where the superstructure reaches the abutment. The superstructure-abutment system was considered as a single bi-supported beam subjected to its self-weight only. The beam self-weight was calculated assuming a unit weight of 25 kN/m³ for the reinforced concrete, according to TxDOT (2016).

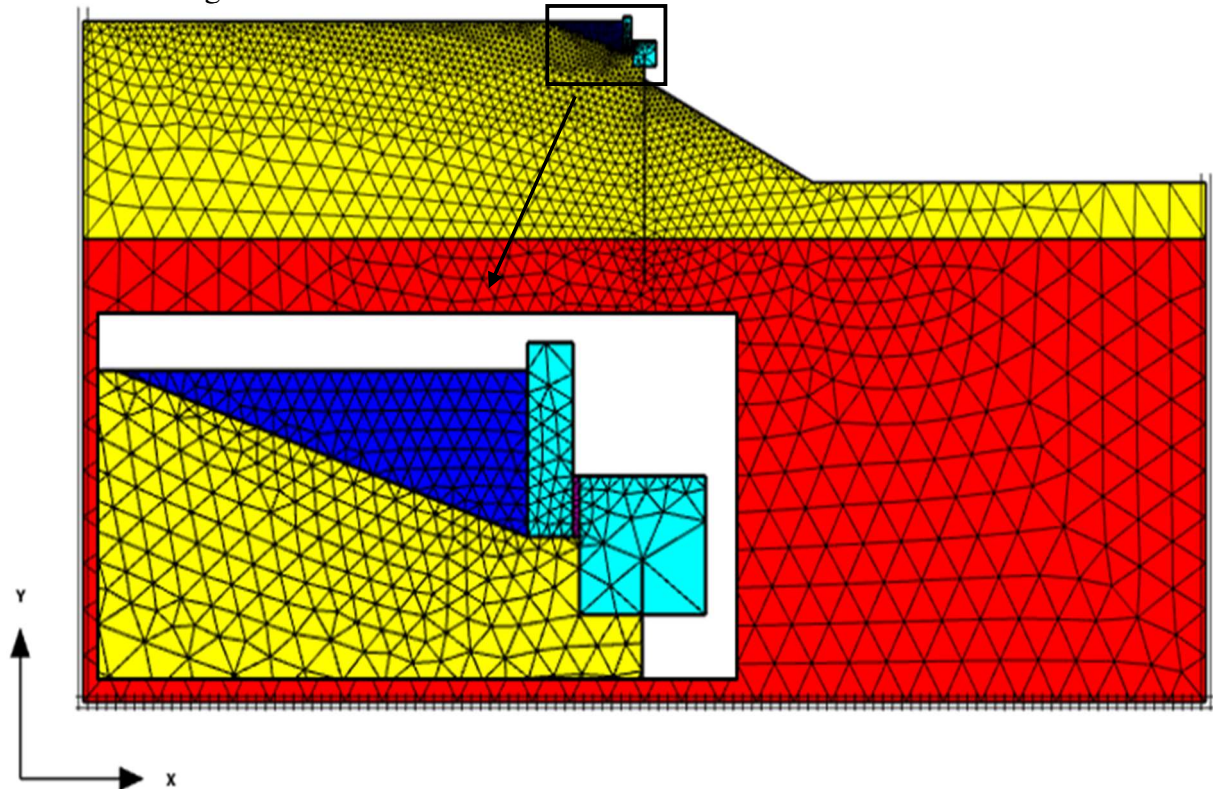
The bending moment's effect was represented in Plaxis by a horizontal two-point load of 2 kN/m, obtained dividing the bending moment by the height of the superstructure. The shear force was represented by a uniform vertical load of 12 kN/m/m, obtained dividing the shear force by the height of the superstructure. The superstructure-abutment system load was represented by a uniform vertical load of 150 kN/m/m, obtained dividing the structural support reaction by the width of the pile cap. The calculated bending moment and shear force were applied to the superstructure-abutment interface section, and the load from the superstructure-abutment system was applied to the top of the pile cap.

Prescribed horizontal displacements applied at the top of the abutment were used to represent the effects of expansion and contraction of the superstructure on the abutment due to temperature changes. This approach was used in recent numerical analysis studies (e. g.: AL-QARAWI; LEO; LIYANAPATHIRANA, 2020; BANKS; BLOODWORTH, 2018; BLOODWORTH et al., 2012; CARISTO; BARNES; MITOULIS, 2018; CARLSTEDT, 2008; EFRETUEI, 2013; MITOULIS et al., 2016) and was adopted herein to simplify the numerical modeling due to limited field instrumentation.

Prescribed horizontal displacements were applied at the top of the abutment. This position was chosen based on the fact that the greater variations in temperature in a bridge usually takes place at the top of the superstructure due to solar radiation (BARR; STANTON; EBERHARD, 2005; CHEN et al., 2009; DAVIDS et al., 2010; EMERSON, 1977; ENGLAND; TSANG; BUSH, 2000; HEDEGAARD; FRENCH; SHIELD, 2013; IMBSEN et al., 1985; KONG; CAI; KONG, 2015; KONG; CAI; ZHANG, 2016; RODRIGUEZ; BARR; HALLING, 2014; SHIU; TABATABAI, 1994; SONG; XIAO; SHEN, 2012; XUE et al., 2018). Temperature distribution in a vertical cross-section of the superstructure is maximum at the top

enough for obtaining accurate numerical results without leading to an excessive calculation length. Further details about the software Plaxis 2D version 2016 can be found in Brinkgreve, Kumarswamy and Swolfs (2016b). Figure 4.4 shows the finite element mesh used in the numerical simulations.

Figure 4.4 – Finite element mesh used in the numerical simulations.



Source: Elaborated by the author (2020).

4.2 Material properties

The stress-strain behavior of the soil materials was represented by the Hardening Soil (HS) hyperbolic constitutive model. The HS model is an elastoplastic type of advanced hyperbolic model, based on the Plasticity Theory, for simulating the behavior of different types of soils, both soft and stiff soils, which include soil dilatancy and a yield cap. In this constitutive model, irreversible strains due to primary deviatoric loading are modeled by shear hardening while irreversible plastic strains due to primary compression in oedometer loading and isotropic loading are modeled by compression hardening. Further details about the HS constitutive model can be found in Brinkgreve, Kumarswamy and Swolfs (2016a).

Soil parameters were obtained based on the results of the TCP test results presented in subsection 3.2, on the consolidated drained triaxial test results presented in subsection 3.3, and

on correlations and recommendations for typical values available in the technical literature (BOWLES, 1997; DUDERSTADT; COYLE; BARTOSKEWITZ, 1977; HAMOUDI; COYLE; BARTOSKEWITZ, 1974; KULHAWY; MAYNE, 1990; LAWSON et al., 2018; MESRI, 1975; POULOS; DAVIS, 1974; STROUD; BUTLER, 1975; TOMLINSON, 1993; TxDOT, 2020; VASUDEVAN, 2005; VIPULANANDAN et al., 2008).

Specifically, the undrained shear strength for the sandy clay layer was estimated as $4N_{60,SPT}$, as suggested by Stroud and Butler (1975), where $N_{60,SPT}$ is Standard Penetration Test (SPT) blowcount resistance corrected to 60% efficiency. $N_{60,SPT}$ was calculated as $0.5N_{TCP}$, as suggested by Lawson et al. (2018), where N_{TCP} is TCP blowcount resistance. The friction angle for the silty sand layer was estimated from the correlation proposed by TxDOT (2020).

Due to the limited native soil survey, proposed preliminary numerical simulations showed that the response of the backfill-abutment system was not significantly influenced by the refinements of the native soil parameters. Table 4.1 lists the soil parameters used to validate the numerical model.

Table 4.1 – Soil parameters used to validate the numerical model.

Parameter	Unit	Sandy clay	Silty sand	Gravel
Unsaturated unit weight (γ_{unsat})	kN/m ³	19	17	20
Saturated unit weight (γ_{sat})	kN/m ³	22	20	23
Secant stiffness in standard drained triaxial test (E_{50}^{ref})	MPa	60	40	30
Tangent stiffness for primary oedometer loading ($E_{oed}^{ref} = E_{50}^{ref}$)	MPa	60	40	30
Unloading/loading stiffness ($E_{ur}^{ref} = 3E_{50}^{ref}$)	MPa	180	120	90
Undrained shear strength at reference level ($S_{u,ref}$)	kPa	210	-	-
Effective cohesion (c'_{ref})	kPa	-	15	1
Effective friction angle (ϕ')	°	-	31.5	40

Source: Elaborated by the author (2020).

The soil parameters were associated with the reference stress for stiffness (p^{ref}) equal to 100 kPa, which is the default value of the Plaxis software (BRINKGREVE; KUMARSWAMY; SWOLFS, 2016a). A dilatancy angle equal to zero was adopted for the silty sand layer and the gravel backfill because they were loose to slightly compacted materials. The power for the stress-level dependency of stiffness (m) was assumed to be equal to 0.5, as suggested by Duncan and Chang (1970), Janbu (1963), Lade and Nelson (1987) and Schanz and Vermeer (1998). Undrained conditions were assumed for the sandy clay layer while drained

conditions were assumed for the silty sand layer and the gravel backfill. Non-porous conditions were assumed for the reinforced concrete and the PBFM.

The stress-strain behavior of the structural materials was represented by the linear elastic constitutive model. Different sources were consulted to define parameters for the structural materials due to the absence of laboratory tests (AASHTO, 2012; CAI; ROSS, 2010; GERDAU, 2019; MAHENDRAN, 1996; PERIC et al., 2016; SUCHSLAND; WOODSON, 1987; TxDOT, 2016). Table 4.2 lists the structural parameters used to validate the numerical model.

Table 4.2 – Structural parameters used to validate the numerical model.

Parameter	Unit	Reinforced concrete	PBFM	Foundation	Anchor
Unit weight (γ)	kN/m ³	25	10	-	-
Young's modulus (E)	GPa	30	4	-	-
Poisson's ratio (ν)	-	0.2	0.2	0.3	-
Normal stiffness (EA) – Plate	kN/m	-	-	3.16×10^6	-
Flexural rigidity (EI)	kNm ² /m	-	-	7.33×10^4	-
Weight (w)	kN/m/m	-	-	1.18	-
Normal stiffness (EA) – Anchor	kN	-	-	-	2.99×10^6
Out-of-plane spacing (L_{spacing})	m	-	-	-	2.62

Source: Elaborated by the author (2020).

4.3 Approach for calculating the prescribed horizontal displacements

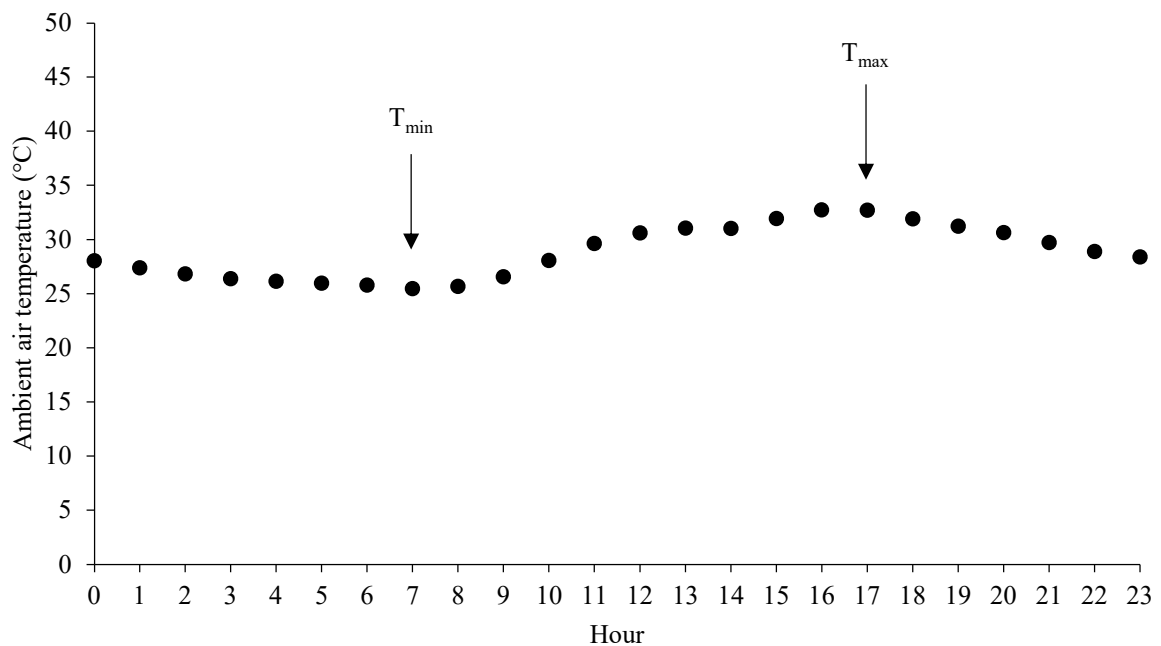
As suggested by AASHTO (2012), the variation of the bridge length (ΔL) was estimated by $\Delta L = \alpha L \Delta T$, where α is the thermal expansion coefficient of the bridge material, L is the bridge length, and ΔT is the bridge temperature variation. In the absence of laboratory tests or more precise data, a coefficient of thermal expansion of $10.8 \times 10^{-6} / ^\circ\text{C}$ was assumed for the concrete, which is within the range recommended by AASHTO (2012). The prescribed horizontal displacements were calculated by dividing ΔL by two. This assumption is believed to be in accordance with field conditions since both north and south backfills were built with the same material and compaction degree (TxDOT, 2016), thus leading to equivalent displacements. The same approach was used by Banks and Bloodworth (2018), Bloodworth et al. (2012), Civjan et al. (2007), and Karalar and Dicleli (2018).

As reported by Emerson (1977), England, Tsang and Bush (2000), Hoffman, McClure and West (1983), Imbsen et al. (1985), Lee (1994), Moorty and Roeder (1992), Potgieter and

Gamble (1989) and Thepchatri, Johnson and Matlock (1977), the most significant factors affecting the bridge temperature are solar radiation, ambient air temperature, wind speed, precipitation and structural material thermal properties. Combinations of these factors can produce situations in which the bridge temperature is not necessarily equal to the ambient air temperature. Consequently, bridge temperature and associated horizontal displacements can be very complex to predict.

Due to limited field instrumentation, and to simplify the complex interaction mechanisms of heat transfer and flow involving the bridge and the surrounding environment, bridge temperature variations were assumed to equal ambient air temperature variations. ΔT values were calculated from minimum and maximum daily temperatures recorded by the temperature sensors. As an example, Figure 4.5 presents hourly ambient air temperatures recorded on July 14, 2017. In the first hours of the day, the temperature followed a descending path until reaching a minimum value (T_{\min}). Then, the temperature increased until reaching a maximum value (T_{\max}). Horizontal displacements pushing the abutment against the backfill were calculated using the difference between T_{\min} and T_{\max} of the current day, while horizontal displacements pulling the abutment away from the backfill were calculated using the difference between T_{\max} of the current day and T_{\min} of the next day.

Figure 4.5 – Ambient air temperatures recorded on July 14, 2017.



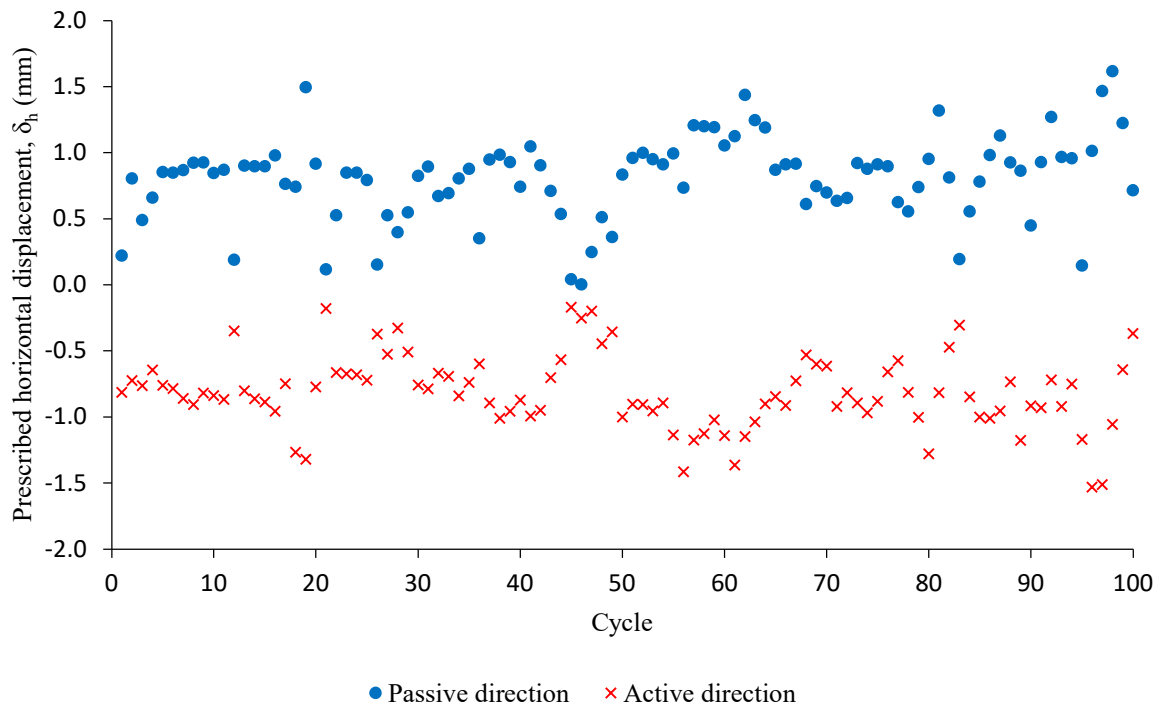
Source: Elaborated by the author (2020).

5 BACKFILL-ABUTMENT SYSTEM NUMERICAL RESPONSE

5.1 Numerical model validation

The proposed numerical model was validated based on the field data collected by Walter (2018). Calculation data were restricted to a 100-day period, counted from the beginning of the field monitoring, to avoid long computational periods. The numerical simulation was performed by applying prescribed horizontal displacements (δ_h) to the abutment, as to represent the cyclic lateral displacements of the abutment due to daily maximum expansions and contractions of the bridge. Figure 5.1 shows δ_h values calculated via the approach described in subsection 4.3. A positive sign is assigned to lateral displacements pushing the abutment against the backfill (passive direction) while a negative sign means that the lateral displacements pull the abutment away from the backfill (active direction). As shown in Figure 5.1, in general, the calculated displacements ranged within ± 1 mm, which represents $\pm 0.1\%$ of the abutment height.

Figure 5.1 – Prescribed horizontal displacements used to validate the numerical model.



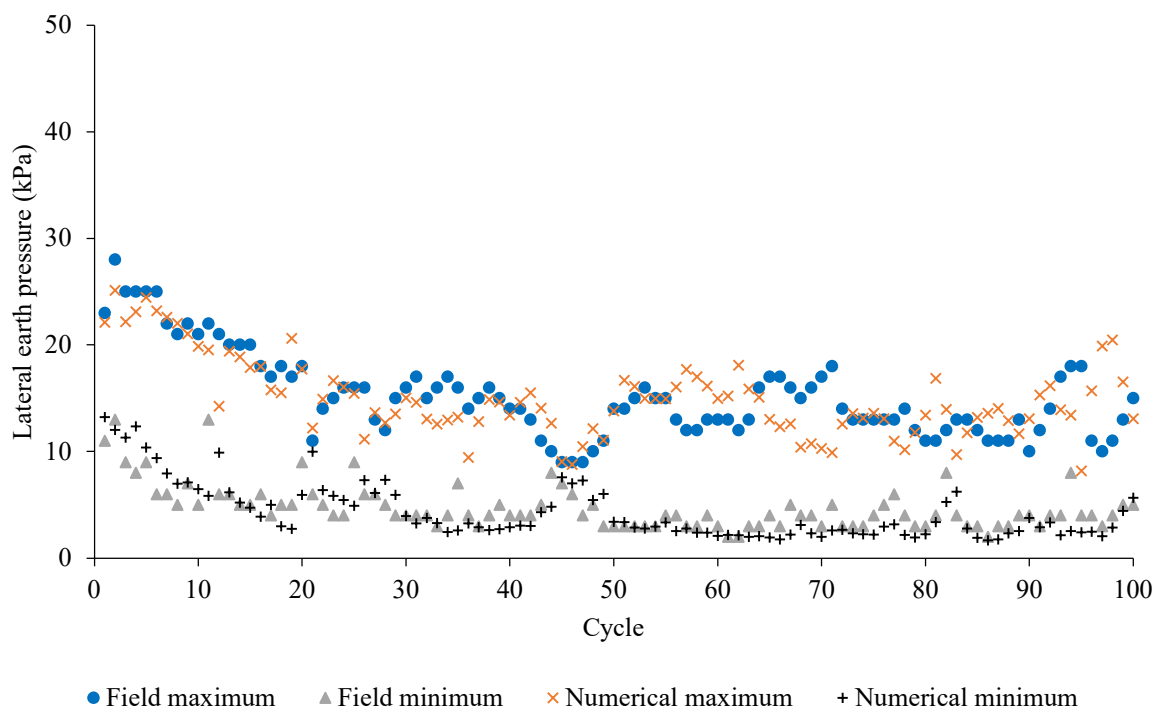
Source: Elaborated by the author (2020).

The maximum and minimum daily cyclic lateral earth pressures measured in the field are compared with the numerical predictions in Figure 5.2. The numerical values represent the average of stresses in eleven stress points on the backfill-abutment interface, as to coincide with

the same vertical positions of the pressure cells in the field. The numerical and field lateral earth pressures are also compared in a 1:1 chart, as shown in Figure 5.3. The relationship between numerical predictions and field measurements yielded a coefficient of Pearson product-moment correlation (r) of 0.905, which represents a coefficient of determination (r^2) of 0.82. According to Salkind (2017), the r value assesses the relationship between two continuous variables, and the r^2 value represents the variance percentage in one variable that can be explained by the variance in the other variable. In this case, $r = 0.905$ corresponds to a very strong relationship (SALKIND, 2017) between the numerical prediction and field measurement. Moreover, the obtained r^2 value means that 82% of the variance in the numerical prediction is accounted for by the variance in the field measurement.

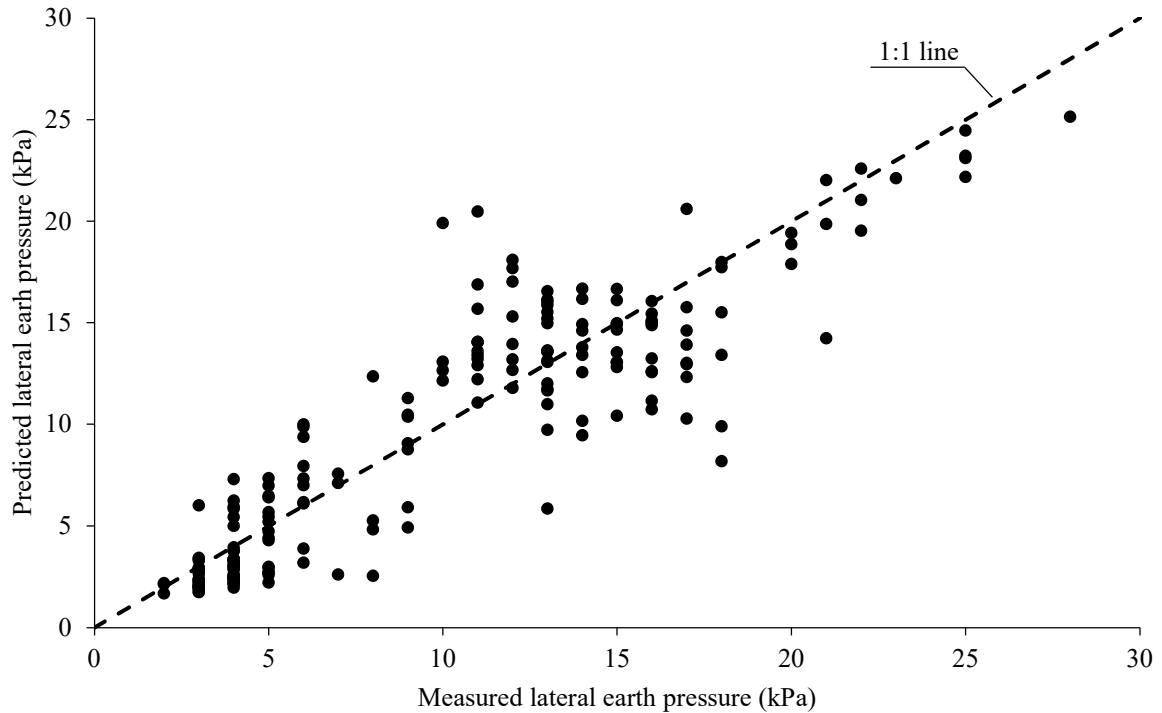
Additional numerical simulations were carried out with strength reduction factors (R_{inter}) equal to 0.1, 0.3, 0.5, and 0.9. The r and r^2 values produced by these numerical simulations were compared with the r and r^2 values produced by the numerical simulation with $R_{\text{inter}} = 0.7$ (Table 5.1) to analyze the influence of R_{inter} in the numerical model validation. The results showed that the best relationship between numerical predictions and field measurements was obtained with $R_{\text{inter}} = 0.7$. Therefore, the numerical model validation can be considered satisfactory, given the many variables and inherent imprecision involved in the whole calibration process.

Figure 5.2 – Comparison between field and numerical lateral earth pressures.



Source: Elaborated by the author (2020).

Figure 5.3 – Dispersion of the lateral earth pressures.



Source: Elaborated by the author (2020).

Table 5.1 – Relationship between numerical predictions and field measurements for different values of R_{inter} .

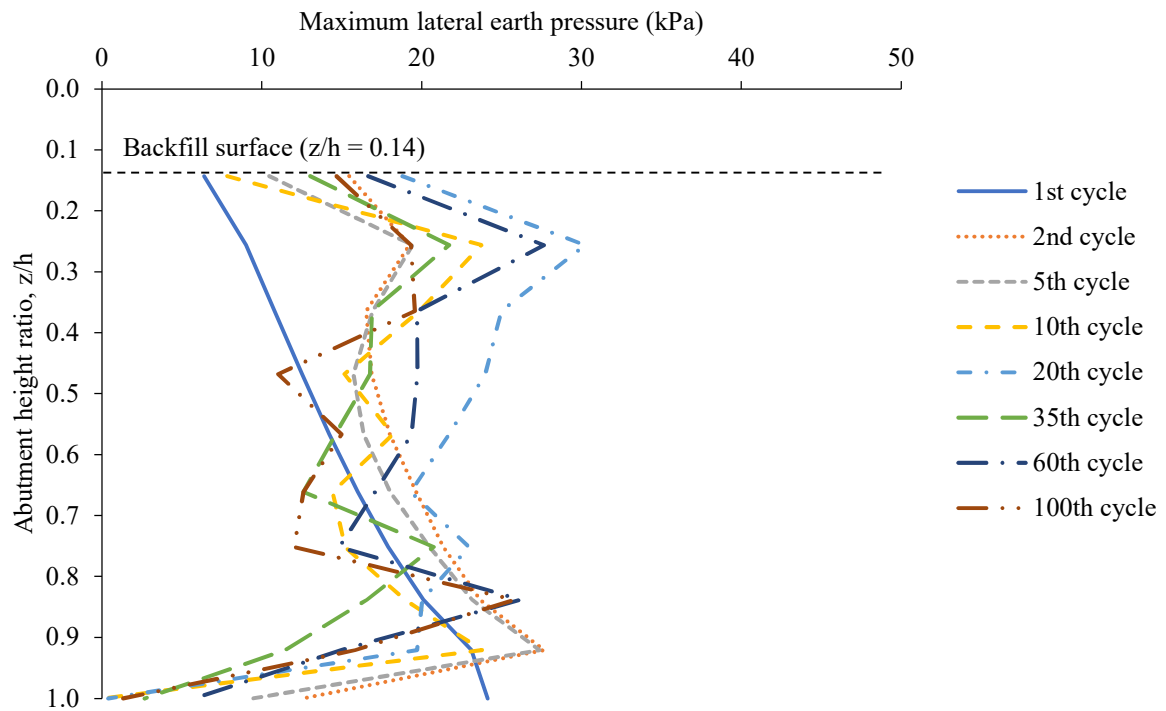
R_{inter}	r	r^2	Variance	Relationship (SALKIND, 2017)
0.1	0.14	0.02	2%	Weak or no relationship
0.3	0.34	0.12	12%	Weak relationship
0.5	0.35	0.12	12%	Weak relationship
0.7	0.91	0.82	82%	Very strong relationship
0.9	0.20	0.04	4%	Weak or no relationship

Source: Elaborated by the author (2020).

5.2 Analysis of the daily cyclic response

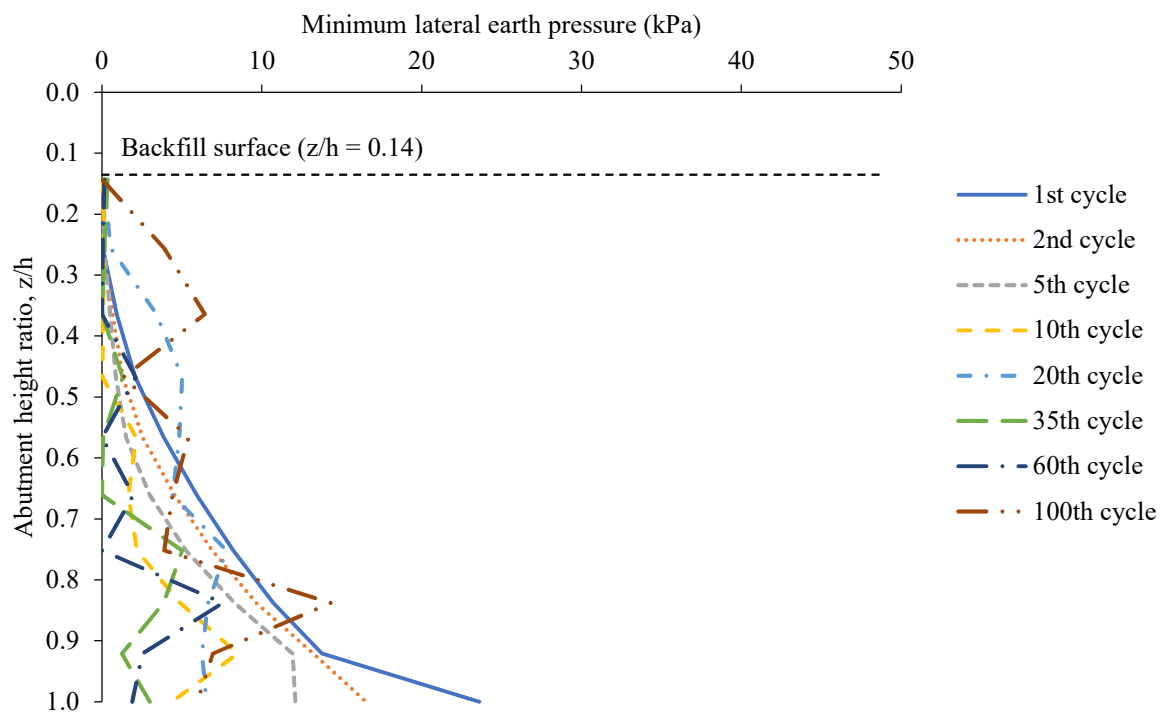
Analysis of the response of the backfill-abutment system upon daily cyclic lateral displacements of the abutment was carried out after validation of the numerical model. Figures 5.4 and 5.5 show, respectively, the maximum and minimum lateral earth pressures as a function of the abutment height ratio (z/h), where z is the depth measured from the top of the abutment, and h is the abutment height, for selected daily cycles.

Figure 5.4 – Distributions of maximum lateral earth pressures along the abutment height for selected daily cycles.



Source: Elaborated by the author (2020).

Figure 5.5 – Distributions of minimum lateral earth pressures along the abutment height for selected daily cycles.



Source: Elaborated by the author (2020).

The lateral earth pressures presented a nonlinear distribution along the abutment height. In general, larger values of maximum lateral earth pressures occurred within the upper and bottom thirds of the abutment while larger values of minimum lateral earth pressures occurred within the bottom third of the abutment. Particularly, the minimum lateral earth pressures were nearly zero within the upper third of the abutment. No simplified shape for the distributions of maximum and minimum lateral earth pressures could expressly be identified. Similar profiles have been obtained elsewhere by physical measurements and numerical simulations (ABDEL-FATTAH; ABDEL-FATTAH, 2019; ABDEL-FATTAH; ABDEL-FATTAH; HEMADA, 2018; PAIK; SALGADO, 2003; XU; LIU, 2019).

Diagrams with a linear shape or with a regular geometric shape have been proposed by most conventional methods for predicting lateral earth pressures (CLOUGH; DUNCAN, 1991). For example, AASHTO (2012) suggests that lateral earth pressures should be assumed linearly proportional to soil depth considering lateral earth pressure coefficients calculated from Coulomb or Rankine's Theories. However, physical measurements and numerical simulations have revealed nonlinear lateral earth pressure distributions on abutments undergoing cyclic lateral displacements (ABDEL-FATTAH, M.; ABDEL-FATTAH, T., 2019; ABDEL-FATTAH, M.; ABDEL-FATTAH, T.; HEMADA, 2018; BANKS; BLOODWORTH, 2018; CARISTO; BARNES; MITOULIS, 2018; CIVJAN et al., 2013; HUNTLEY; VALSANGKAR, 2013; KIM et al., 2014; LEHANE, 2011; MITOULIS et al., 2016; XU; LIU, 2019). The nonlinear distributions observed for the lateral earth pressures can be related to the transfer of stresses between the backfill and the abutment due to soil-structure interface friction. This transfer of stresses is commonly known as arching in soils and results in nonlinear distributions of lateral earth pressures on the abutment (COSTA; ZORNBERG, 2020; HANDY, 1985; PAIK; SALGADO, 2003; TERZAGHI, 1943).

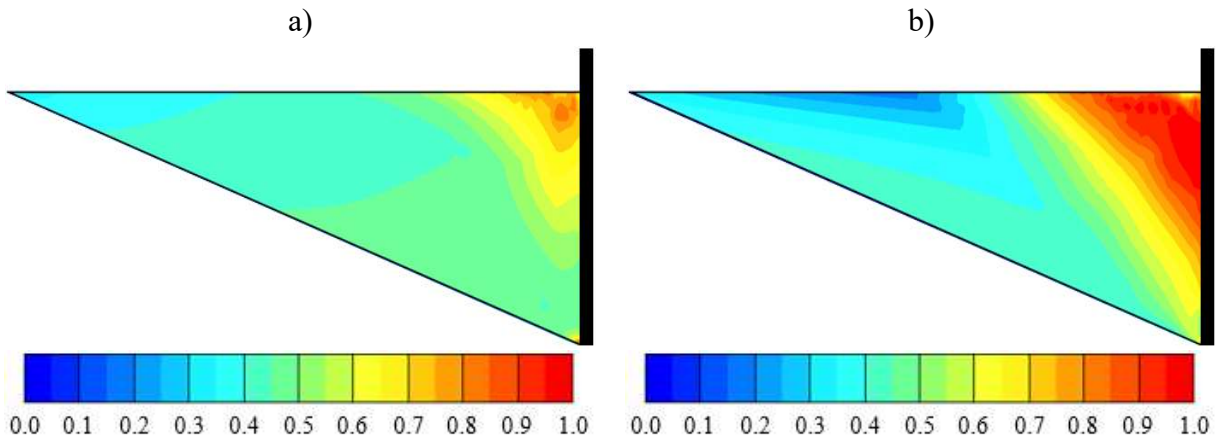
The obtained lateral earth pressure profiles can be related to the lateral displacement amplitude of the abutment. The imposed displacement amplitude was not enough to overcome the shear strength of the backfill and slip upward a soil portion toward the backfill surface during the passive direction. Therefore, since the largest lateral displacements were imposed at the top of the abutment, the maximum lateral earth pressures within the upper third of the abutment were more affected by the cyclic lateral displacements, which can justify the obtained profiles for maximum lateral earth pressures. On the other hand, the imposed displacement amplitude was enough to overcome the shear strength of the backfill and slip downward a soil portion toward the gap developed between the abutment and the backfill during the active direction. Therefore, the soil near the upper third of the abutment was displaced toward the

bottom third of the abutment, which can explain the obtained profiles for minimum lateral earth pressures.

The previously mentioned behavior can be observed from shadings of relative shear stress (τ_{rel}), as shown in Figure 5.6, arrows of resultant displacement (u_{res}), as presented in Figure 5.7, and shadings of deviatoric strain (γ_s), as shown in Figure 5.8. τ_{rel} gives an indication of the proximity of the stress point to the failure envelope and is defined as the ratio between the maximum value of mobilized shear stress (τ_{mob}) and the maximum value of shear stress for the case where the Mohr's circle is expanded to touch the Coulomb's failure envelope with the center of Mohr's circle constant (τ_{max}). u_{res} indicates the direction of movement of the soil elements. γ_s is defined as $\sqrt{\frac{2}{3} \left[\left(\epsilon_x - \frac{\epsilon_v}{3} \right)^2 + \left(\epsilon_y - \frac{\epsilon_v}{3} \right)^2 + \left(\epsilon_z - \frac{\epsilon_v}{3} \right)^2 + \frac{1}{2} (\gamma_{xy}^2 + \gamma_{yz}^2 + \gamma_{zx}^2) \right]}$, where ϵ_x is the axial strain in x-direction, ϵ_y is the axial strain in y-direction, ϵ_z is the axial strain in z-direction, ϵ_v is the volumetric strain, γ_{xy} is the shear strain in xy-plane, γ_{yz} is the shear strain in yz-plane, and γ_{zx} is the shear strain in zx-plane.

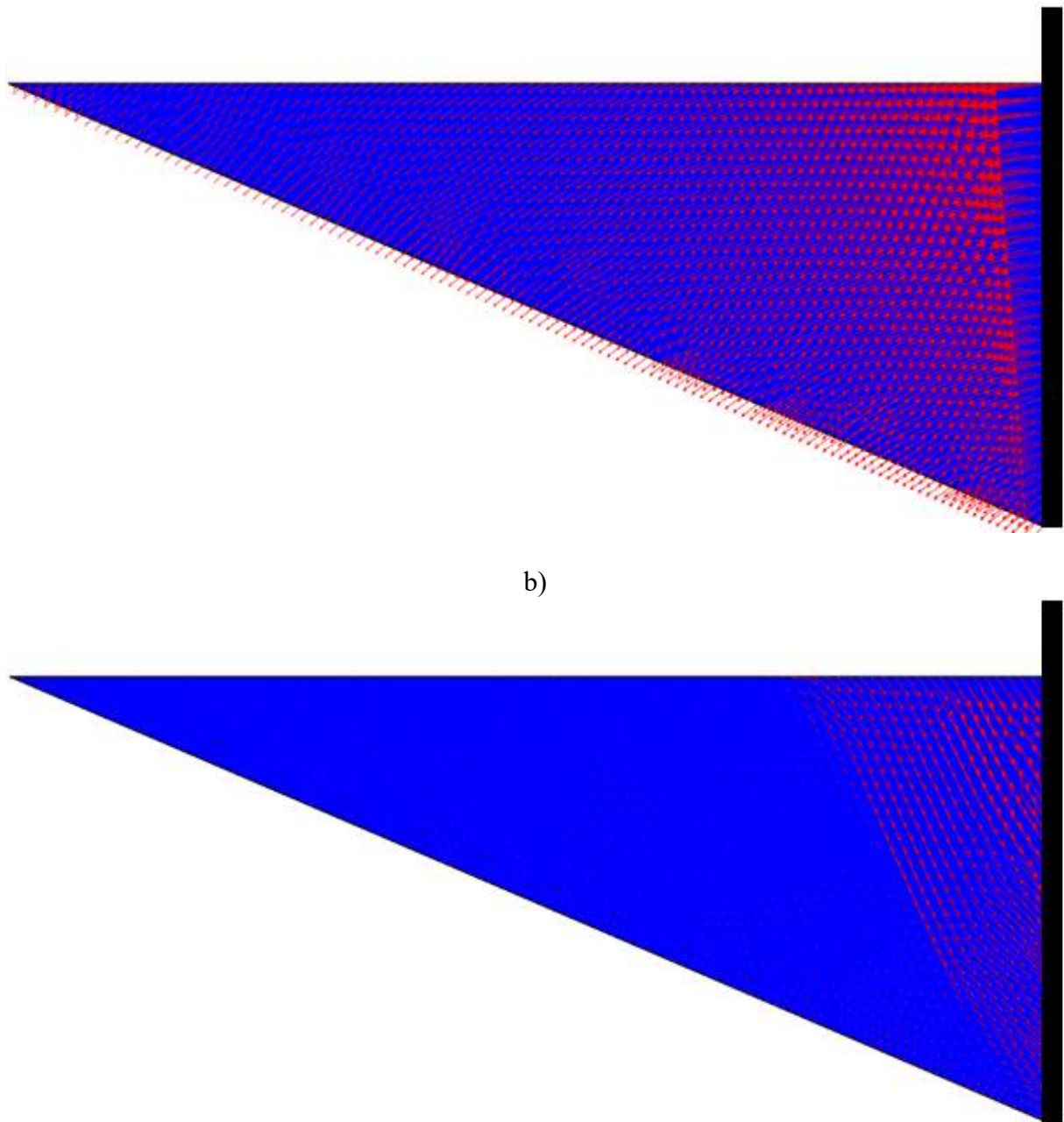
The shadings show that τ_{rel} was less than one ($\tau_{mob} < \tau_{max}$) in the whole backfill for the passive direction, which indicates the absence of soil failure. On the other hand, for active direction, τ_{rel} was equal to one ($\tau_{mob} = \tau_{max}$) in a zone of the backfill near the upper third of the abutment while τ_{rel} was less than one ($\tau_{mob} < \tau_{max}$) in the other zones of the backfill, which indicates a potential zone of soil failure near the upper third of the abutment. The arrows demonstrate that, during the passive direction, the soil was not displaced toward the backfill surface. During the active direction, the soil was displaced toward the bottom third of the abutment. The shadings also show that, with the cycles, a shear band was formed at a certain distance from the abutment, indicating a sliding surface.

Figure 5.6 – Shadings of relative shear stress in the backfill for a typical daily cycle: a) passive direction; b) active direction.



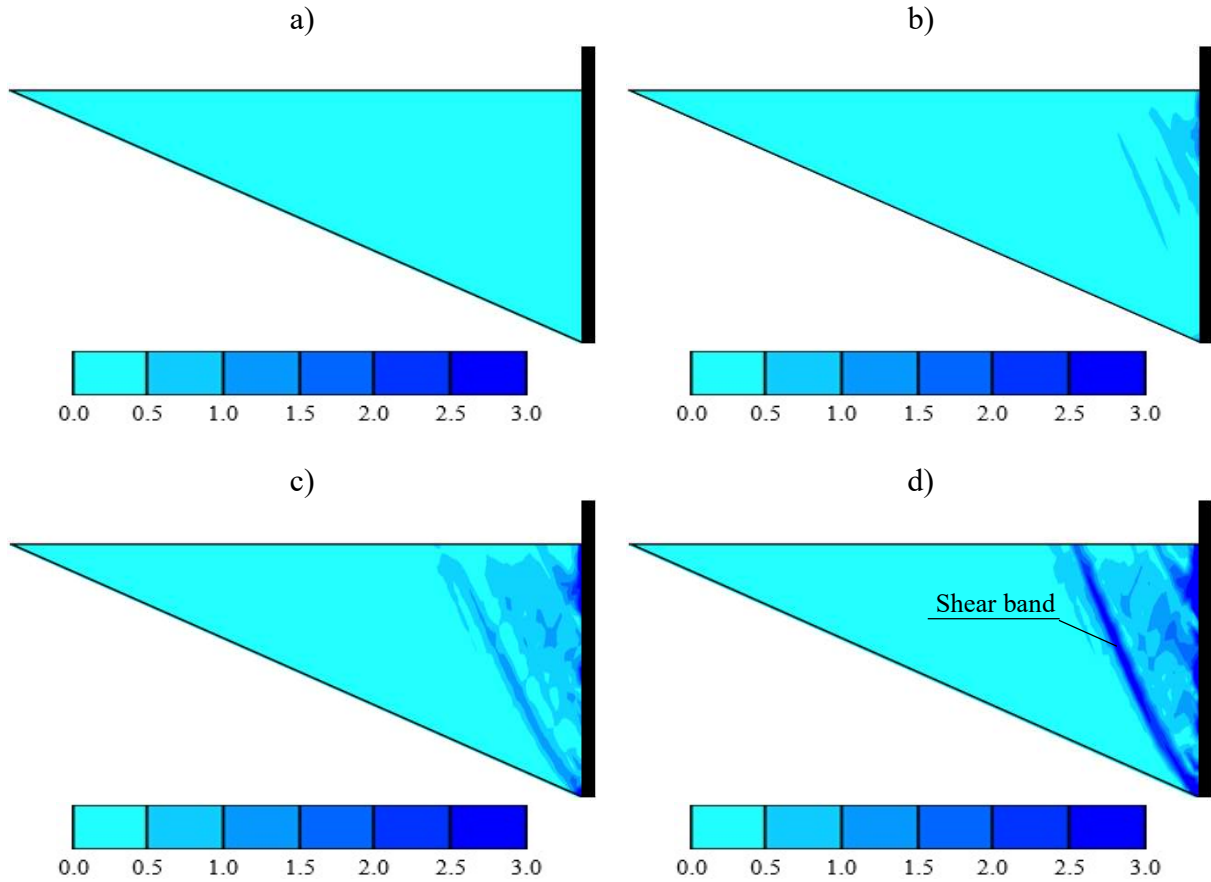
Source: Elaborated by the author (2020).

Figure 5.7 – Arrows of resultant displacement in the backfill for a typical daily cycle: a) passive direction; b) active direction.



Source: Elaborated by the author (2020).

Figure 5.8 – Shadings of accumulated deviatoric strain (in %) in the backfill at the end of selected daily cycles: a) 1st cycle; b) 33rd cycle; c) 66th cycle; d) 100th cycle.



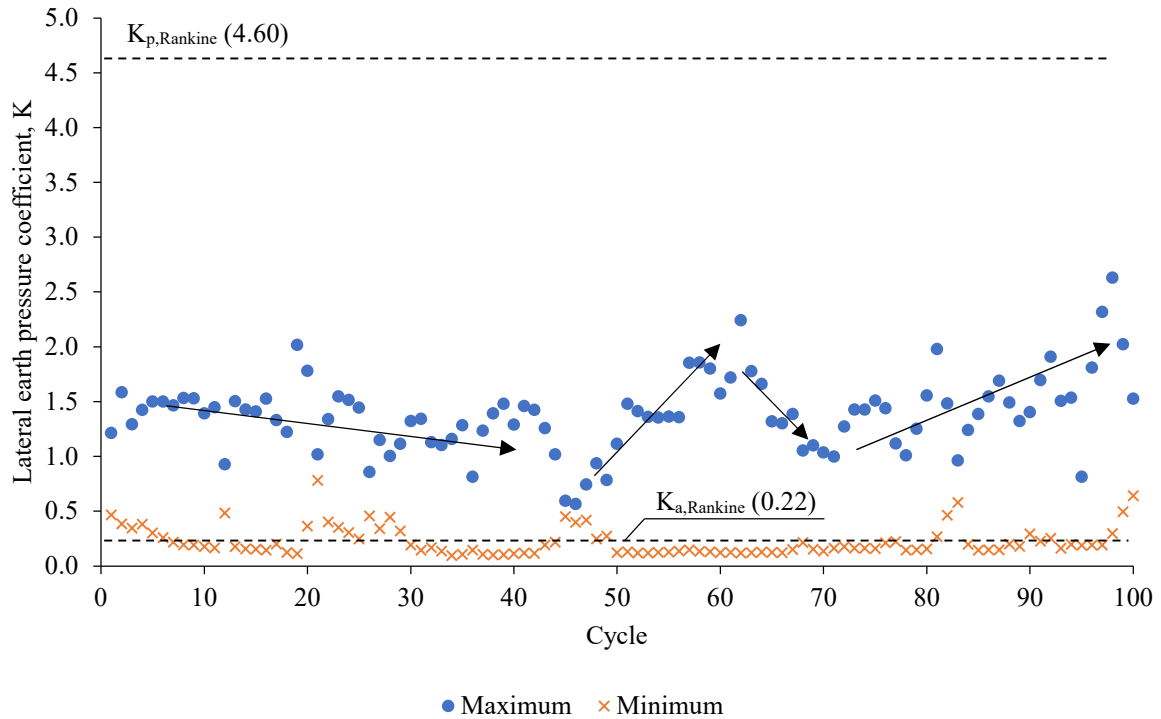
Source: Elaborated by the author (2020).

The lateral earth pressure coefficient (K) was calculated to assess the behavior of the lateral earth pressures with the daily cycles. K values were calculated by dividing the total lateral soil force acting on the abutment by the total lateral soil force of a triangular hydrostatic stress distribution acting over the height of the abutment (ENGLAND; TSANG; BUSH, 2000). Figure 5.9 shows K values calculated for daily cycles.

The maximum lateral earth pressure coefficient (K_{\max}) remained below Rankine's passive lateral earth pressure coefficient ($K_{p,\text{Rankine}}$) throughout the entire analyzed cycles, while the minimum lateral earth pressure coefficient (K_{\min}) remained close to Rankine's active lateral earth pressure coefficient ($K_{a,\text{Rankine}}$) for almost the entire analyzed cycles. Trends for the K_{\max} and K_{\min} behavior could be identified as the cycles went by. K_{\max} firstly presented a slight downward trend within the first 46 cycles. Then, K_{\max} increased until the 62nd cycle and reduced until the 71st cycle. Lastly, K_{\max} showed a slight upward trend from the 72nd cycle. The tendencies identified for K_{\min} were firstly characterized by a decrease within the first 10 cycles. Finally, K_{\min} became virtually constant from the 11th cycle, with some minor scattering.

Variation of K_{\max} and K_{\min} can be associated with the changes of δ_h due to temperature fluctuations since the daily temperature variations are not constant. Furthermore, K_{\min} was less affected by the cyclic lateral displacements of the abutment than K_{\max} .

Figure 5.9 – Lateral earth pressure coefficients for daily cycles.



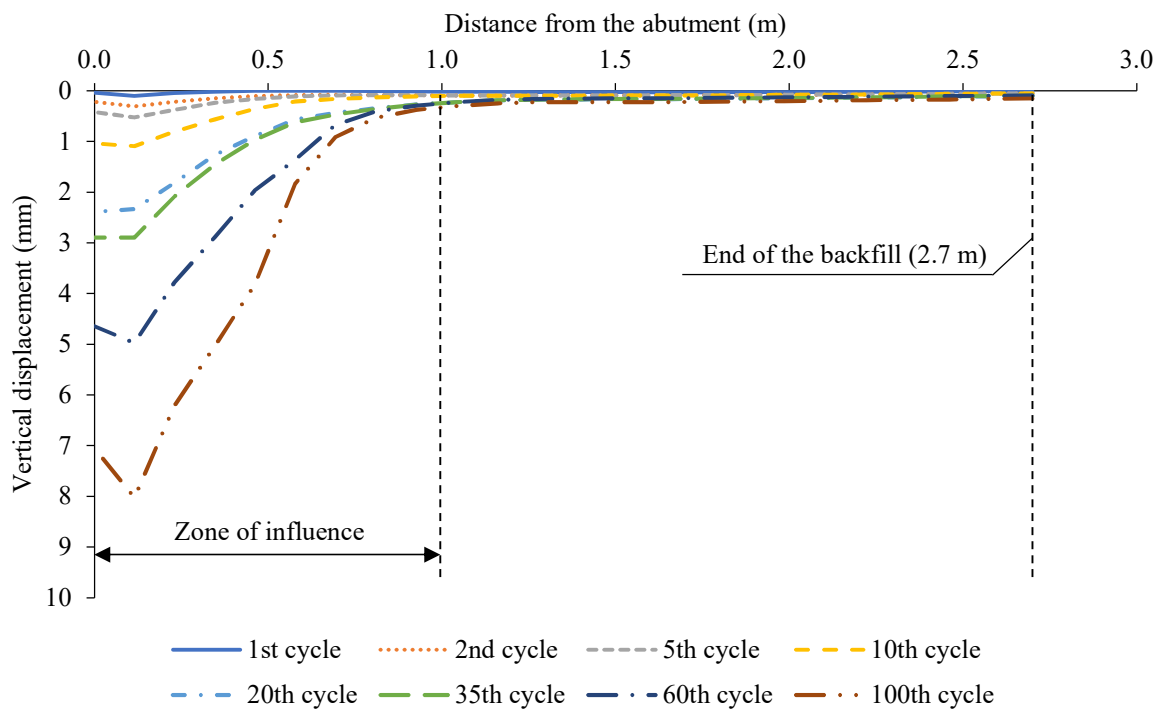
Source: Elaborated by the author (2020).

Physical measurements and numerical simulations have shown that maximum lateral earth pressures are more affected by cyclic lateral displacements of the abutment than minimum lateral earth pressures (AL-QARAWI; LEO; LIYANAPATHIRANA, 2020; BANKS; BLOODWORTH, 2018; CLAYTON; XU; BLOODWORTH, 2006; ENGLAND; TSANG; BUSH, 2000; HUNTLEY; VALSANGKAR, 2013; KIM; LAMAN, 2012; LEHANE, 2011; TATSUOKA et al., 2009; XU; CLAYTON; BLOODWORTH, 2007; ZADEHMOHAMAD; BAZAZ, 2019). This probably happens due to the magnitude of lateral displacement required to reach the passive and active failure states. According to Clough and Duncan (1991) and Hambly and Burland (1979), the active failure state takes place for a magnitude of lateral displacement equal to approximately 10% of the magnitude required for mobilizing the passive failure state. This difference is mainly associated with the different confining pressures in the two failure states (ENGLAND; TSANG; BUSH, 2000), which allows that the active failure

state takes place long before the passive failure state in granular backfills upon cyclic loading (TATSUOKA et al., 2009).

Vertical displacement profiles of the backfill surface along the distance from the abutment for selected daily cycles were also analyzed (Figure 5.10). Displacements were obtained at the end of each cycle. In the figure, the downward vertical displacement (settlement) is taken as positive. The largest settlement occurred near the backfill-abutment interface and decreased with increasing distance from the abutment. According to the profiles, settlements were more influenced by the cyclic lateral displacements within a zone with dimension equal to abutment height measured from the abutment. The settlement within this zone increased with the cycles, what indicates the presence of ratcheting. Moreover, no tendency of upward vertical displacement (heave) was observed on the backfill surface, what indicates the absence of the soil granular flow as defined by England, Tsang and Bush (2000).

Figure 5.10 – Vertical displacement profiles of the backfill surface along the distance from the abutment for selected daily cycles.

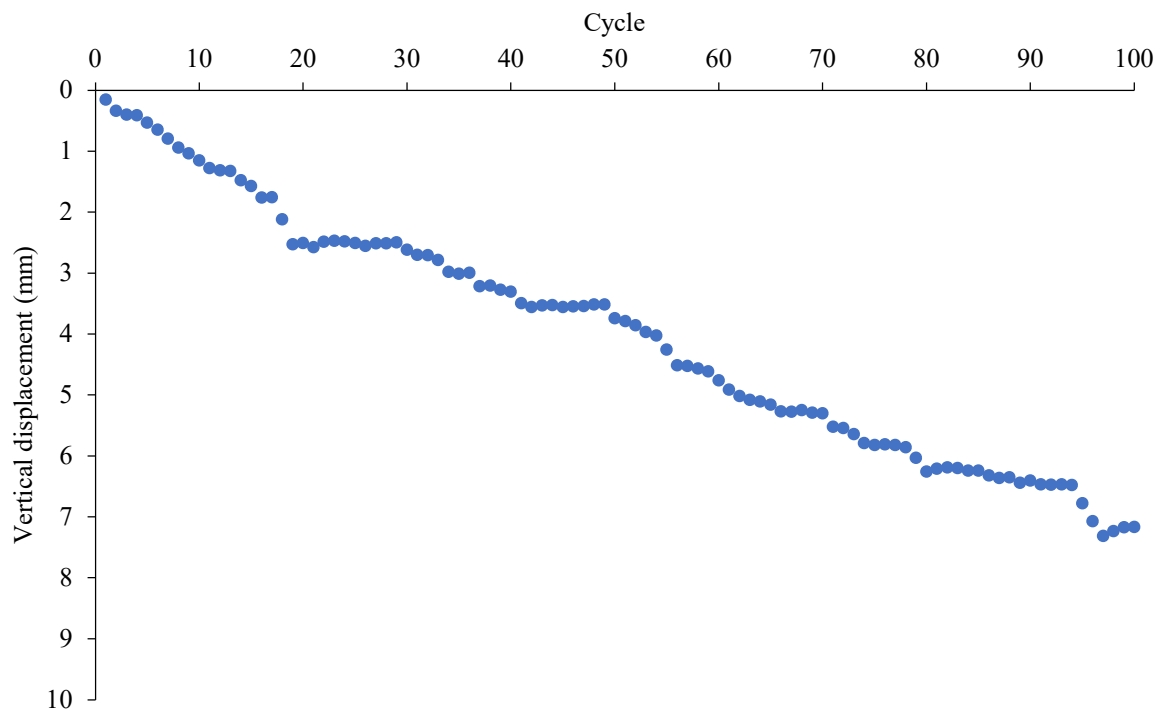


Source: Elaborated by the author (2020).

Figure 5.11 shows the vertical displacements at the top of the backfill-abutment interface for daily cycles. The settlement increased with the cycles according to a nonlinear fashion with a slight decreasing rate. No tendency of stabilization (steady state) could expressly be identified with increasing cycles. Results of laboratory experiments and numerical

simulations have shown a similar behavior for the vertical displacement of the backfill surface (AL-QARAWI; LEO; LIYANAPATHIRANA, 2020; ARGYROUDIS et al., 2016; CARISTO; BARNES; MITOULIS, 2018; DAVID; FORTH; YE, 2014; ENGLAND; TSANG; BUSH, 2000; MITOULIS et al., 2016; MUNOZ et al., 2012; TATSUOKA et al., 2009; ZADEHMOHAMAD; BAZAZ, 2019).

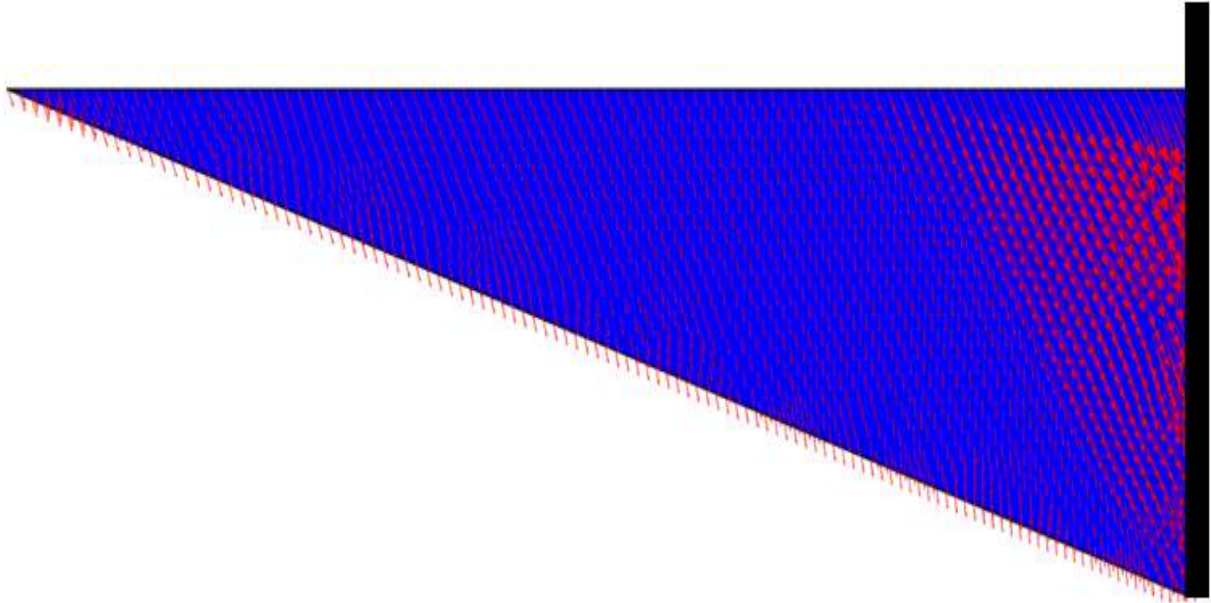
Figure 5.11 – Vertical displacements at the top of the backfill-abutment interface for daily cycles.



Source: Elaborated by the author (2020).

As discussed in subsection 2.3, the backfill surface is expected to present settlement and heave due to cyclic lateral loading. However, no heave was observed in the vertical displacement profiles of the backfill surface, as shown in Figure 5.10. The obtained profiles can be explained by the influence of the lateral displacement amplitude of the abutment. In this case, the displacement amplitude was sufficient to densify the soil near the backfill-abutment interface, but not enough to produce a soil granular flow that could raise the backfill surface. This characteristic can be noted in Figure 5.12, which shows arrows of accumulated resultant displacement after the daily cyclic lateral loading. The arrows show that the whole backfill displaced downward, which indicates the absence of the soil granular flow defined by England, Tsang and Bush (2000).

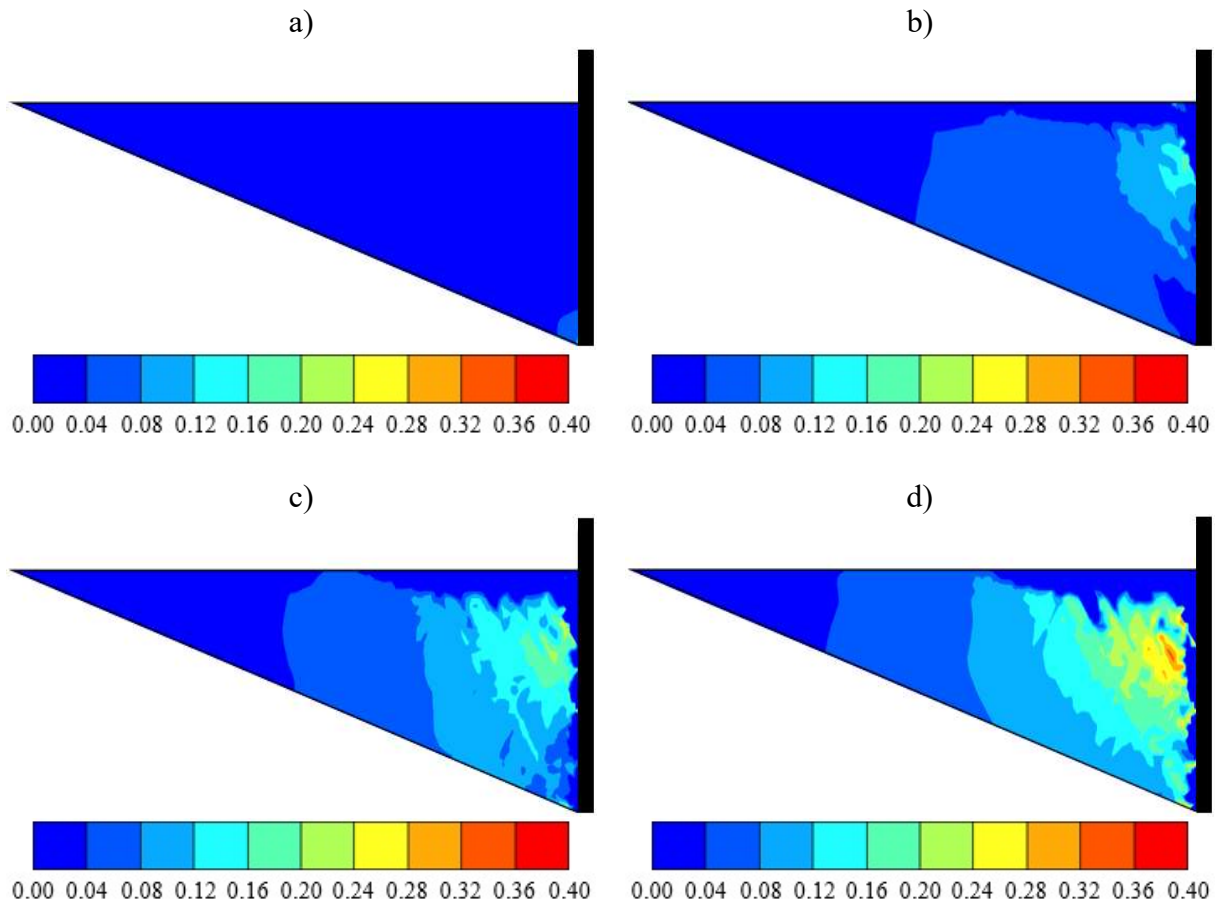
Figure 5.12 – Arrows of accumulated resultant displacement in the backfill after the daily cyclic lateral loading.



Source: Elaborated by the author (2020).

However, the displacement amplitude was not sufficient to cause the maximum densification of the backfill, what can explain the continuous settlement increase shown in Figure 5.11. On the other hand, the decreasing rate of the settlement with the cycles can be related to soil densification. Densification of the soil gradually increased the backfill stiffness with the cycles, reducing the settlement increment at each cycle. The densification of the backfill is shown in Figure 5.13, which presents shadings of accumulated compressive volumetric strain in the backfill at the end of selected daily cycles. The shadings show that larger compressive volumetric strains occurred near the backfill-abutment interface and decreased with distance from the abutment, which can justify the profiles presented in Figure 5.10. Moreover, the increase of the compressive volumetric strains with the cycles indicates the presence of ratcheting and can explain the continuous increase in the vertical displacement of the backfill surface (Figure 5.11).

Figure 5.13 – Shadings of accumulated compressive volumetric strain (in %) in the backfill at the end of selected daily cycles: a) 1st cycle; b) 33rd cycle; c) 66th cycle; d) 100th cycle.



Source: Elaborated by the author (2020).

5.3 Analysis of the annual cyclic response

Analysis of the response of the backfill-abutment system upon annual cyclic lateral displacements of the abutment is presented in this subsection. AASHTO (2012) recommends designing permanent retaining walls for a minimum service life of 75 years for most applications and 100 years for a greater level of safety and/or longer service life for retaining walls supporting bridge abutments. This means that the bridge would be subjected to a minimum of 75 or 100 cycles of annual thermal variation, depending on the considered design condition. The present analysis included 100 annual cycles of lateral displacement of the abutment.

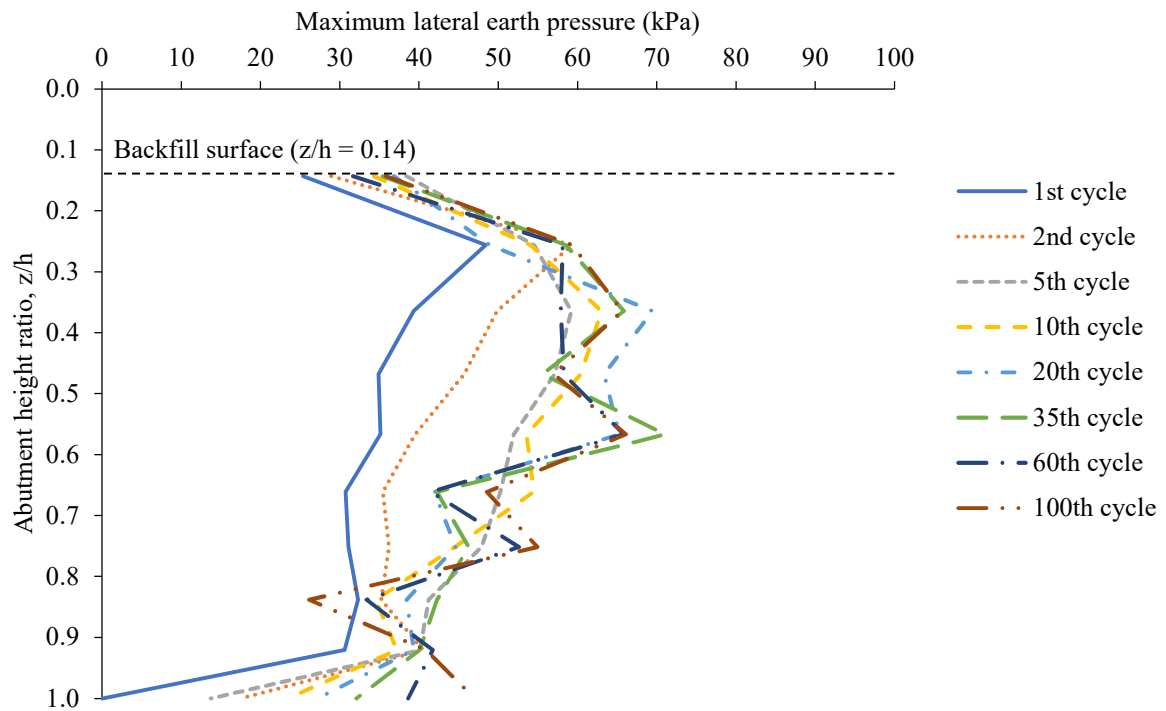
Since the bridge was completed in the summer season, it initially contracted until the winter season, when it reached its minimum longitudinal length. Then, the bridge expanded until the summer season of the next year, completing the annual cycle. Following this rationale, at new each annual cycle, the abutment was firstly displaced away from the backfill, and then

it was displaced towards the backfill. This scenario was modeled by applying cycles of δ_h equal to 5 mm to represent the cyclic lateral displacements of the abutment due to annual maximum expansions and contractions of the bridge. The value of 5 mm was calculated via the approach described in subsection 4.3, considering a temperature variation of 45 °C, as recommended by AASHTO (2012) for the location where the bridge was built.

Figures 5.14 and 5.15 show, respectively, the maximum and minimum lateral earth pressures as a function of the abutment height ratio for selected annual cycles. In general, the largest values of maximum lateral earth pressures occurred within the middle third of the abutment, while the largest values of minimum lateral earth pressures occurred within the bottom third of the abutment. Particularly, the lateral earth pressures for the active condition were nearly zero within the upper third of the abutment. The distributions of maximum lateral earth pressures can be approximated by a bi-linear shape with the largest pressures occurring within the middle third of the abutment. The distributions of minimum lateral earth pressures can be described by a triangular shape with the largest pressures occurring within the bottom third of the abutment. Similar profiles have been obtained by physical measurements and numerical simulations (ABDEL-FATTAH; ABDEL-FATTAH, 2019; ABDEL-FATTAH; ABDEL-FATTAH; HEMADA, 2018; BANKS; BLOODWORTH, 2018; CARISTO; BARNES; MITOULIS, 2018; CIVJAN et al., 2013; KIM et al., 2014; LEHANE, 2011; MITOULIS et al., 2016; PAIK; SALGADO, 2003).

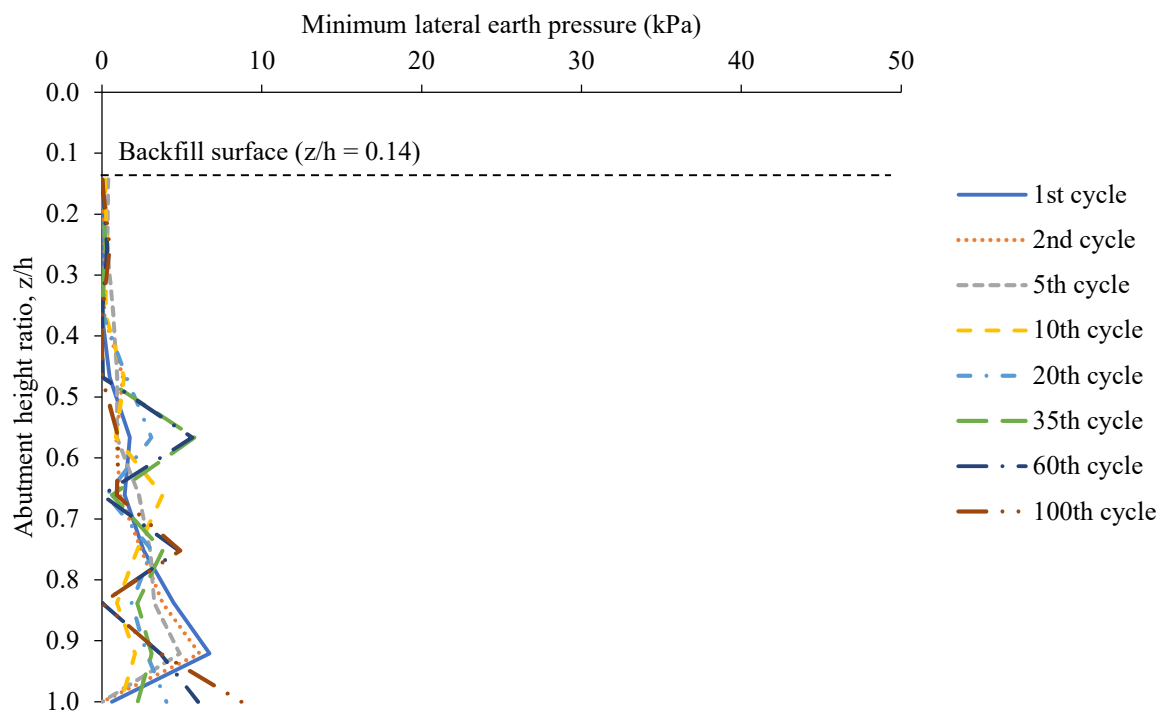
The lateral earth pressures presented a nonlinear distribution along the abutment height due to arching in soils, as discussed in subsection 5.2. The obtained lateral earth pressure profiles can be related to the lateral displacement amplitude imposed at the abutment, which was sufficient to overcome the shear strength of the backfill in both passive and active directions. During the passive direction, the abutment forced a soil portion to slip upward toward the backfill surface, inducing a concentration of lateral earth pressures at the middle third of the abutment, which can explain the obtained maximum lateral earth pressure profiles. During the active direction, a soil portion was slipped downward toward the gap developed between the abutment and the backfill. This slip displaced the soil toward the bottom third of the abutment, which can justify the obtained minimum lateral earth pressure profiles. The previously mentioned behavior can be observed from shadings of relative shear stress (τ_{rel}), as shown in Figure 5.16, arrows of resultant displacement (u_{res}), as shown in Figure 5.17, and shadings of deviatoric strain (γ_s), as shown in Figure 5.18. τ_{rel} and γ_s were defined as described in subsection 5.2.

Figure 5.14 – Distributions of maximum lateral earth pressures along the abutment height for selected annual cycles.



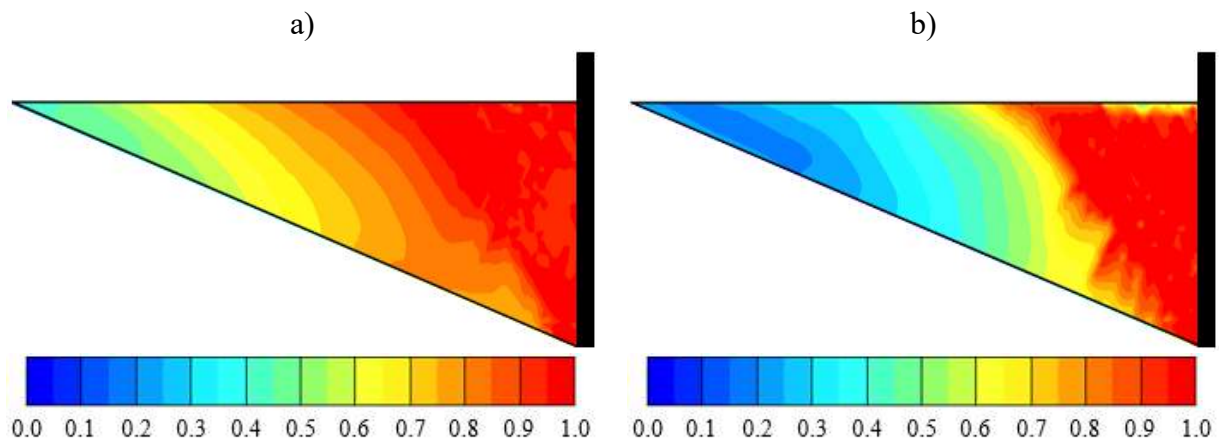
Source: Elaborated by the author (2020).

Figure 5.15 – Distributions of minimum lateral earth pressures along the abutment height for selected annual cycles.



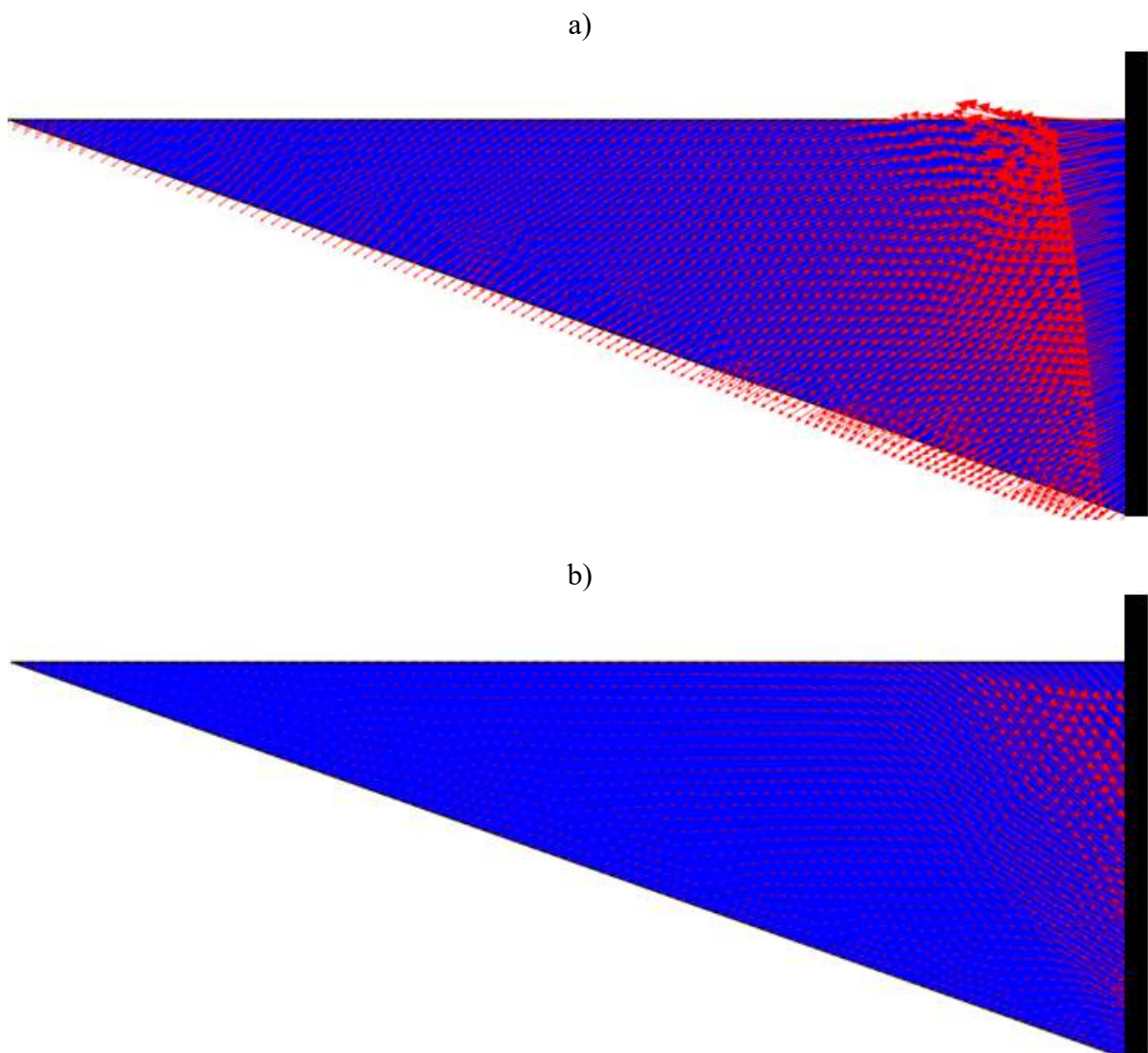
Source: Elaborated by the author (2020).

Figure 5.16 – Shadings of relative shear stress in the backfill for a typical annual cycle: a) passive direction; b) active direction.



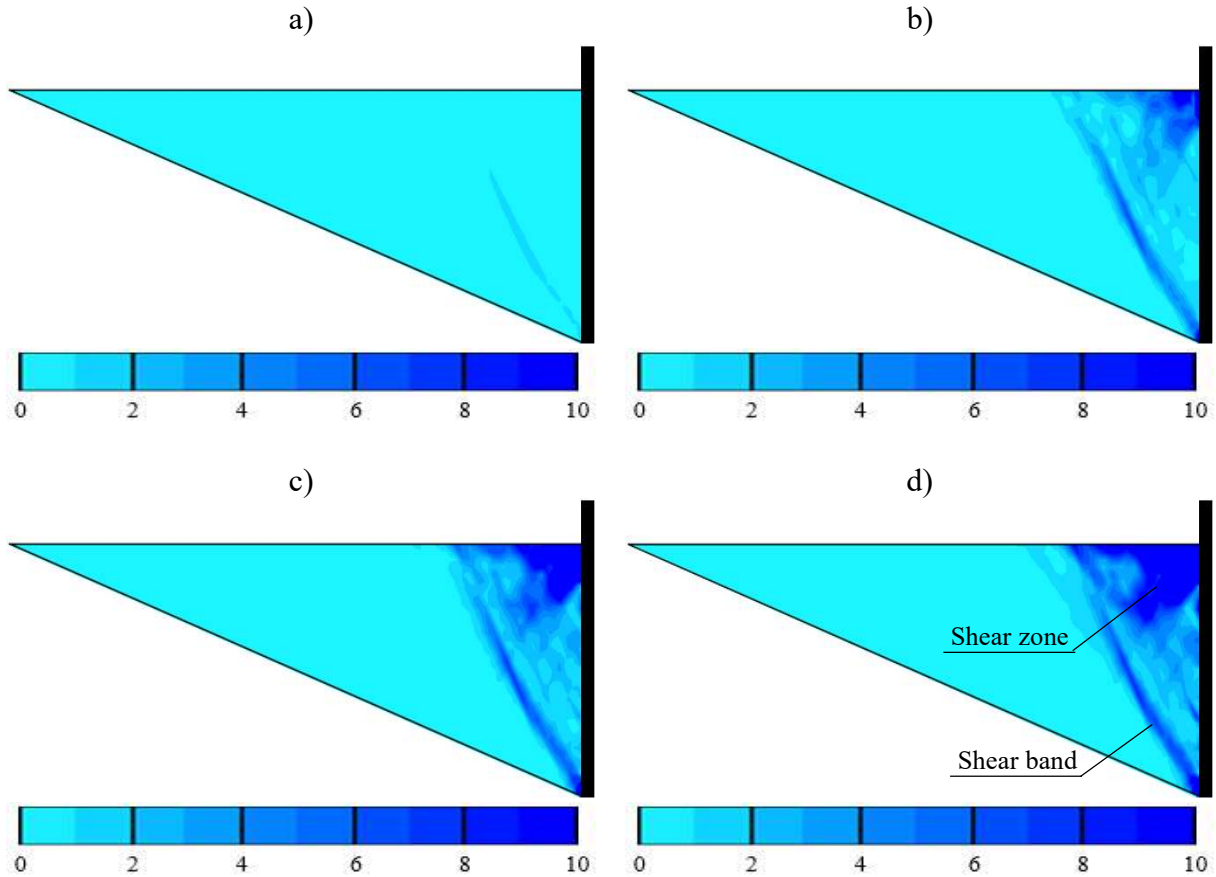
Source: Elaborated by the author (2020).

Figure 5.17 – Arrows of resultant displacement in the backfill for a typical annual cycle: a) passive direction; b) active direction.



Source: Elaborated by the author (2020).

Figure 5.18 – Shadings of accumulated deviatoric strain (in %) in the backfill at the end of selected annual cycles: a) 1st cycle; b) 33rd cycle; c) 66th cycle; d) 100th cycle.



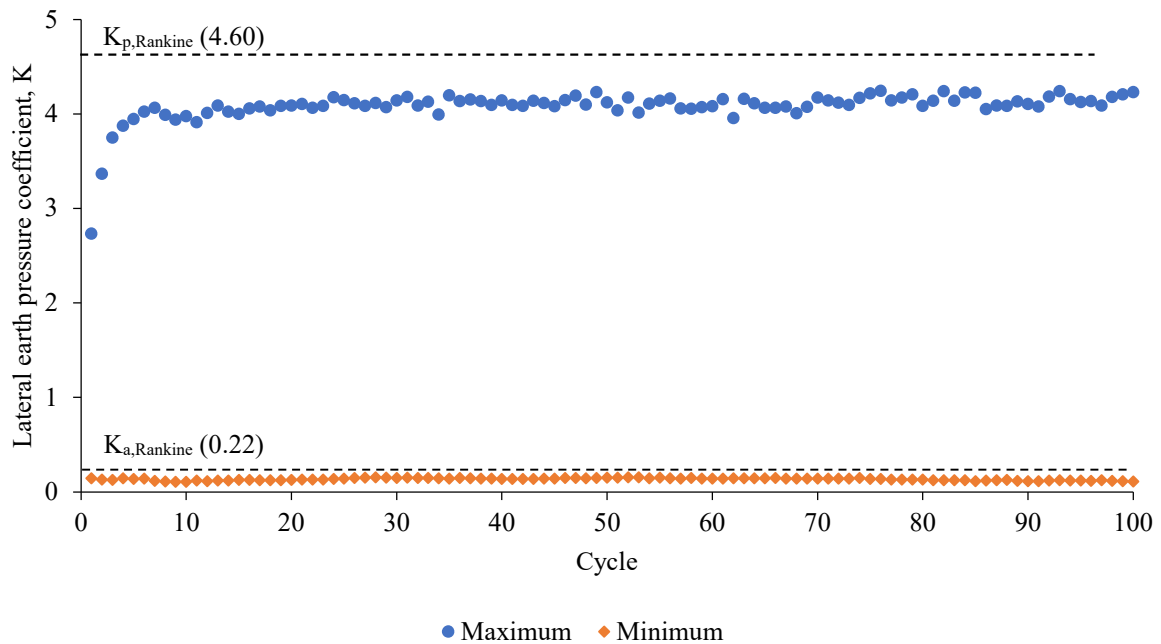
Source: Elaborated by the author (2020).

The shadings show potential zones of soil failure ($\tau_{rel} = 1$) near the abutment in both passive and active directions. The arrows demonstrate that, during the passive direction, the soil near the upper third of the abutment was displaced toward the backfill surface. During the active direction, the soil was displaced toward the bottom third of the abutment. The shadings also show that, with the cycles, a shear band was formed at a certain distance from the abutment, and a shear zone was formed near the upper third of the abutment, indicating sliding surfaces.

Figures 5.19 presents the evolution of the lateral earth pressure coefficient (K) with the annual cycles. The maximum lateral earth pressure coefficient (K_{max}) presented a nonlinear increase with a decreasing rate within the first cycles and then reached the steady state slightly below $K_{p,Rankine}$ in the fifth cycle. The K_{max} value at the steady state can be assumed as 4.1. On the other hand, the minimum lateral earth pressure coefficient (K_{min}) remained at the steady state close to $K_{a,Rankine}$ throughout the entire analyzed cycles. Moreover, K_{min} was less affected by the annual cycles of lateral displacements of the abutment than K_{max} , probably due to the magnitude of soil lateral displacement required to reach the passive and active failure states, as

discussed in subsection 5.2. Results of field monitoring, laboratory experiments, and numerical simulations have shown a similar behavior (AL-QARAWI; LEO; LIYANAPATHIRANA, 2020; BANKS; BLOODWORTH, 2018; CARISTO; BARNES; MITOULIS, 2018; FROSCH; LOVELL, 2011; GABRIELI; ZORZI; WAN, 2015; KIM; LAMAN, 2012; LEHANE, 2011; RAVJEE et al., 2018; TATSUOKA et al., 2009; ZADEHMOHAMAD; BAZAZ, 2019).

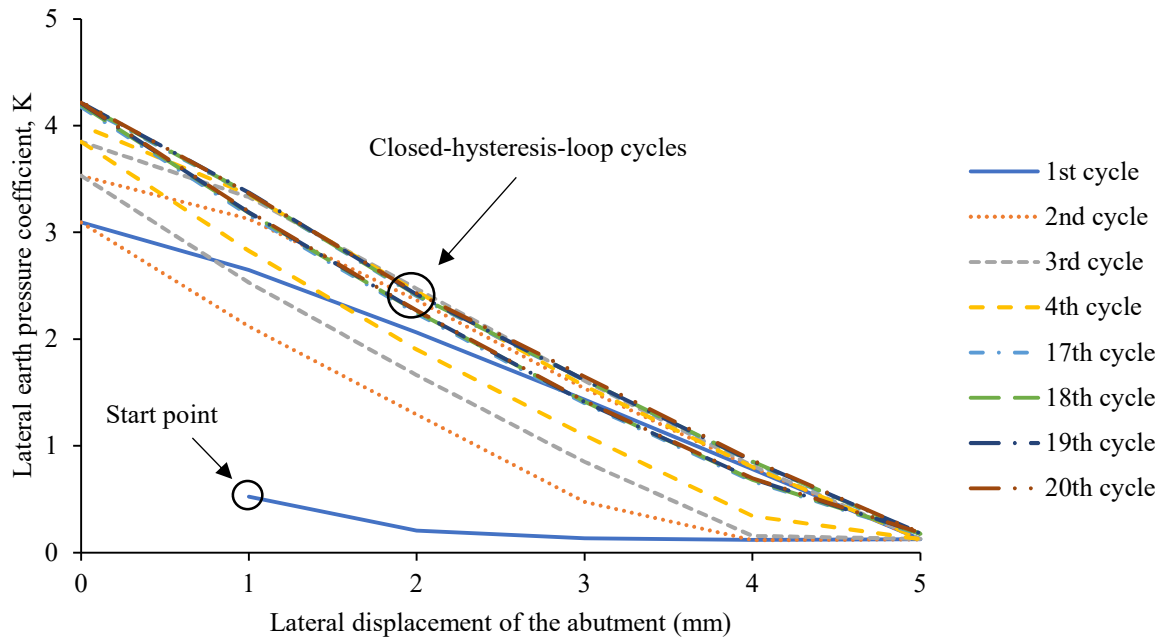
Figure 5.19 – Lateral earth pressure coefficients for annual cycles.



Source: Elaborated by the author (2020).

The behavior observed for the variation of K_{\max} with the cyclic lateral displacements of the abutment (Figure 5.19) depends on the effects of soil densification and granular flow promoted by cycling. As discussed in subsection 2.3, densification and granular flow have opposite effects on the backfill. While densification increases the stiffness of the soil, granular flow contributes to reducing it. The influence of the effect of soil densification appeared to be preponderant on the initial cycles, which led to increased maximum lateral pressure coefficients. However, a balance between both effects appeared to have been reached in the following cycles, resulting in constant maximum lateral earth pressure coefficients. At this moment, the soil reached the shakedown state. Figure 5.20 shows the lateral earth pressure coefficient as a function of the lateral displacement of the abutment for selected annual cycles. It is possible to observe that the cyclic lateral displacements resulted in closed hysteresis loops after some cycles, which indicates that the elastic shakedown has been reached with increasing cycles.

Figure 5.20 – Lateral earth pressure coefficients during the cyclic process for selected annual cycles.

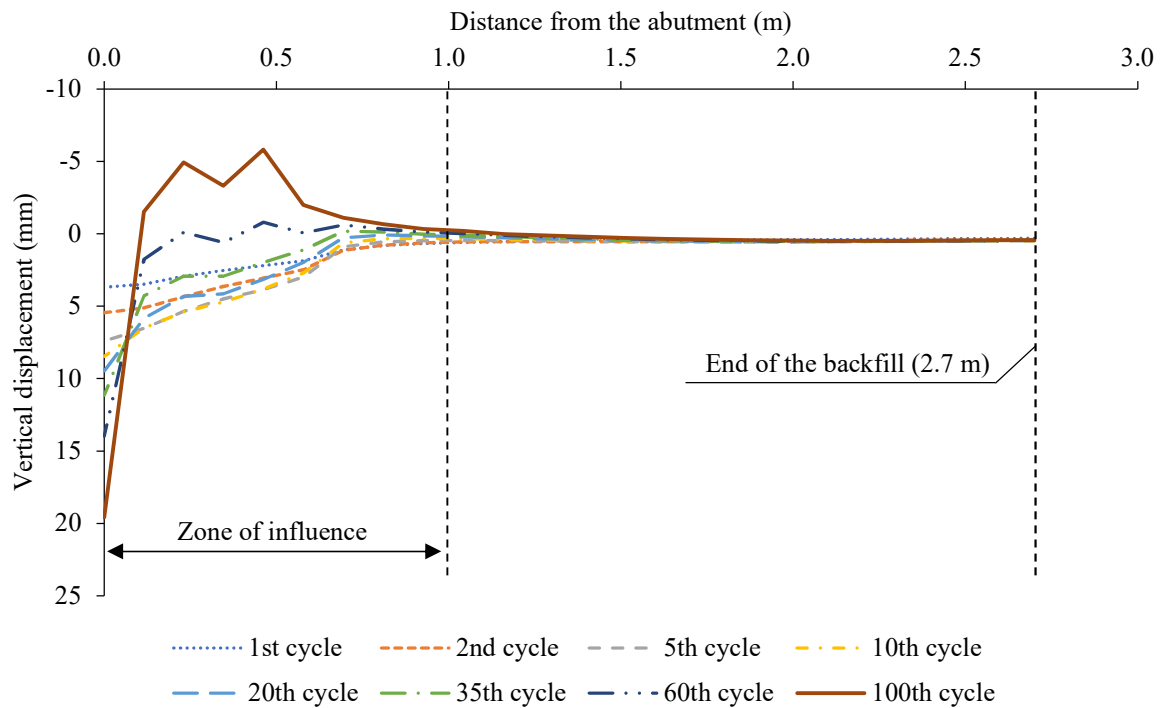


Source: Elaborated by the author (2020).

Profiles of vertical displacement of the backfill surface for selected annual cycles were also presented in Figure 5.21. Displacements were obtained at the end of each cycle. Positive values were assigned for the settlements in the figure. The largest settlement occurred near the backfill-abutment interface and decreased with the distance from the abutment. As the cycles increased, a heave zone was formed at a certain distance from the abutment, which suggests the presence of the soil granular flow defined by England, Tsang and Bush (2000). The peak heave was approximately 25% of the peak settlement. The influence zone of the displacements can be assumed to cover a distance equal to abutment height measured from the abutment. Within this zone, settlements and heave increased with the cycles, which indicates the presence of ratcheting.

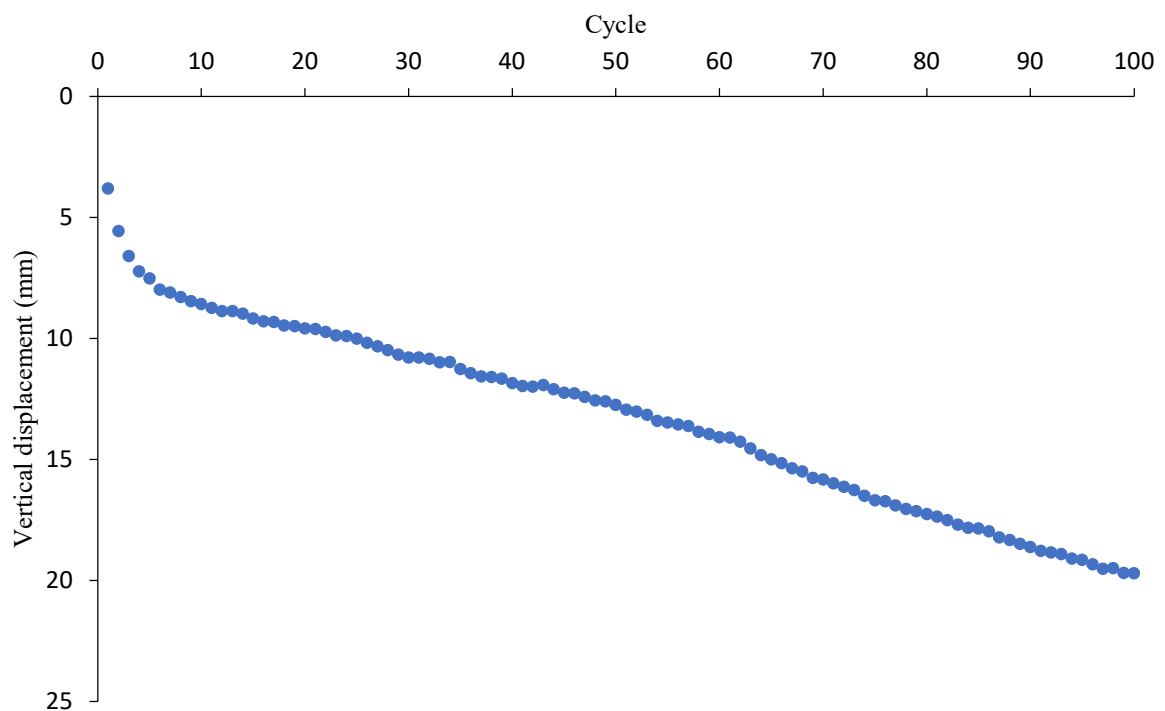
Figure 5.22 shows the evolution of the vertical displacements at the top of the backfill-abutment interface. It is noted a sharp increase in the settlement in the first five cycles, followed by a nearly linear increase in the next cycles. A tendency of reaching the steady state was not observed. The results agree with the experimental and numerical findings reported in the technical literature (AL-QARAWI; LEO; LIYANAPATHIRANA, 2020; ARGYROUDIS et al., 2016; CARISTO; BARNES; MITOULIS, 2018; DAVID; FORTH; YE, 2014; ENGLAND; TSANG; BUSH, 2000; MITOULIS et al., 2016; MUNOZ et al., 2012; TATSUOKA et al., 2009; ZADEHMOHAMAD; BAZAZ, 2019).

Figure 5.21 – Vertical displacement profiles of the backfill surface along the distance from the abutment for selected annual cycles.



Source: Elaborated by the author (2020).

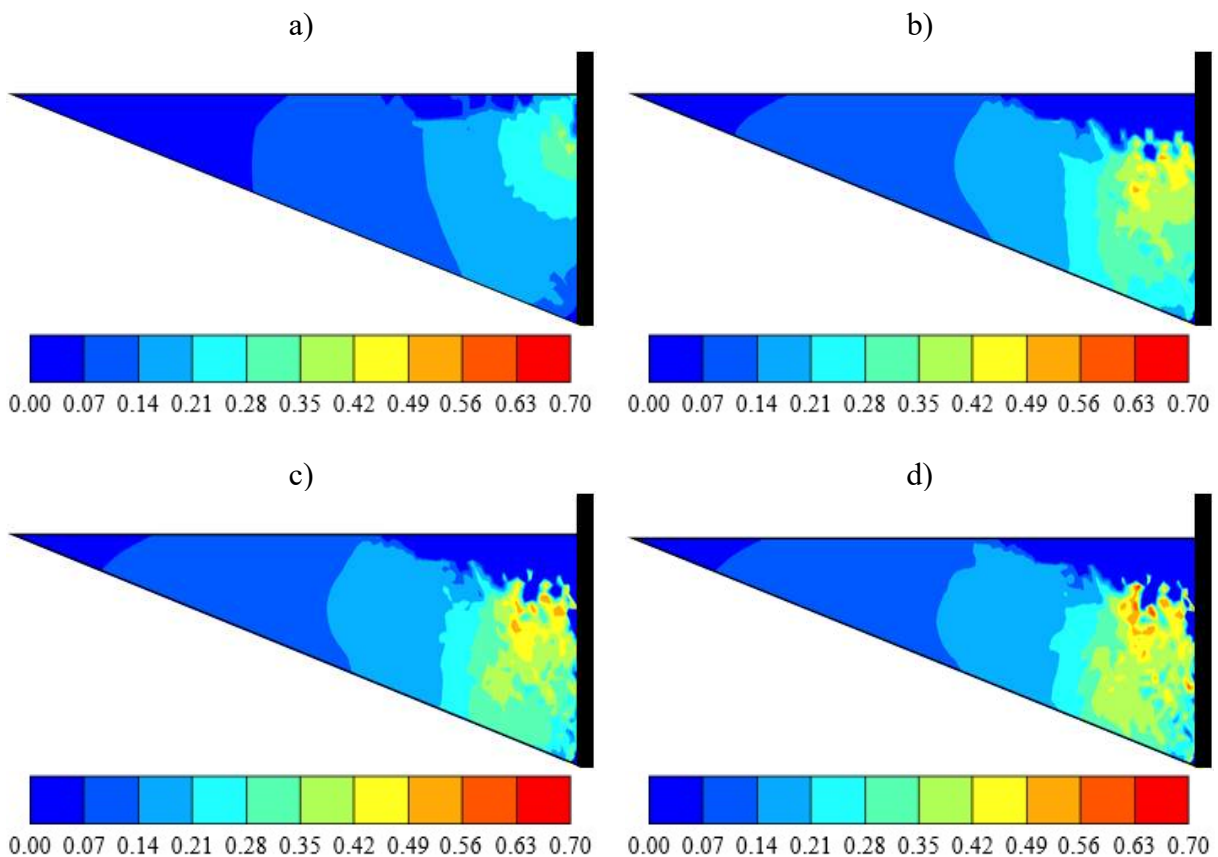
Figure 5.22 – Vertical displacements at the top of the backfill-abutment interface for annual cycles.



Source: Elaborated by the author (2020).

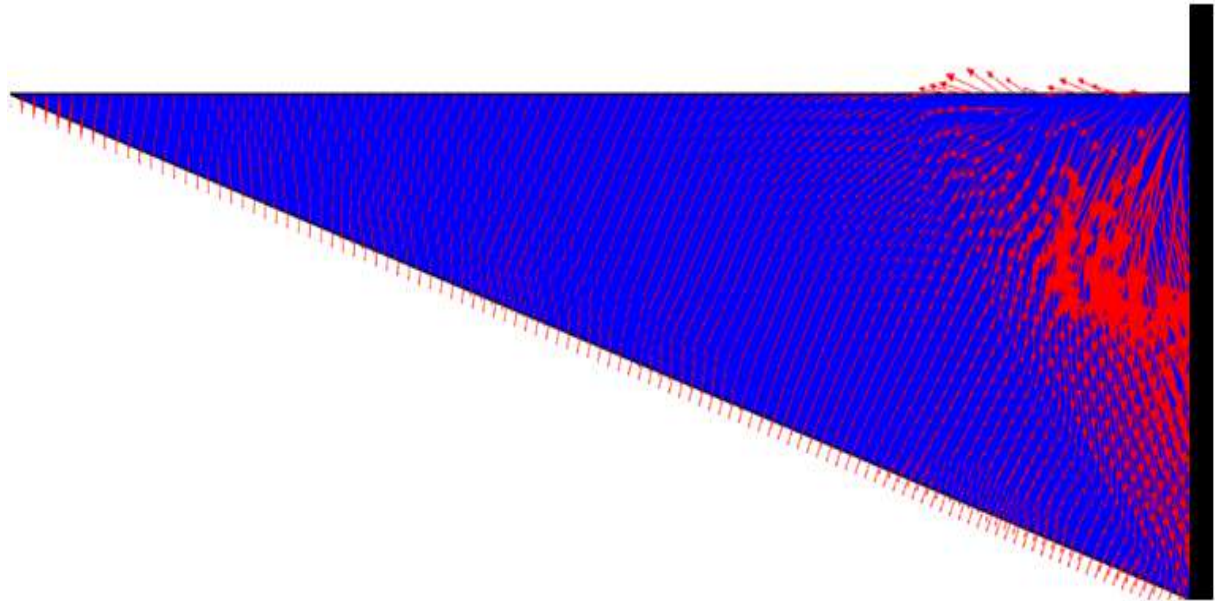
Vertical displacements on the backfill surface are associated with the effects of soil densification and granular flow. While densification reduces the settlement increment, granular flow plays an opposite effect. The influence of the effect of densification appeared to be more significant for the first five cycles, while a balance between both effects appeared to have been reached in the subsequent cycles. The densification of the backfill is shown in Figure 5.23, which presents shadings of accumulated compressive volumetric strain in the backfill at the end of selected annual cycles, while the vectors of accumulated resultant displacement shown in Figure 5.24 suggest the occurrence of the granular flow defined by England, Tsang and Bush (2000). The shadings show that larger compressive volumetric strains occurred near the backfill-abutment interface and decreased with distance from the abutment, which agrees with the profiles of Figure 5.18. Moreover, the increase in the compressive volumetric strains with the cycles shows the occurrence of ratcheting in the soil and explains the continuous increase in the vertical displacement of the backfill surface (Figure 5.19). The arrows show that a soil portion is displaced toward the backfill surface, which indicates the occurrence of the soil granular flow defined by England, Tsang and Bush (2000).

Figure 5.23 – Shadings of accumulated compressive volumetric strain (in %) in the backfill at the end of selected annual cycles: a) 1st cycle; b) 33rd cycle; c) 66th cycle; d) 100th cycle.



Source: Elaborated by the author (2020).

Figure 5.24 – Arrows of accumulated resultant displacement in the backfill after the annual cyclic lateral loading.



Source: Elaborated by the author (2020).

6 PARAMETRIC ANALYSIS

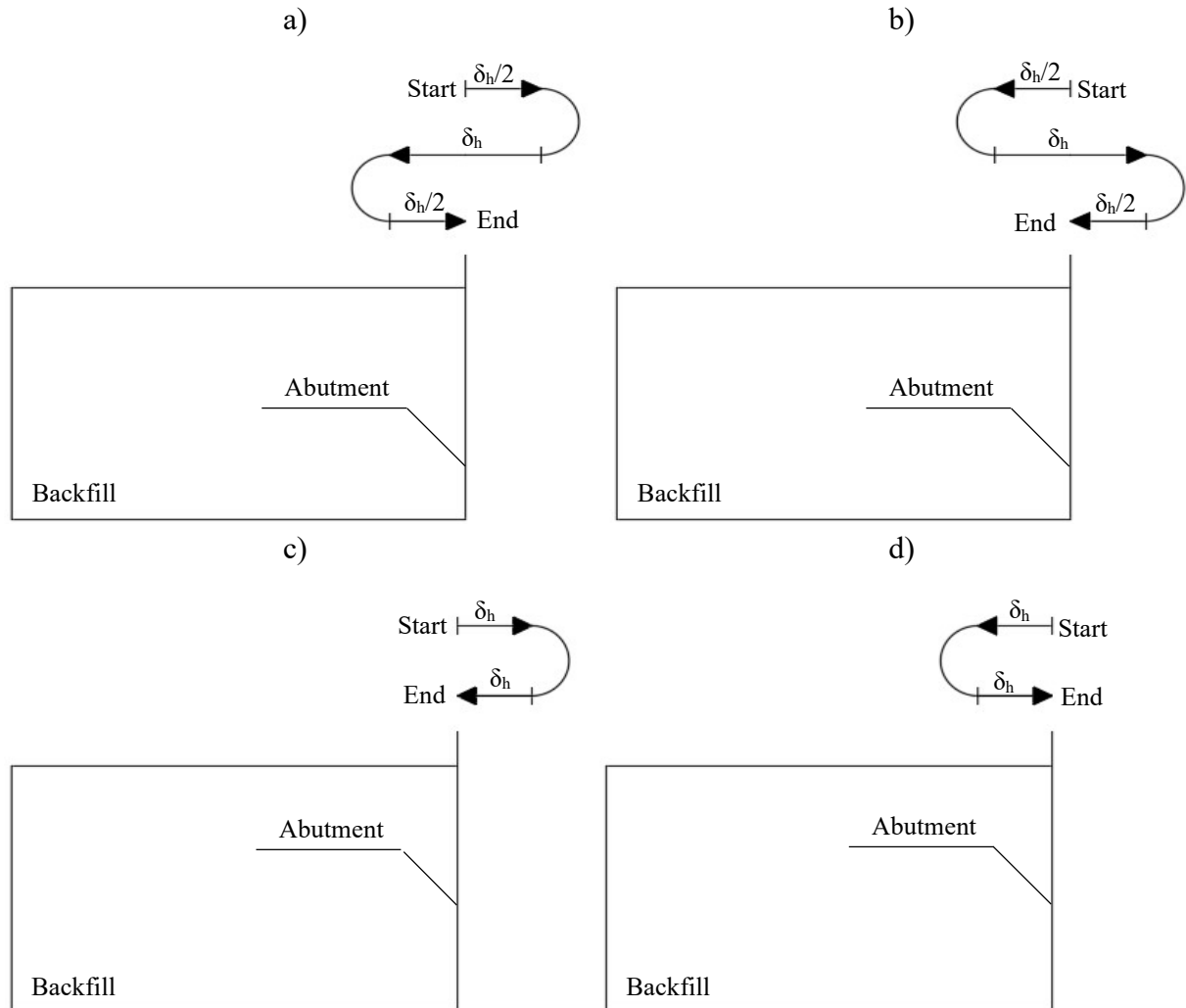
A parametric analysis with parameters of interest was performed after predicting the response of the backfill-abutment system upon daily and annual cyclic lateral displacements. Numerical simulations were carried out by considering 50 cycles of lateral displacements of the abutment. This number of cycles was chosen based on the results of physical measurements and numerical simulations presented in the technical literature (AL-QARAWI; LEO; LIYANAPATHIRANA, 2020; BANKS; BLOODWORTH, 2018; CARISTO; BARNES; MITOULIS, 2018; ENGLAND; TSANG; BUSH, 2000; KIM; LAMAN, 2012; RAVJEE et al., 2018; TATSUOKA et al., 2009). Results presented in subsection 5.3 corroborate the findings reported in the technical literature. It has been found that stabilization (steady state) of the lateral earth pressures on the abutment, and the variation rate of the vertical displacement of the backfill surface is usually reached within 50 cycles. Limiting the number of cycles can save time and unnecessary computational efforts. The previous analyses revealed that maximum lateral earth pressures are more affected by cyclic lateral displacements of the abutment than minimum lateral earth pressures. For this reason, the parametric analysis presented in this section included results of maximum lateral earth pressures only.

6.1 Bridge completion season

The first parameter of investigation was the influence of the completion season of bridge construction. Simulations were performed for an amplitude of prescribed horizontal displacements (δ_h) equal to 5 mm, which represents the cyclic lateral displacements of the abutment due to annual maximum longitudinal expansions and contractions of the bridge. Four scenarios represented the lateral displacements of the abutment for bridge construction completed in spring, summer, autumn, and winter. When the bridge is completed in spring, the abutment initially displaces $\delta_h/2$ towards the backfill from spring to summer. Then, the abutment displaces δ_h away from the backfill from summer to winter. Finally, the abutment displaces $\delta_h/2$ towards the backfill from winter to spring, completing the annual cycle. When the bridge is finished in summer, the abutment firstly displaces δ_h away from the backfill from summer to winter. Then, the abutment displaces δ_h towards the backfill from winter to summer, completing the annual cycle. When the bridge is completed in autumn and winter, the abutment displaces in the opposite way as for the bridge finished in spring and summer, respectively.

Figure 6.1 schematically illustrates the lateral displacements of the abutment during an annual cycle for all analyzed scenarios.

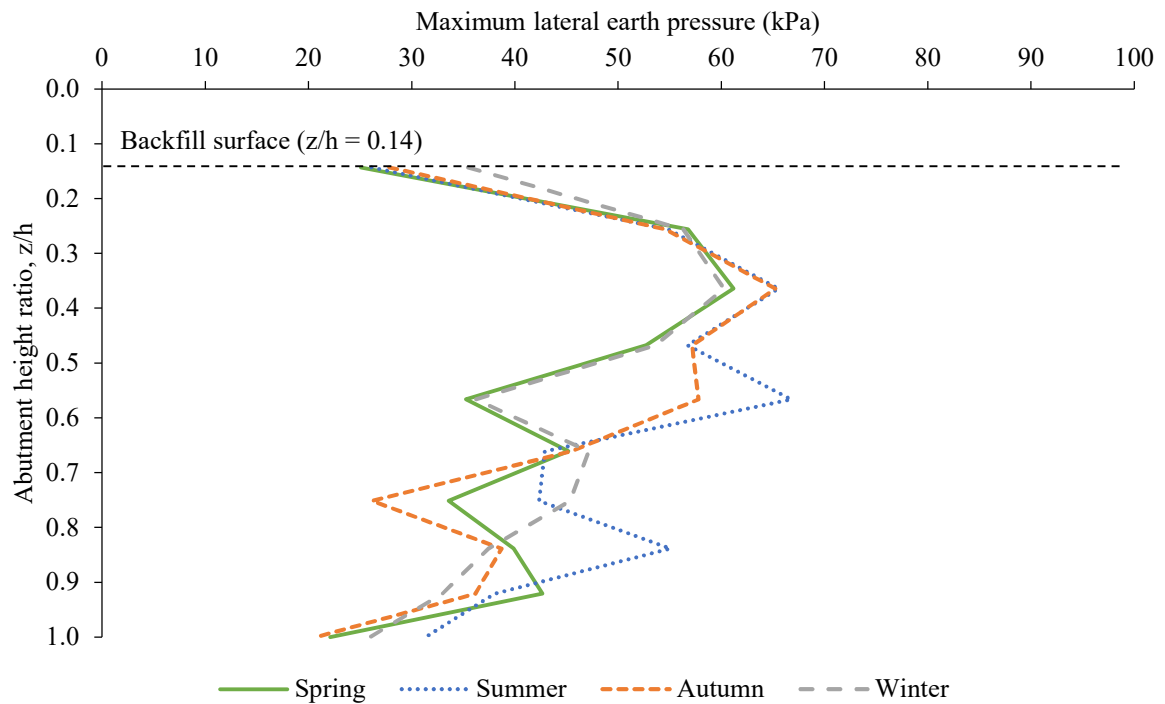
Figure 6.1 – Schemes of annual cycles of lateral displacements of the abutment for all analyzed scenarios: a) autumn; b) spring; c) summer; d) winter.



Source: Elaborated by the author (2020).

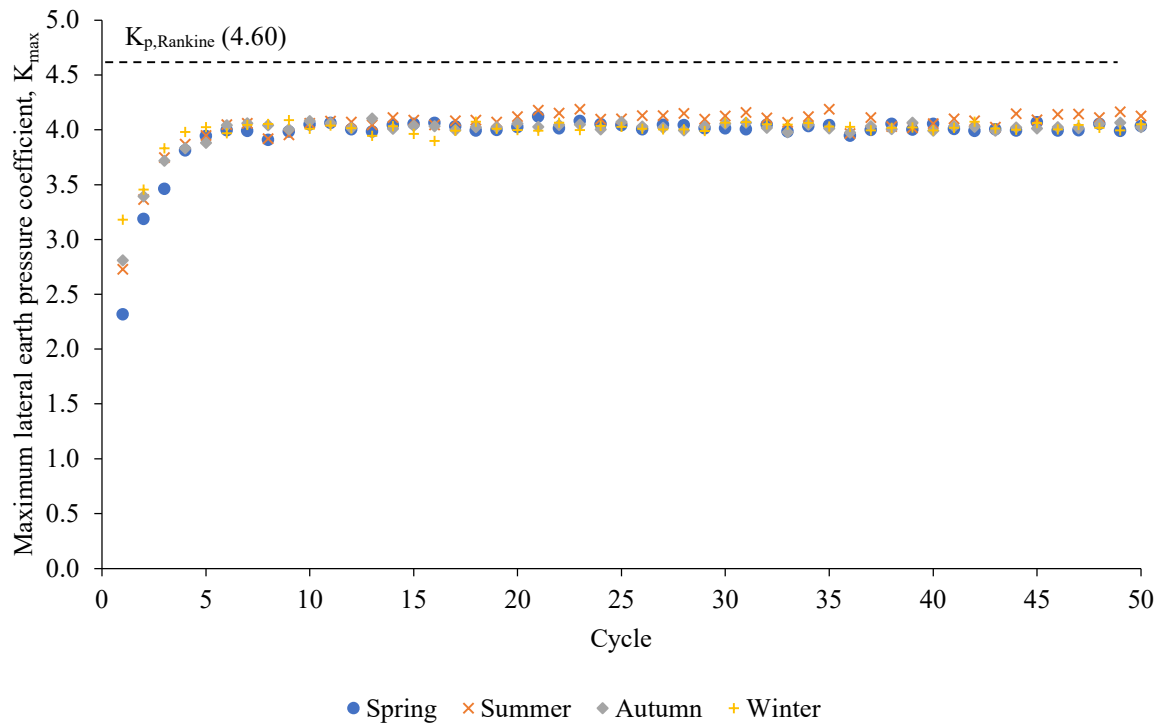
Figure 6.2 shows the maximum lateral earth pressures along the abutment for the four scenarios after 50 annual cycles of lateral displacements. In the four scenarios, the maximum lateral earth pressures presented a nonlinear distribution along the abutment height with the largest values of maximum lateral earth pressures occurring within the middle third of the abutment. The distributions of maximum lateral earth pressures can be approximated by a bi-linear shape with the largest pressures occurring within the middle third of the abutment. Figure 6.3 presents the evolution of K_{\max} with the annual cycles for the four seasons. For all analyzed scenarios, K_{\max} presented a nonlinear increase with a decreasing rate in the initial cycles and then reached the steady state slightly below $K_{p, \text{Rankine}}$ from the fifth cycle.

Figure 6.2 – Distributions of maximum lateral earth pressures along the abutment height for the analyzed scenarios after 50 annual cycles.



Source: Elaborated by the author (2020).

Figure 6.3 – Maximum lateral earth pressure coefficients for annual cycles considering the analyzed scenarios.

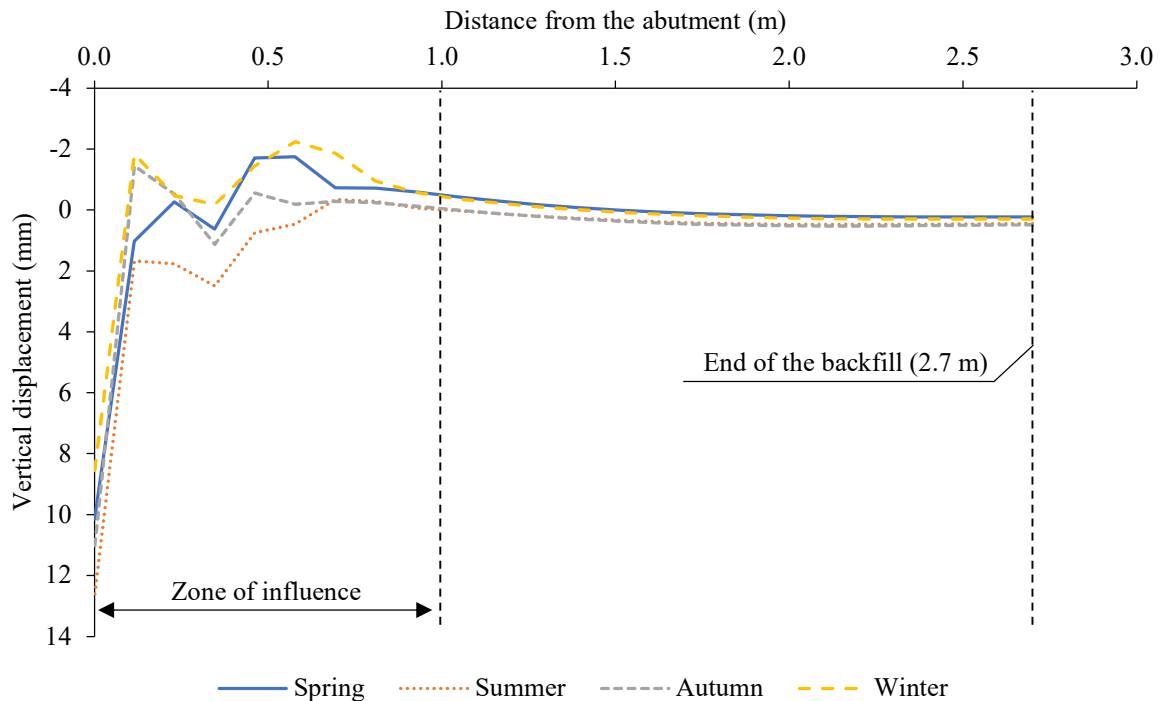


Source: Elaborated by the author (2020).

The maximum lateral earth pressure profiles (Figure 6.2) and the K_{\max} values (Figure 6.3) were not significantly affected by the completion season of bridge construction. Although the analyzed scenarios simulated different initial movements of the abutment, the fact that the amplitude of the displacements was the same in all scenarios can explain the observed characteristic. Similar results were observed in numerical simulations carried out by Caristo, Barnes and Mitoulis (2018), and England, Tsang and Bush (2000).

Vertical displacement profiles of the backfill surface along the distance from the abutment after 50 annual cycles were also assessed (Figure 6.4). Displacements correspond to the end of each cycle. Downward vertical displacements (settlement) were considered positive in the figure. For all seasons, the largest settlement took place near the backfill-abutment interface. Settlements decreased with increasing distance from the abutment. A heave zone was formed at a certain distance from the abutment for a bridge completed in spring, autumn, and winter while no heave was observed for a bridge finished in summer. Vertical displacements took place within an influence zone equal to the abutment height measured from the abutment.

Figure 6.4 – Vertical displacement profiles of the backfill surface along the distance from the abutment for the analyzed scenarios after 50 annual cycles.

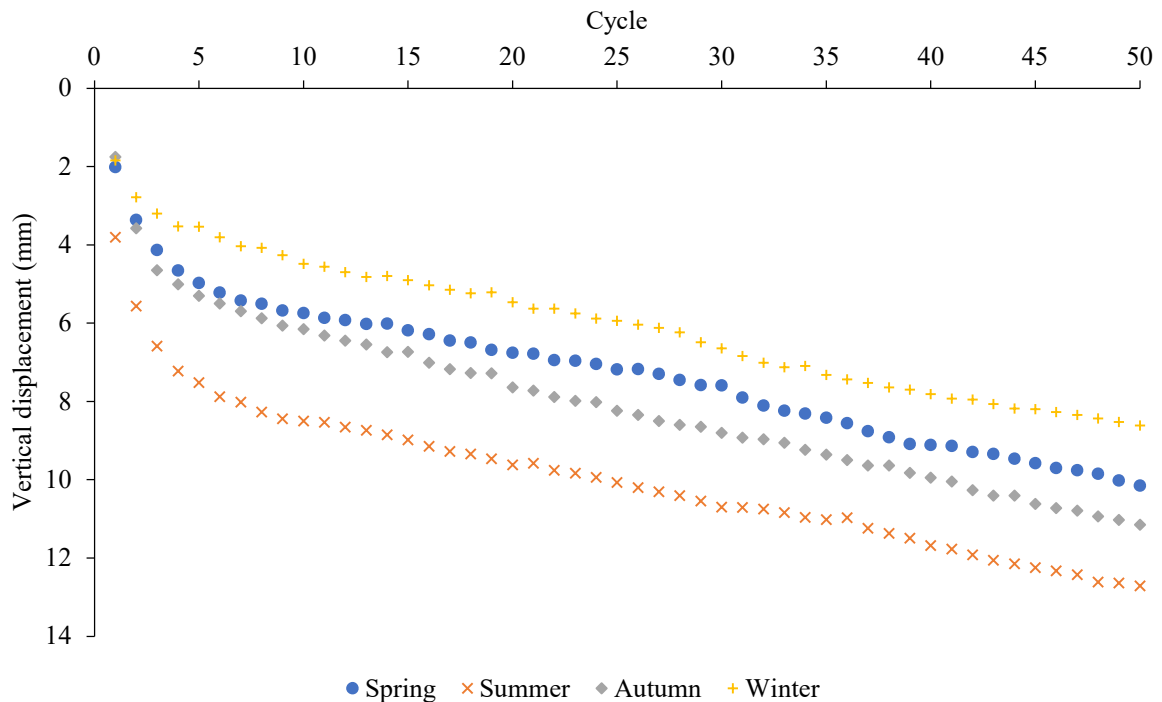


Source: Elaborated by the author (2020).

Figure 6.5 shows the vertical displacements at the top of the backfill-abutment interface for varying annual cycles. For all analyzed season scenarios, settlements increased

nonlinearly with a decreasing rate in the first cycles and then increased linearly. No tendency of reaching the steady state could be observed with increasing cycles. The largest settlements occurred for a bridge finished in summer, while the smallest settlements took place for a bridge finished in winter. Intermediate settlements were obtained for spring and autumn seasons, with slightly higher values for the former.

Figure 6.5 – Vertical displacements on the top of the backfill-abutment interface for annual cycles considering the analyzed scenarios.



Source: Elaborated by the author (2020).

As observed in Figures 6.4 and 6.5, the vertical displacements on the backfill surface were influenced by the completion season of the bridge construction. The differences in the displacements between seasons can be associated with the initial movement of the abutment (Figure 6.1). When a bridge is completed in summer, the abutment firstly displaces away from the backfill, and, consequently, the soil initially tends to flow downwards towards the gap developed between the abutment and the backfill, resulting in larger settlements. On the other hand, a bridge finished in winter will have the abutment firstly displacing to the backfill. Therefore, the soil initially tends to flow upwards towards the backfill surface, resulting in smaller settlements. Settlements with intermediate amplitudes in spring and autumn are explained by the fact that the initial lateral abutment displacement in both seasons is half that at the beginning of summer and winter. The absence of heave for the bridge construction

completed in summer may be explained by an insufficient number of cycles. In this case, more than 50 cycles are needed to develop a heave on the backfill surface, as observed in subsection 5.3 after 60 annual cycles.

Numerical simulations carried out by England, Tsang and Bush (2000) showed that the completion season of the bridge construction influenced the vertical displacements on the backfill surface. The authors reported that the largest settlements occurred for a bridge completed in winter. On the other hand, numerical simulations performed by Caristo, Barnes and Mitoulis (2018) demonstrated that the vertical displacements on the backfill surface were not influenced by the completion season of the bridge construction. The differences between the results obtained by England, Tsang and Bush (2000), Caristo, Barnes and Mitoulis (2018), and the present investigation can be attributed to differences in the proposed models. England, Tsang and Bush (2000) modeled a part of an integral abutment considering only rotation movements of the abutment. Caristo, Barnes and Mitoulis (2018) completely simulated an integral abutment considering combined movements of rotation and translation of the abutment. The present investigation fully modeled a semi-integral abutment considering combined movements of rotation and translation of the abutment. Furthermore, the effects of the superstructure on the abutment and the approach slab/road on the backfill were not considered by those authors, unlike this investigation.

Finally, although the completion season of the bridge construction has not influenced the maximum lateral earth pressures on the abutment, the results showed that completing the construction of the bridge in summer represents the most unfavorable situation because of excessive settlements. For this reason, the following investigations were simulated for the summer scenario since it represented the most unfavorable situation. Another argument for simulating the summer scenario is that it represents the start condition of movement of the bridge abutment in the field.

6.2 Sheet pile stiffness

The influence of the foundation stiffness on the backfill-abutment system performance was investigated by varying the sheet pile profile. Three profiles were selected for this analysis: PZC-12, PZC-18, and PZC-28 (GERDAU, 2019). Table 6.1 shows the structural parameters of the selected profiles.

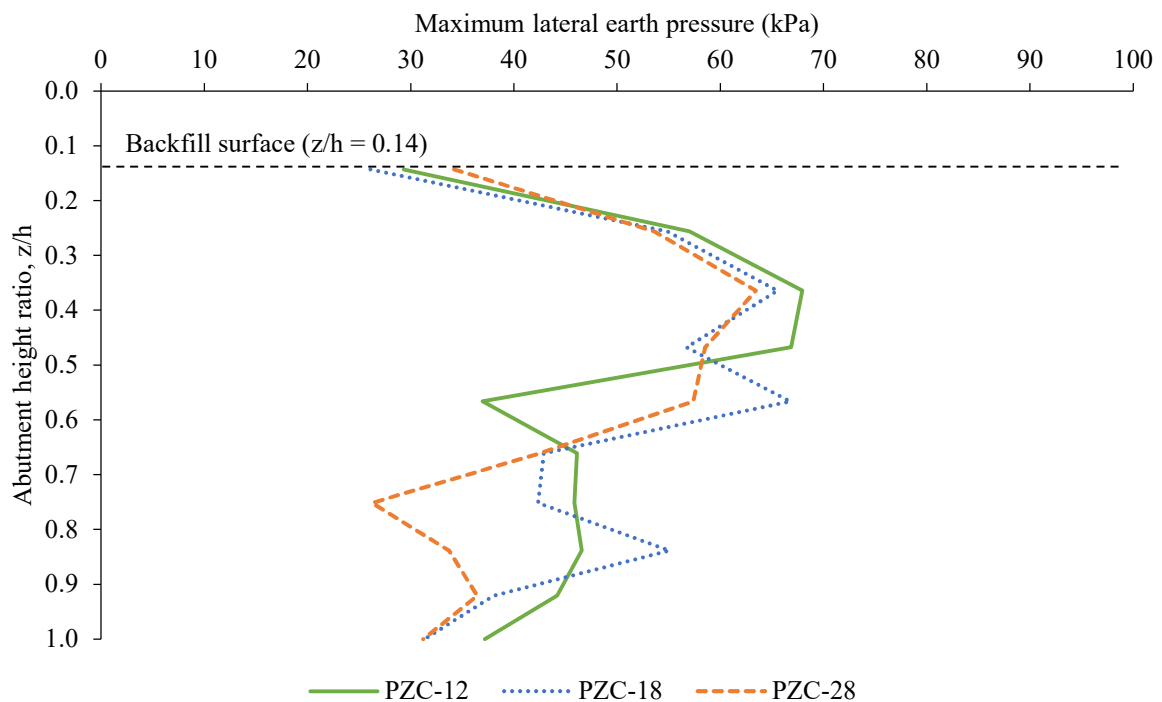
Table 6.1 – Structural parameters of the sheet pile profiles.

Parameter	Unit	PZC-12	PZC-18	PZC-28
Normal stiffness (EA)	kN/m	2.61×10^6	3.16×10^6	4.44×10^6
Flexural rigidity (EI)	kNm ² /m	4.01×10^4	7.33×10^4	1.30×10^5
Weight (w)	kN/m/m	0.98	1.18	1.66

Source: Elaborated by the author (2020).

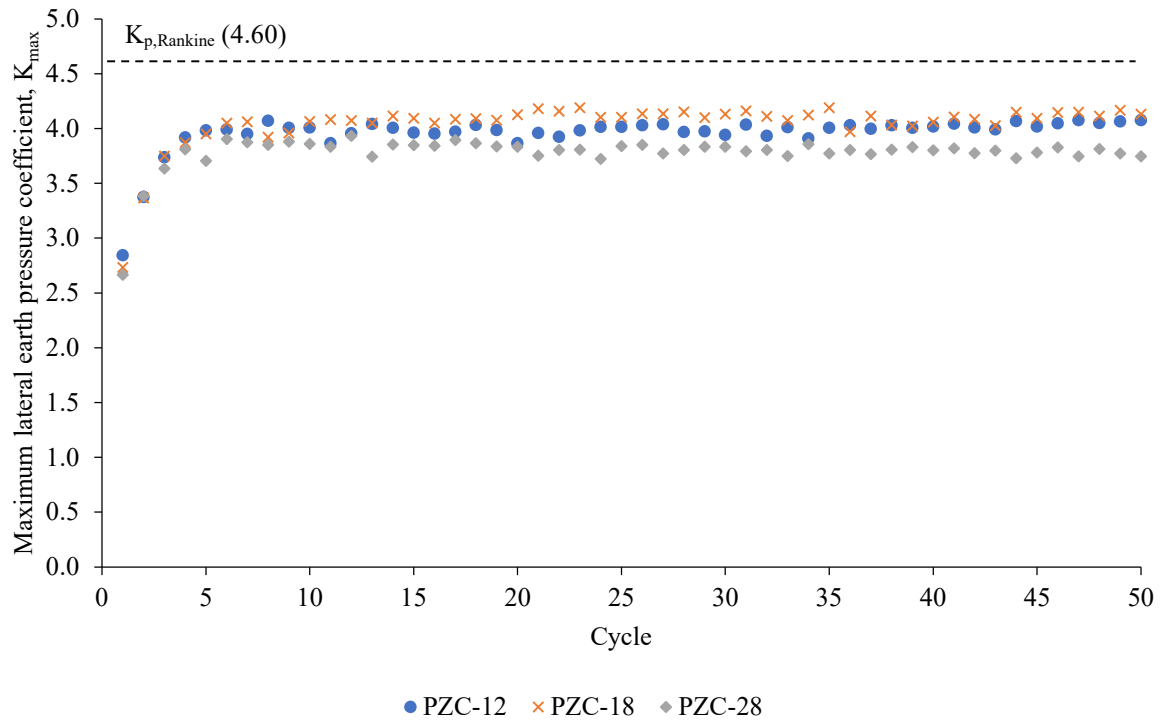
Figure 6.6 shows the maximum lateral earth pressures along the abutment height for the three profiles after 50 annual cycles of lateral displacements. For all profiles, the maximum lateral earth pressures presented a nonlinear distribution along the abutment height. The largest values of maximum lateral earth pressures occurred within the middle third of the abutment. The distributions of maximum lateral earth pressures can be approximated by a bi-linear shape with the largest pressures occurring within the middle third of the abutment. Figure 6.7 shows the maximum lateral earth pressure coefficient (K_{\max}) values calculated for annual cycles. Similar trends were obtained for all investigated profiles. K_{\max} presented a nonlinear increase with a decreasing rate in the first cycles and then reached the steady state slightly below $K_{p, \text{Rankine}}$.

Figure 6.6 – Distributions of maximum lateral earth pressures along the abutment height after 50 annual cycles considering the selected values of foundation stiffness.



Source: Elaborated by the author (2020).

Figure 6.7 – Maximum lateral earth pressure coefficients for annual cycles considering the selected values of foundation stiffness.

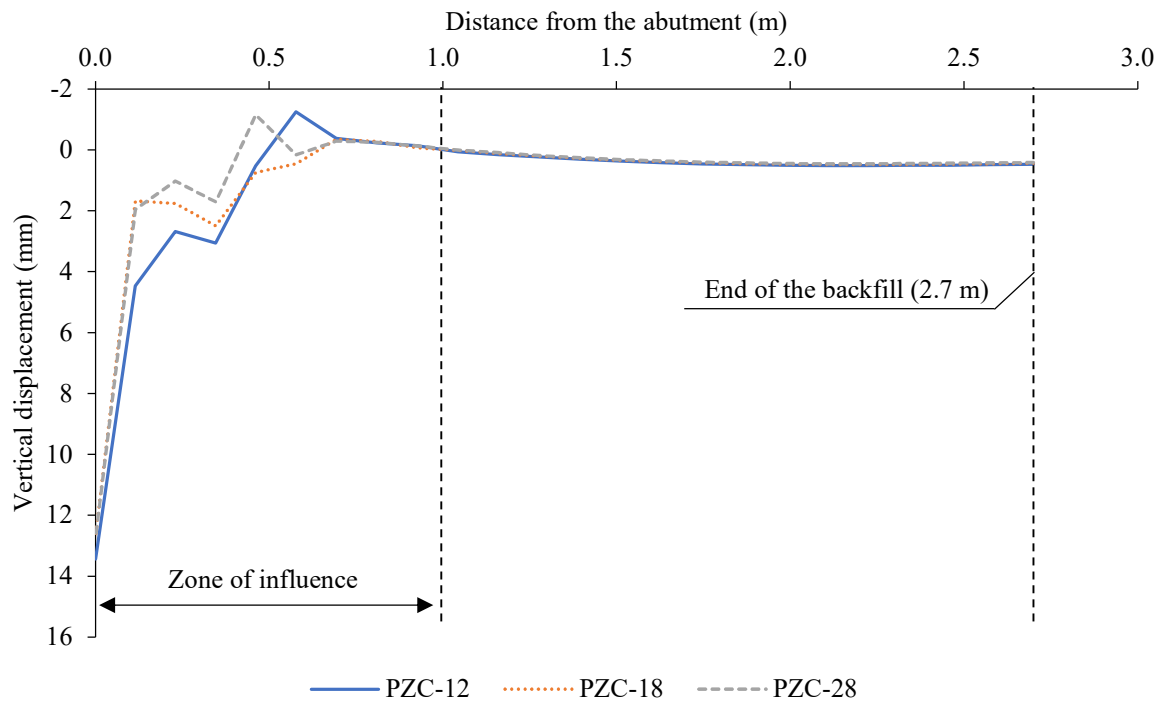


Source: Elaborated by the author (2020).

Vertical displacement profiles of the backfill surface along the distance from the abutment for the three profiles after 50 annual cycles are shown in Figure 6.8. The displacements were obtained at the end of each cycle. Settlements are considered positive in the figure. For all profiles, the largest settlement occurred near the backfill-abutment interface and decreased with increasing distance from the abutment. A heave zone was formed at a certain distance from the abutment. The influence zone of displacements can be assumed to occur within a distance equal to the abutment height measured from the abutment. Figure 6.9 shows the vertical displacements at the top of the backfill-abutment interface for annual cycles. For all investigated profiles, settlements presented a nonlinear increase with a decreasing rate in the initial cycles and then increased according to a nearly linear trend. A tendency of reaching the steady state could not be observed with increasing cycles.

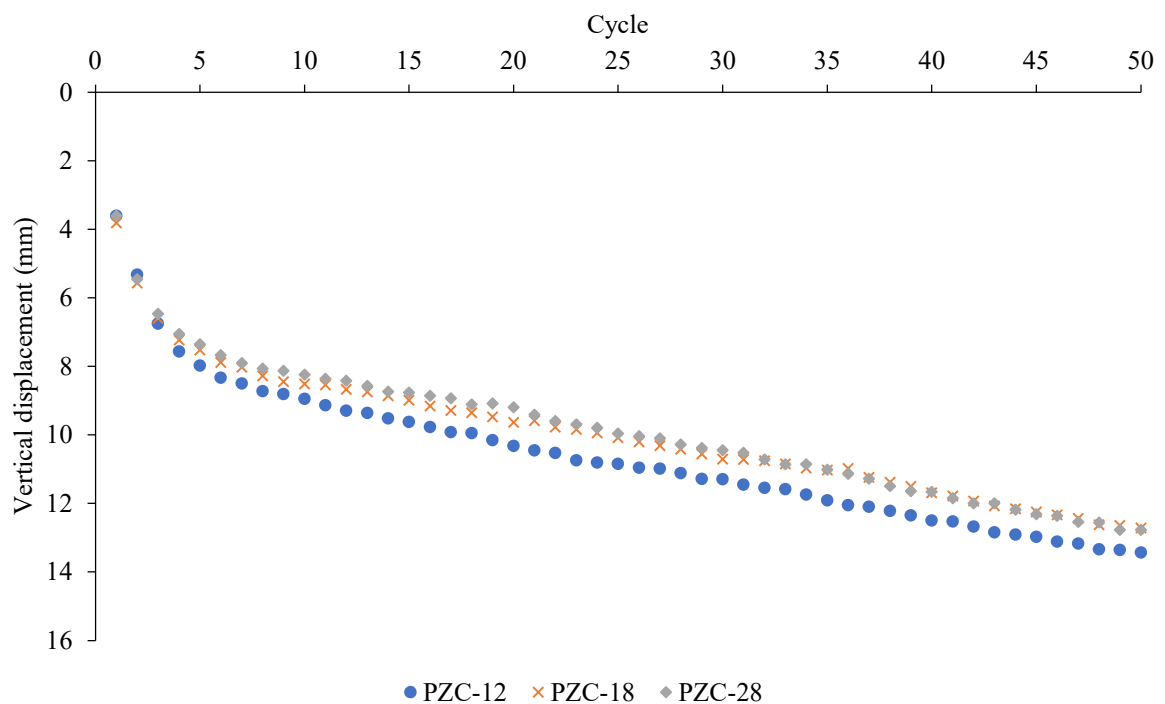
As observed in Figures 6.6, 6.7, 6.8, and 6.9, the response of the backfill-abutment system upon imposed cyclic lateral displacements at the abutment was not significantly influenced by the variation of the stiffness of the sheet piles used in the foundation of the SIAB. This can be associated with the fact that the abutment is not integrated to the foundation system.

Figure 6.8 – Vertical displacement profiles of the backfill surface along the distance from the abutment for the different values of foundation stiffness after 50 annual cycles.



Source: Elaborated by the author (2020).

Figure 6.9 – Vertical displacements on the top of the backfill-abutment interface for annual cycles considering the different values of foundation stiffness.



Source: Elaborated by the author (2020).

6.3 Lateral displacement amplitude

The last parameter of investigation was the influence of the lateral displacement amplitude of the abutment. Table 6.2 presents a compilation of lateral displacements of the abutment measured or assumed in various numerical and experimental investigations. It is observed that the values of δ_h/h situate within the range between 0.1% and 0.5%. Five different values of relative lateral displacement (δ_h/h) were chosen based on information from the sources cited in Table 6.2: 0.1%, 0.2%, 0.3%, 0.4% and 0.5%.

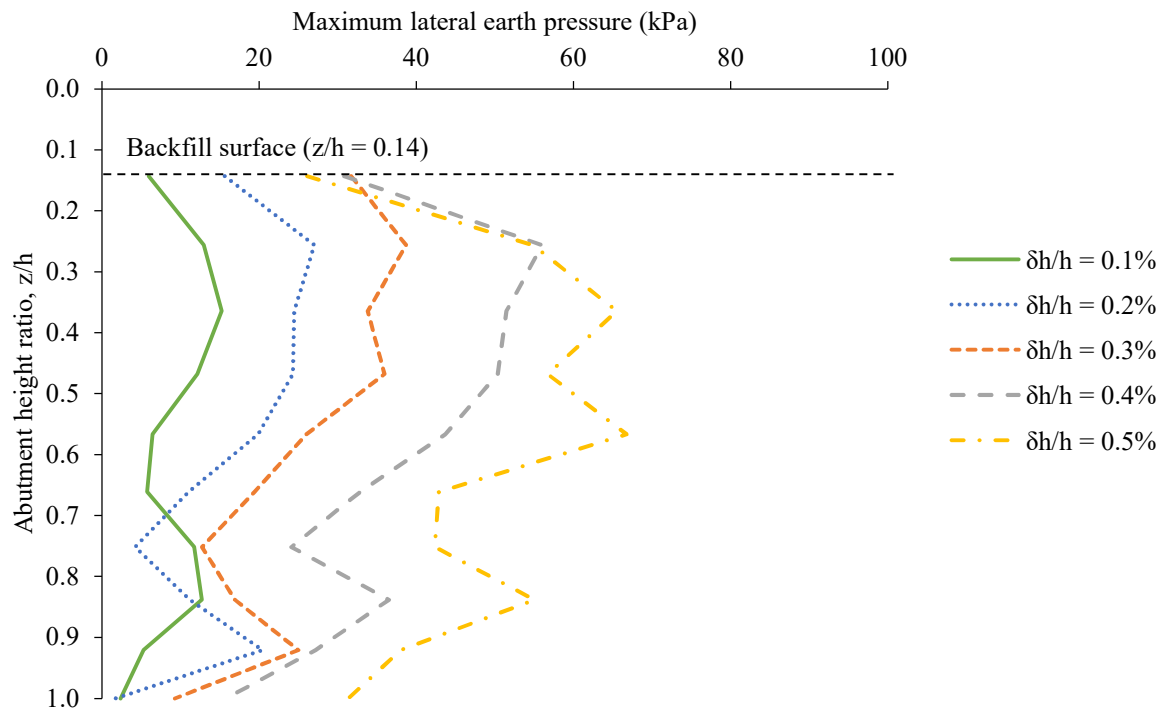
Table 6.2 – Lateral displacement of the abutment from several sources in the technical literature.

Reference	Amplitude (mm)	Abutment height (m)	δ_h/h (%)
Ng, Springman and Norrish (1998)	6	6.4	0.1
	12		0.2
Bloodworth et al. (2012)	16	4	0.4
Civjan et al. (2013)	12	4	0.3
	20		0.5
Huntley and Valsangkar (2013)	15	4	0.4
Mitoulis et al. (2016)	30	7	0.4
Caristo, Barnes and Mitoulis (2018)	27	7	0.4

Source: Elaborated by the author (2020).

Figure 6.10 shows maximum lateral earth pressures along the abutment height for the selected amplitudes after 50 cycles. For all selected values of δ_h/h , the maximum lateral earth pressures presented a nonlinear distribution along the abutment height. The lowest amplitude presented the largest values of maximum lateral earth pressure situating within the upper and bottom thirds of the abutment. Intermediate amplitudes concentrated the largest values of maximum lateral earth pressure in the upper third of the abutment. The highest amplitude presented the largest values of maximum lateral earth pressure occurring within the middle third of the abutment.

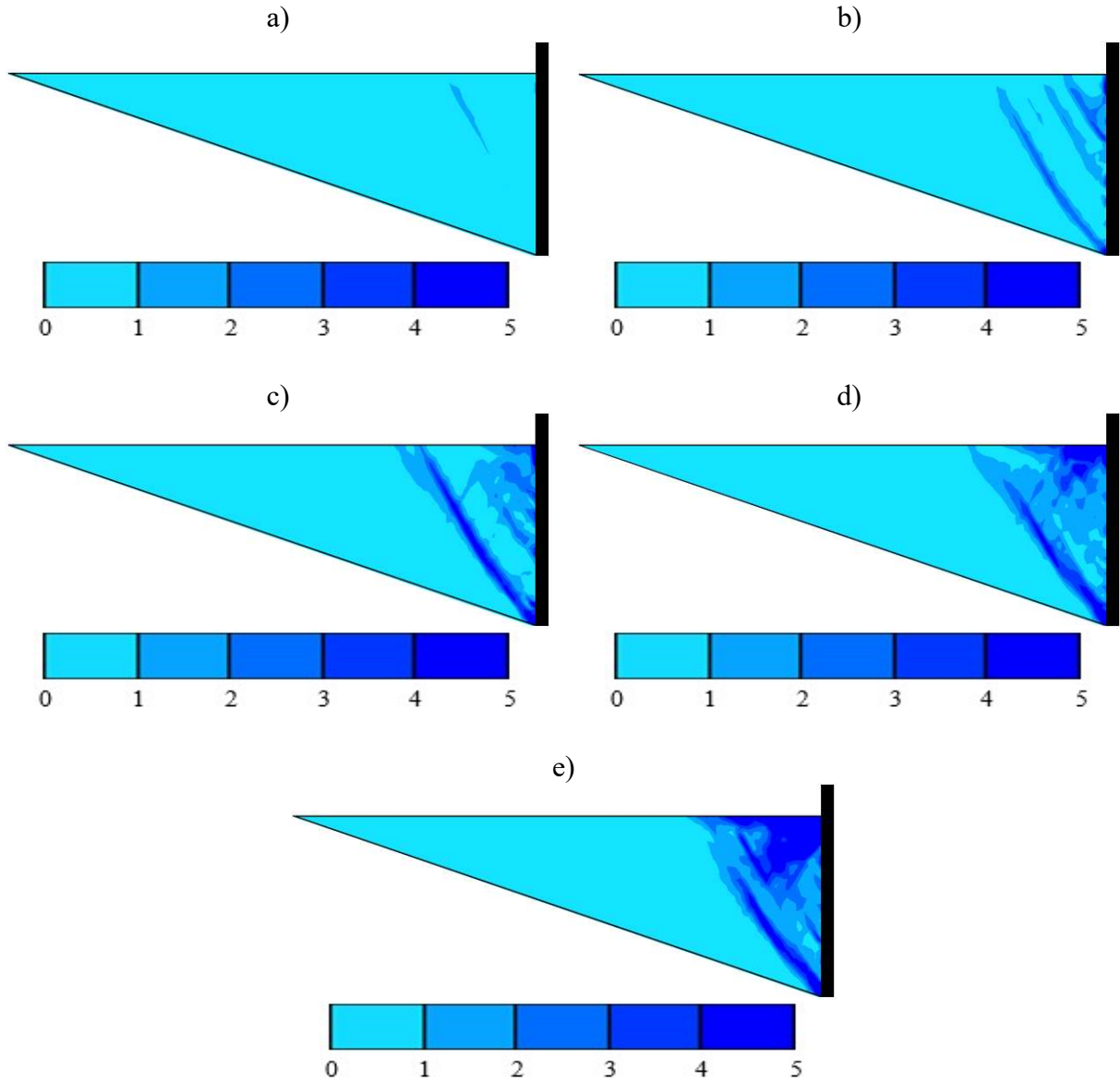
Figure 6.10 – Distributions of maximum lateral earth pressures along the abutment height for the selected values of δ_h/h after 50 cycles of lateral displacements of the abutment.



Source: Elaborated by the author (2020).

As discussed in subsection 5.2 and 5.3, the behavior observed in Figure 6.10 is explained by the development of shear zones in the backfill due to cyclic lateral displacements of the abutment. Figure 6.11 presents shadings of deviatoric strain in the backfill for all analyzed amplitudes. The shadings show the formation of a particularly intense shear zone developing in the upper third of the abutment. The intensity of shearing increased with increasing amplitude.

Figure 6.11 – Shadings of deviatoric strains (in %) in the backfill accumulated after 50 cycles of δ_h/h equal to: a) 1 mm; b) 2 mm; c) 3 mm; d) 4 mm; e) 5 mm.

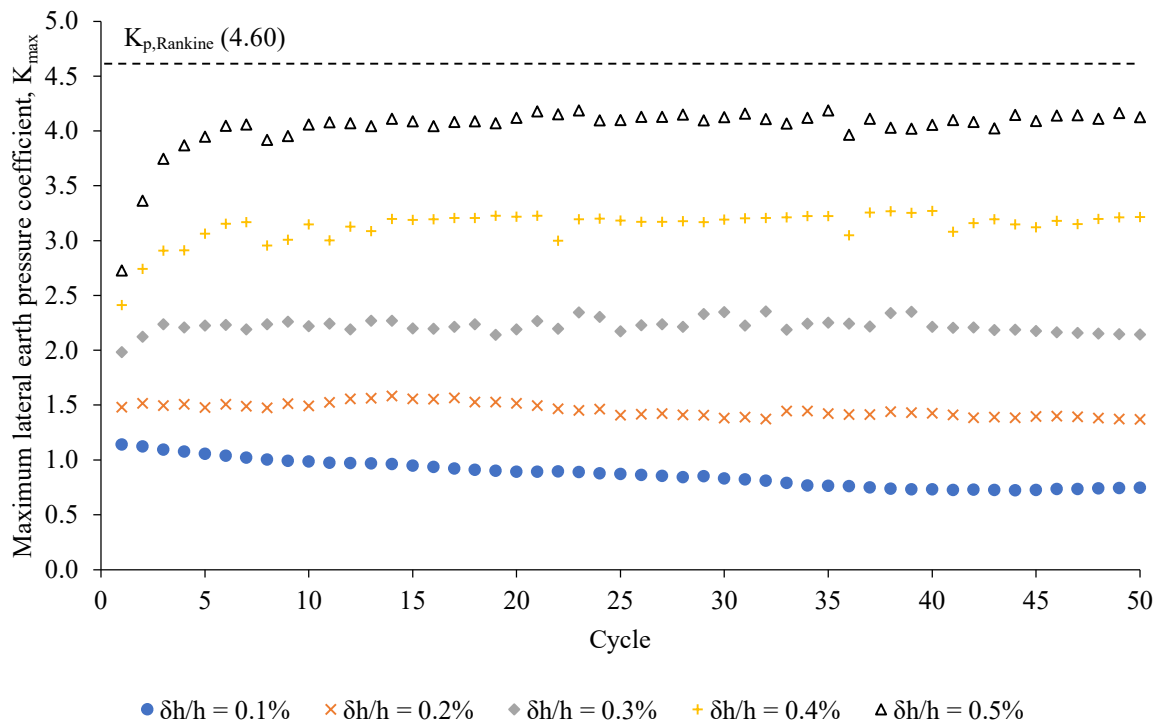


Source: Elaborated by the author (2020).

Figure 6.12 shows the evolution of K_{\max} with the cycles. K_{\max} remained below $K_{p, \text{Rankine}}$ with all selected displacement amplitudes. For $\delta_h/h = 0.1\%$, K_{\max} presented a slight decrease within the first 40 cycles and then reached the steady state around 0.75. For $\delta_h/h = 0.2\%$, K_{\max} remained virtually constant around 1.5. For $\delta_h/h = 0.3\%$, 0.4% and 0.5% , K_{\max} increased within the initial cycles and then reached the steady state around 2.25, 3.2 and 4.1, respectively. As discussed in subsection 2.3, the behavior shown in Figure 6.12 can be explained by the effects of densification and granular flow of the soil produced by cycling. In the case of $\delta_h/h = 0.1\%$, the effect of soil granular flow prevailed over the effect of soil densification within the first 40 cycles, what reduced the maximum lateral earth pressure coefficient. A balance between both

effects was reached afterward, and K_{\max} became constant. The amplitude of $\delta_h/h = 0.2\%$ resulted in a constant maximum lateral earth pressure coefficient, which revealed a balance between densification and granular flow effects. On the other hand, for δ_h/h equal to 0.3%, 0.4% and 0.5%, the effect of soil densification prevailed over the effect of soil granular flow within the initial cycles. Eventually, a balance between both effects was reached with increasing cycles, and K_{\max} remained unchanged.

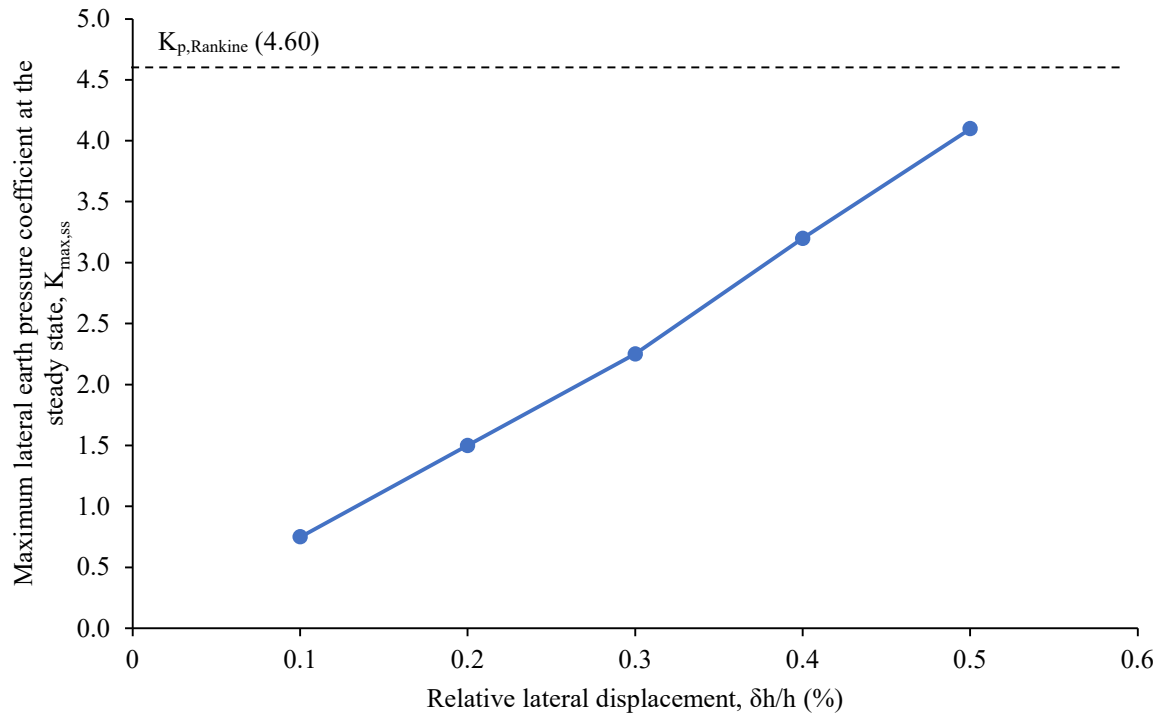
Figure 6.12 – Maximum lateral earth pressure coefficients with cycles considering the selected values of δ_h/h .



Source: Elaborated by the author (2020).

For a better understanding of the influence of the lateral displacement amplitude on the maximum lateral earth pressures, the maximum lateral earth pressure coefficient at the steady state ($K_{\max,ss}$) was plotted against δ_h/h , as shown in Figure 6.13. It is possible to observe that $K_{\max,ss}$ increased with δ_h/h according to an approximately linear fashion. Moreover, the results showed that maximum lateral earth pressure predictions with $K_{p,Rankine}$ proved to be on the safe side until $\delta_h/h = 0.55$. Similar results to those presented in Figures 6.10, 6.12, and 6.13 were obtained in experimental tests and numerical simulations performed by Abdel-Fattah and Abdel-Fattah (2019), Abdel-Fattah, Abdel-Fattah and Hemada (2018), England, Tsang and Bush (2000), Gabrieli, Zorzi and Wan (2015), Ng, Springman and Norrish (1998), and Zorzi, Artoni and Gabrieli (2017).

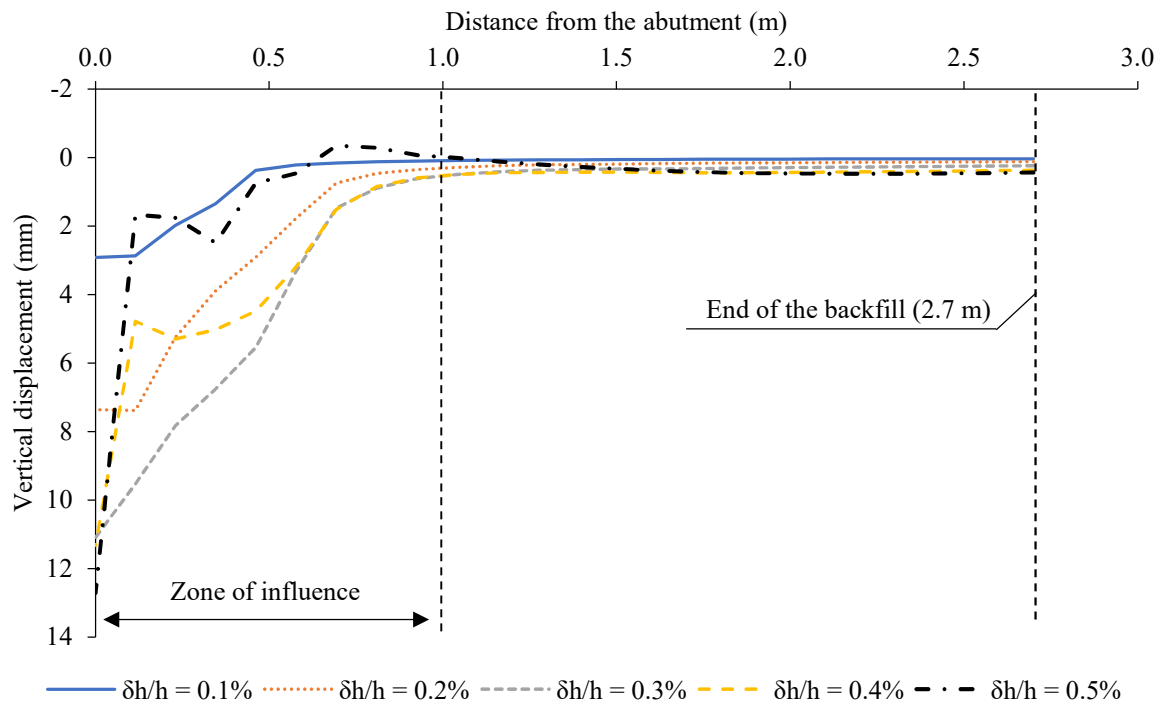
Figure 6.13 – Variation of the maximum lateral earth pressure coefficients at the steady state with the relative lateral displacements.



Source: Elaborated by the author (2020).

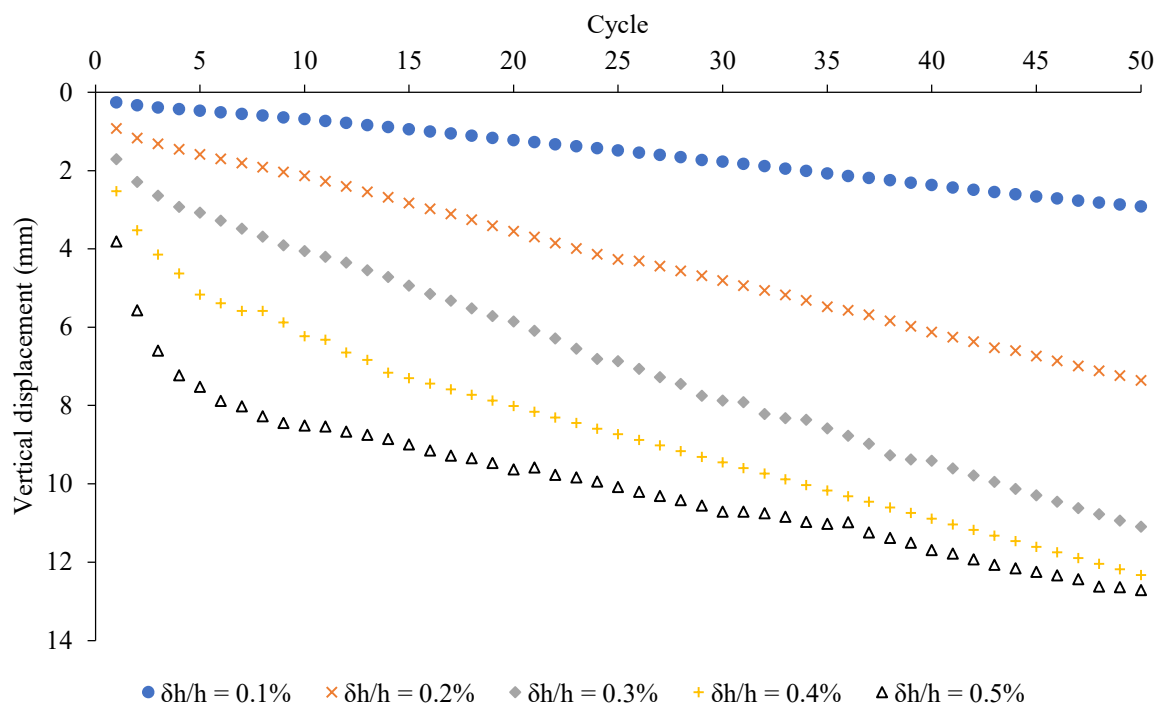
Vertical displacement profiles of the backfill surface along the distance from the abutment for the different values of δ_h/h after 50 cycles were also analyzed (Figure 6.14). The displacement was obtained at the end of each cycle. Settlements were considered positive and heave values negative. All lateral displacement amplitudes yielded maximum settlements near the backfill-abutment interface. A heave zone was not identified on the backfill surface for δ_h/h equal to 0.1% to 0.4%. On the other hand, the cyclic lateral displacement of $\delta_h/h = 0.5\%$ caused a heave in the soil mass. The zone where displacements are significant can be assumed to occur within a distance equal to the abutment height measured from the abutment. Figure 6.15 shows the variation of the vertical displacements at the top of the backfill-abutment interface with cycles. For all values of δ_h/h , settlements increased with cycles. For δ_h/h equal to 0.1% and 0.2%, settlements increased according to a virtually linear fashion from the beginning of cycling. On the other hand, for δ_h/h equal to 0.3%, 0.4%, and 0.5%, settlements firstly presented a nonlinear increase with a decreasing rate in the initial cycles, followed by a nearly linear increase. No tendency of reaching the steady state was noted.

Figure 6.14 – Vertical displacement profiles of the backfill surface along the distance from the abutment for the different values of $\delta h/h$ after 50 cycles.



Source: Elaborated by the author (2020).

Figure 6.15 – Vertical displacements on the top of the backfill-abutment interface with cycles considering the different values of $\delta h/h$.

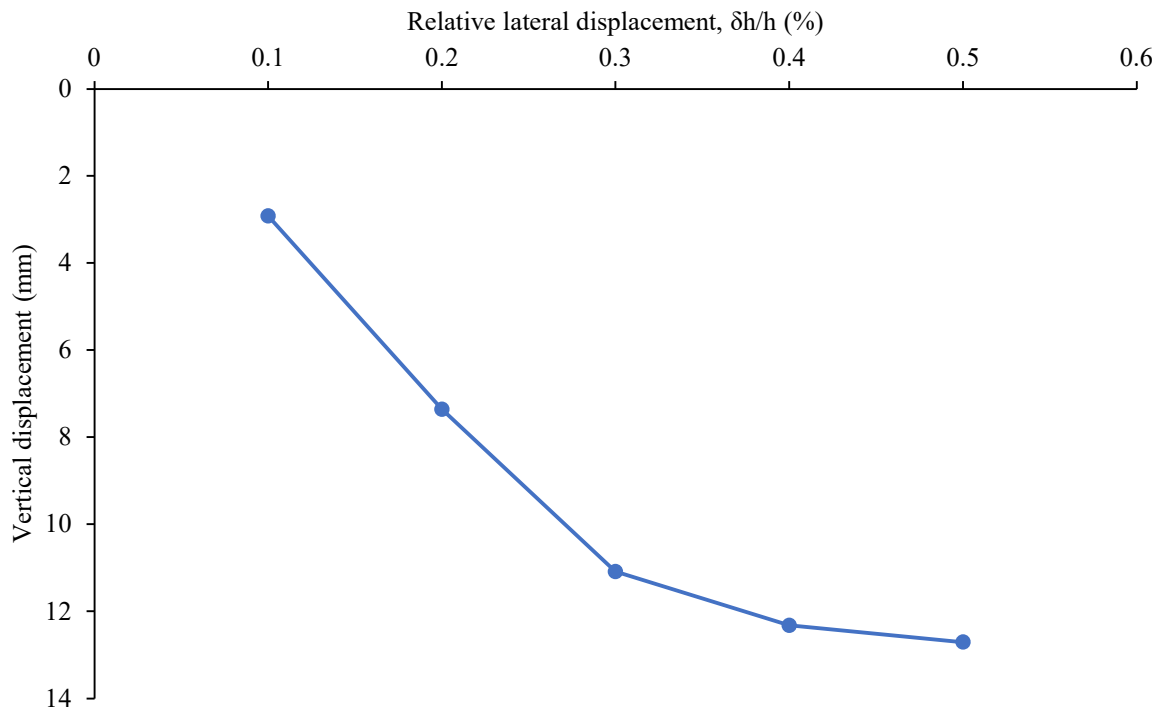


Source: Elaborated by the author (2020).

As discussed in subsections 5.2 and 5.3, the behavior observed for the vertical displacement of the backfill surface can be related to the effects of soil densification and granular flow. Displacement amplitudes of 0.1%, 0.2%, 0.3%, and 0.4% were sufficient to cause densification of the soil near the backfill-abutment interface, but not to produce a soil granular flow that could raise the backfill surface. On the other hand, the displacement amplitude of 0.5% was sufficient to densify the soil near the backfill-abutment interface and produce a soil granular flow that raised the backfill surface. In the case of δ_h/h equal to 0.1%, despite having prevailed over the effect of soil densification, the magnitude of the effect of soil granular flow was not enough to affect the behavior of the settlement with the cycles. For δ_h/h equal to 0.2%, a balance between both effects occurred from the beginning of the cyclic lateral displacements of the abutment. On the other hand, for δ_h/h equal to 0.3%, 0.4% and 0.5%, the effect of soil densification prevailed over the effect of soil granular flow within the first cycles. Then, a balance between both effects was reached.

For a better understanding of the influence of the lateral displacement amplitude on the vertical displacement on the backfill surface, the maximum settlement obtained after 50 cycles of lateral displacement of the abutment was plotted against δ_h/h , as shown in Figure 6.16. It is possible to observe that the settlement tended to stabilize after undergoing an initial increase. Similar results to those presented in Figures 6.14, 6.15, and 6.16 were obtained in numerical simulations performed by England, Tsang and Bush (2000), and Ng, Springman and Norrish (1998).

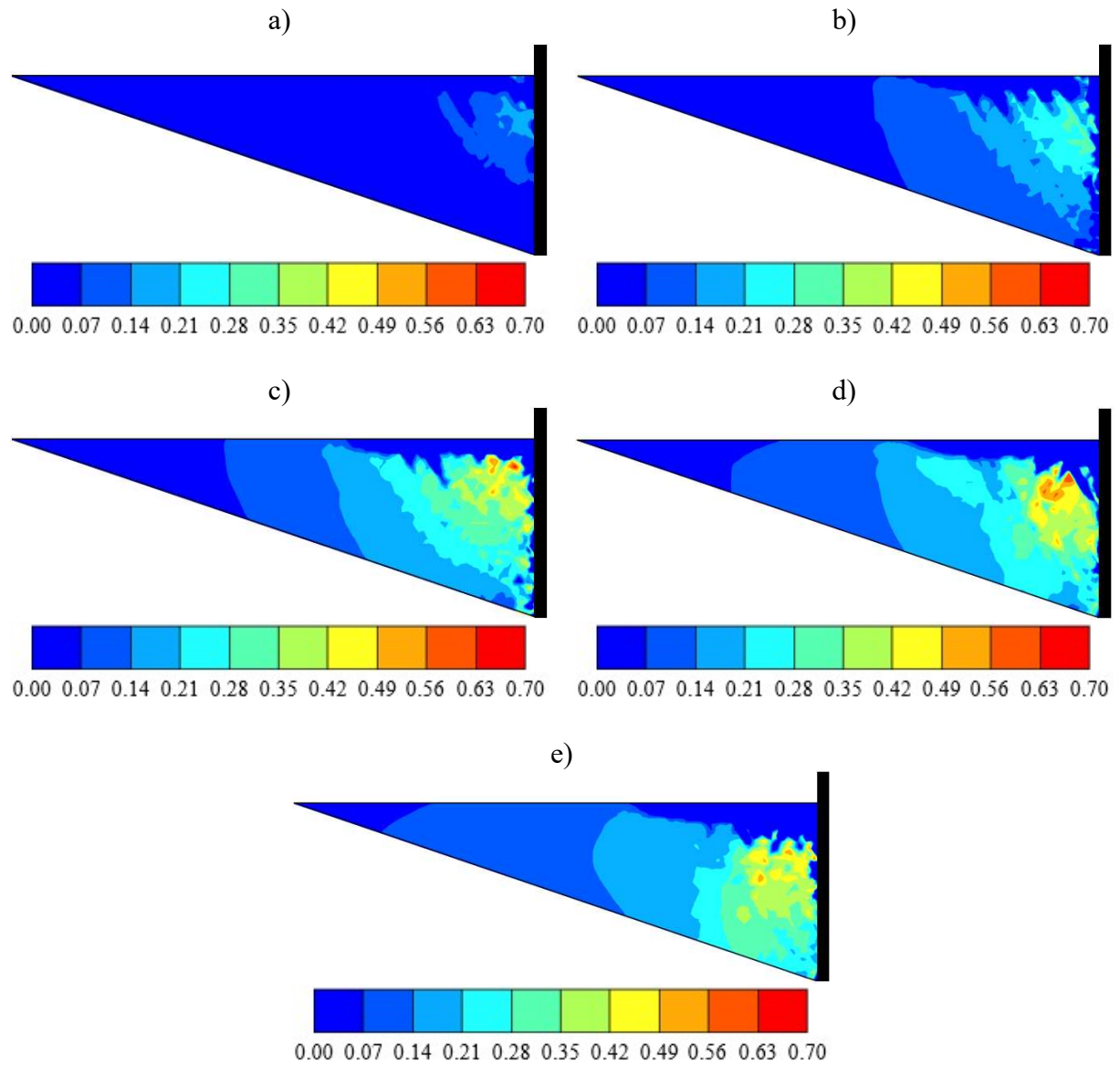
Figure 6.16 – Variation of the vertical displacement on the top of the backfill-abutment interface with the relative lateral displacements after 50 cycles.



Source: Elaborated by the author (2020).

The behavior of the maximum settlement with the lateral displacement amplitude can be related to the backfill densification. Backfill soil densification can be checked in Figure 6.17, which shows compressive volumetric strains in the backfill accumulated after 50 cycles of lateral displacement of the abutment for the selected values of δ_h/h . The shadings show that the compressive volumetric strains increased with increasing δ_h/h . With the lowest values of δ_h/h , compressive volumetric strains were significantly affected by the variation of the amplitude of lateral displacement of the abutment. However, it became less significant with the largest values of δ_h/h .

Figure 6.17 – Shadings of compression volumetric strains (in %) in the backfill accumulated after 50 cycles of δ_h/h equal to: a) 1 mm; b) 2 mm; c) 3 mm; d) 4 mm; e) 5 mm.



Source: Elaborated by the author (2020).

7 LESSONS LEARNED FROM THE SIAB NUMERICAL INVESTIGATION

Some aspects of interest regarding the SIAB design are discussed in this section. A preliminary analysis should be performed to identify the lateral earth pressure distribution that can be used to design the bridge abutment. Lateral earth pressures calculated from Rankine's theory showed to be on the safe side within a lateral displacement amplitude of about 0.5% of the abutment height. For higher amplitudes, it is suggested that the lateral displacement amplitude of the abutment be considered in the methodology to calculate the lateral earth pressures on the abutment, as also suggested by England, Tsang and Bush (2000).

The results of the numerical simulations showed that the vertical displacements on the backfill surface were more influenced by the cyclic lateral displacements of the abutment within a zone with dimension equal to the abutment height measured from the abutment. Moreover, the vertical displacements within this zone increased with the cycles. Therefore, solutions to control and/or reduce the evolution of the vertical displacements on the backfill surface with cycling within a distance from the abutment equal to the abutment height or more should be anticipated to avoid safety and riding-quality issues for bridge users. Rubberized and/or reinforced backfills and/or the use of expanded polystyrene inclusions have been proposed elsewhere (AL-QARAWI; LEO; LIYANAPATHIRANA, 2020; ARGYROUDIS et al., 2016; CARISTO; BARNES; MITOULIS, 2018; TATSUOKA et al., 2009; ZADEHMOHAMAD; BAZAZ, 2019) as an alternative to conventional backfilling.

The completion season of the bridge construction should be considered in the design of IABs and SIABs since it influences the vertical displacements on the backfill surface (ENGLAND; TSANG; BUSH, 2000). In the present analysis, the largest backfill vertical displacements were found to occur for a bridge finished in summer while the smallest ones were found to take place for a bridge finished in winter. The design should include analyses of both scenarios (i.e., bridge completed in summer and winter) in order to define the most unfavorable situation since different responses can be obtained in each situation.

Finally, it is important to point out that the suggestions presented in this section were given based on the results of numerical simulations considering the characteristics of the bridge analyzed in the present investigation. Therefore, these suggestions should be understood as preliminary. The different aspects must be verified by considering the particularities of each project.

8 CONCLUDING REMARKS

8.1 Summary

The present investigation assessed the effects of cyclic lateral displacements on the response of the backfill-abutment system of a semi-integral abutment bridge (SIAB). A finite element numerical model was developed and validated based on the project and field monitoring of an instrumented SIAB located near the city of Palestine, Texas, United States of American. Analyses of the response of the backfill-abutment system upon daily and annual cyclic lateral displacements of the abutment were carried out after validation of the numerical model. The daily response analysis was based on the numerical simulation performed to validate the numerical model. On the other hand, the annual response analysis was carried out taking into consideration design thermal variations recommended to the geographic location of the bridge.

A parametric analysis with parameters of interest was performed after the analyses of the daily and annual responses of the backfill-abutment system. Numerical simulations in this phase of the investigation included studying the influence of the completion season of the bridge construction, the foundation stiffness, and the lateral displacement amplitude. To address the effect of the completion season of the bridge construction, four scenarios (spring, summer, autumn, and winter) were analyzed by considering the same thermal variation used to predict the annual response of the abutment. Three profiles of steel sheet pile (PZC-12, PZC-18, and PZC-28) were selected to assess the influence of the foundation stiffness by considering the same thermal variation adopted to predict the annual response and the bridge construction completed in summer. Finally, five relative lateral displacements (0.1%, 0.2%, 0.3%, 0.4% and 0.5% of the abutment height) were evaluated by considering the bridge construction completed in summer.

The main findings of this research are as follows:

- Predictions with the finite element numerical model produced good matches with the field data.
- The lateral earth pressure presented a nonlinear distribution along the abutment height in all numerical simulations.
- Cyclic lateral displacements of the abutment resulted in a zone of vertical displacements on the backfill surface with dimension equal to abutment height measured from the abutment in all numerical simulations.

- Vertical displacements on the backfill surface increased with cycles in all investigated conditions, which indicates the occurrence of ratcheting in the backfill.
- The largest downward vertical displacement (settlement) of the backfill surface occurred near the backfill-abutment interface and decreased with the distance from the abutment in all investigated conditions.
- Maximum lateral earth pressures were more affected by the cyclic lateral displacements of the abutment than minimum lateral earth pressures.
- The largest daily maximum lateral earth pressures occurred within the upper and bottom thirds of the abutment while the largest annual maximum lateral earth pressures occurred within the middle third of the abutment.
- The largest daily and annual minimum lateral earth pressures were developed within the bottom third of the abutment.
- Daily and annual maximum lateral earth pressure coefficients were lower than Rankine's passive lateral earth pressure coefficient while daily and annual minimum lateral earth pressure coefficients were close to Rankine's active lateral earth pressure coefficient.
- Daily maximum lateral earth pressure coefficient presented a variable behavior with cycles, which included alternating reduction and escalation, while the annual maximum lateral earth pressure coefficient firstly increased with cycles and then reached stabilization (steady state).
- Daily minimum lateral earth pressure coefficient firstly decreased with cycles and then reached the steady state while the annual minimum lateral earth pressure coefficient remained virtually constant.
- While a tendency of upward vertical displacement (heave) on the backfill surface was not observed with the daily cycle analysis, a heave zone was formed at a certain distance from the abutment with the annual cycle analysis.
- The settlement at the top of the backfill-abutment interface increased according to a nonlinear fashion with a decreasing rate for daily cycles while, for annual cycles, the settlement at the top of the backfill-abutment interface firstly presented a nonlinear increase with a decreasing rate within the first cycles and then increased according to a linear fashion.
- The maximum lateral earth pressure was not influenced by the completion season of the bridge construction.

- The vertical displacement of the backfill surface was influenced by the completion season of the bridge construction since the different initial movements of the abutment resulted in different initial responses to the backfill.
- The largest settlements occurred for the bridge construction completed in the summer season while the smallest settlements occurred for the bridge construction completed in the winter season. Therefore, completing the construction of the bridge in the summer season represented the most unfavorable situation.
- The absence of integration between the abutment and the foundation minimized the influence of foundation stiffness on the response of the backfill-abutment system.
- The maximum lateral earth pressures on the abutment and the vertical displacements of the backfill surface increased with increasing amplitude of lateral displacement.
- The largest values of maximum lateral earth pressure occurred within the upper and bottom thirds of the abutment, for the lowest value of lateral displacement, while, for the largest value of lateral displacement, the maximum lateral earth pressure concentrated at the middle third of the abutment.
- Comparatively smaller amplitudes caused a reduction of the maximum lateral earth pressure coefficient with cycles, while comparatively higher amplitudes caused an increase of the maximum lateral earth pressure coefficient with cycles. In both situations, the steady state was reached.
- The maximum lateral earth pressure coefficient in the steady state increased with the relative lateral displacement according to an approximately linear fashion, and no tendency of reaching a stabilization was observed.
- Maximum lateral earth pressure predictions with Rankine's passive lateral earth pressure coefficient proved to be on the safe side until a relative lateral displacement equal to 0.55% of the abutment height.
- No tendency of heave was observed on the backfill surface for comparatively smaller amplitudes, while a heave zone was formed at a certain distance from the abutment for comparatively higher amplitudes.
- For comparatively smaller amplitudes, the settlement at the top of the backfill-abutment interface increased according to a linear fashion, while for comparatively higher amplitudes, it firstly presented a nonlinear increase with a decreasing rate

within the first cycles and then increased according to a linear fashion, for comparatively higher amplitudes.

- The settlement at the top of the backfill-abutment interface tended to stabilization after undergoing an initial increase.

8.2 Recommendations for future research

During the execution of this research, other interesting aspects regarding the response of the backfill upon cyclic lateral displacements of the abutment were identified and are cited below:

- the influence of the backfill stiffness,
- the effect of reinforcements on the backfill performance,
- the influence of isolated and combined movements of rotation and translation of the abutment,
- combined effects of temperature, creep, and shrinkage,
- the effect of dynamic loading,
- the response of non-granular materials,
- the response of the combination of non-granular and granular materials,
- the development of instrumented physical models and discrete element numerical models to investigate parameters of interest.

REFERENCES

AASHTO. **AASHTO LRFD bridge design specifications**. New York: AASHTO, 2012.

ABDEL-FATTAH, M. T.; ABDEL-FATTAH, T. T. Behavior of integral frame abutment bridges due to cyclic thermal loading: nonlinear finite-element analysis. **Journal of Bridge Engineering**, ASCE, v. 24, n. 5, p. 1-15, 2019.

ABDEL-FATTAH, M. T.; ABDEL-FATTAH, T. T.; HEMADA, A. A. Nonlinear finite-element analysis of integral abutment bridges due to cyclic thermal changes. **Journal of Bridge Engineering**, ASCE, v. 23, n. 2, p. 1-13, 2018.

ABDOLLAHI, E.; CHAKHERLOU, T. N. Numerical and experimental study of ratcheting in cold expanded plate of Al-alloy 2024-T3 in double shear lap joints. **Fatigue & Fracture of Engineering Materials & Structures**, Wiley, v. 42, p. 209-222, 2019.

ABENDROTH, R. E.; GREIMANN, L. F. **Field testing of integral abutments**. Report No HR-399. Ames: Iowa State University and Iowa Department of Transportation, 2005.

AHN, J.; YOON, J.; KIM, J.; KIM, S. Evaluation on the behavior of abutment-pile connection in integral abutment bridge. **Journal of Constructional Steel Research**, Elsevier, v. 67, p. 1134-1148, 2011.

AL-ANI, M.; MURASHEV, A.; PALERMO, A.; ANDISHEH, K.; WOOD, J.; GOODALL, D.; LLOYD, N. Criteria and guidance for the design of integral bridges. **Proceedings of the Institution of Civil Engineers – Bridge Engineering**, ICE, v. 171, n. 3, p. 143-154, 2018.

AL-QARAWI, A.; LEO, C.; LIYANAPATHIRANA, D. S. Effects of wall movements on performance of integral abutment bridges. **International Journal of Geomechanics**, ASCE, v. 20, n. 2, p. 1-14, 2020.

ALONSO-MARROQUÍN, F.; HERRMANN, H. J. Ratcheting of granular materials. **Physical Review Letters**, The American Physical Society, v. 92, n. 5, p. 1-4, 2004.

ARGYROUDIS, S.; PALAIOCHORINOU, A.; MITOULIS, S.; PITILAKIS, D. Use of rubberised backfills for improving the seismic response of integral abutment bridges. **Bull Earthquake Eng**, Springer, v. 14, p. 3573-3590, 2016.

ARSOY, S.; BARKER, R. M.; DUNCAN, J. M. **The behavior of integral abutment bridges**. FHWA/VTRC 00-CR3. Charlottesville: Virginia Transportation Research Council and Virginia Department of Transportation, 1999.

ARSOY, S.; DUNCAN, J. M.; BARKER, R. M. Behavior of a semiintegral bridge abutment under static and temperature-induced cyclic loading. **Journal of Bridge Engineering**, ASCE, v. 9, n. 2, p. 193-199, 2004.

ASTM. **ASTM D-7181**: Method for consolidated drained triaxial compression test for soils. West Conshohocken: ASTM, 2011.

BAKEER, R. M.; MATTEI, N. J.; ALMALIK, B. K.; CARR, S. P.; HOMES, D. **Evaluation of DOTD semi-integral bridge and abutment system**. FHWA/LA.05/397. Baton Rouge: Louisiana Transportation Research Center, 2005.

BANKS, J. R.; BLOODWORTH, A. G. Lateral stress profiles on integral bridge abutments. **Proceedings of the Institution of Civil Engineers – Bridge Engineering**, ICE, v. 171, n. 3, p. 155-168, 2018.

BARR, P. J.; STANTON, J. F.; EBERHARD, M. O. Effects of temperature variations on precast, prestressed concrete bridge girders. **Journal of Bridge Engineering**, ASCE, v. 10, n. 2, p. 186-194, 2005.

BLOODWORTH, A. G.; XU, M.; BANKS, J. R.; CLAYTON, C. R. I. Predicting the earth pressure on integral bridge abutments. **Journal of Bridge Engineering**, ASCE, v. 17, n. 2, p. 371-381, 2012.

BOULBIBANE, M.; WEICHERT, D. Application of shakedown theory to soils with non associated flow rules. **Mechanics Research Communications**, Elsevier Science, v. 24, n. 5, p. 513-519, 1997.

BOWLES, J. E. **Foundation analysis and design**. 5 ed. Singapore: McGraw-Hill, 1997.

BREE, J. Elastic-plastic behaviour of thin tubes subjected to internal pressure and intermittent high-heat fluxes with application to fast-nuclear-reactor fuel elements. **The Journal of Strain Analysis for Engineering Design**, SAGE, v. 2, n. 3, p. 226-238, 1967.

BREÑA, S. F.; BONCZAR, C. H.; CIVJAN, S. A.; DEJONG, J. T.; CROVO, D. S. Evaluation of seasonal and yearly behavior of an integral abutment bridge. **Journal of Bridge Engineering**, ASCE, v. 12, n. 3, p. 296-305, 2007.

BRINKGREVE, R. B. J.; KUMARSWAMY, S.; SWOLFS, W. M. **Plaxis 2D version 2016: material models manual**. Delft: Plaxis bv, 2016a.

BRINKGREVE, R. B. J.; KUMARSWAMY, S.; SWOLFS, W. M. **Plaxis 2D version 2016: reference manual**. Delft: Plaxis bv, 2016b.

BURKE JR, M. P. **Integral & semi-integral bridges**. Oxford: Wiley & Sons, 2009.

CAI, Z.; ROSS, R. J. Mechanical properties of wood-based composite materials. *In*: ROSS, R. J. **Wood handbook: wood as an engineering material**. Centennial Edition. Washington: Department of Agriculture, 2010.

CARISTO, A.; BARNES, J.; MITOULIS, S. A. Numerical modelling of integral abutment bridges under seasonal thermal cycles. **Proceedings of the Institution of Civil Engineers – Bridge Engineering**, ICE, v. 171, n. 3, p. 179-190, 2018.

CARLSTEDT, E. **Soil-structure interaction for bridges with backwalls: FE-analysis using Plaxis**. 2008. 66 f. Thesis (Master's Degree in Structural Design and Bridge) – Royal Institute of Technology, Stockholm, 2008.

CHEN, B.; DING, R.; ZHENG, J.; ZHANG, S. Field test on temperature field and thermal stress for prestressed concrete box-girder bridge. **Frontiers of Architecture and Civil Engineering in China**, Springer, v. 3, n. 2, p. 158-164, 2009.

CIVJAN, S. A.; BONCZAR, C.; BREÑA, S. F.; DEJONG, J.; CROVO, D. Integral abutment bridge behavior: parametric analysis of a Massachusetts bridge. **Journal of Bridge Engineering**, ASCE, v. 12, n. 1, p. 64-71, 2007.

CIVJAN, S. A.; KALAYCI, E.; QUINN, B. H.; BREÑA, S. F.; ALLEN, C. A. Observed integral abutment bridge substructure response. **Engineering Structures**, Elsevier, v. 56, p. 1177-1191, 2013.

CLAYTON, C. R. I.; XU, M.; BLOODWORTH, A. A laboratory study of the development of earth pressure behind integral bridge abutments. **Géotechnique**, ICE, v. 56, n. 8, p. 561-571, 2006.

CLOUGH, G. W.; DUNCAN, J. M. Earth pressure. *In*: FANG, H. **Foundation engineering handbook**. 2 ed. New York: Chapman & Hall, 1991.

COLLINS, I. F.; BOULBIBANE, M. The application of shakedown theory to pavement design. **Metals and Materials**, v. 4, n. 4, p. 832-837, 1998.

COSTA, Y. D. J.; ZORNBERG, J. G. Active and passive arching stresses outside a deep trapdoor. **Acta Geotechnica**, Springer, 2020.

DAFALIAS, Y. F.; HERRMANN, L. R. Bounding surface formulation of soil plasticity. *In*: PANDE, G. N.; ZIENKIEWICZ, O. C. **Soil mechanics-transient and cyclic loads: constitutive relations and numerical treatment**. 1 ed. Chichester: Wiley & Sons, 1982.

DAVID, T. K.; FORTH, J. P. Modelling of soil structure interaction of integral abutment bridges. **International Journal of Civil, Environmental, Structural, Construction and Architectural Engineering**, World Academy of Science, Engineering and Technology, v. 5, n. 6, p. 287-292, 2011.

DAVID, T. K.; FORTH, J. P.; YE, J. Superstructure behavior of a stub-type integral abutment bridge. **Journal of Bridge Engineering**, ASCE, v. 19, n. 6, p. 1-12, 2014.

DAVIDS, W. G.; SANDFORD, T.; ASHLEY, S.; DELANO, J.; LYONS, C. Field-measured response of an integral abutment bridge with short steel H-piles. **Journal of Bridge Engineering**, ASCE, v. 15, n. 1, p. 32-43, 2010.

DUDERSTADT, F. J.; COYLE, H. M.; BARTOSKEWITZ, R. E. **Correlation of the Texas Cone Penetrometer test N-value with soil shear strength**. FHWA/TX77-10-3F. College Station: Texas A&M University, 1977.

DUNCAN, J. M.; CHANG, C. Nonlinear analysis of stress and strain in soils. **Journal of the Soil Mechanics and Foundations Division**, ASCE, v. 96, n. 5, p. 1629-1653, 1970.

EFRETUEI, E. O. **Thermal impact on soil-structure interaction for integral bridges**. 2013. 267 f. Dissertation (Doctor's Degree of Philosophy) – University of Leeds, Leeds, 2013.

EMERSON, M. **Temperature differences in bridges**: basis of design requirements. TRRL Laboratory Report 765. Crowthorne: Transport and Road Research Laboratory, 1977.

ENGLAND, G. L.; TSANG, N. C. M.; BUSH, D. I. **Integral bridges**: a fundamental approach to the time-temperature loading problem. London: Thomas Telford, 2000.

FRANCHIN, P.; PINTO, P. E. Performance-based seismic design of integral abutment bridges. **Bull Earthquake Eng**, Springer, v. 12, p. 939-960, 2014.

FROSCH, R. J.; LOVELL, M. D. **Long-term behavior of integral abutment bridges**. FHWA/IN/JTRP-2011/16. West Lafayette: Indiana Department of Transportation and Purdue University, 2011.

GABRIELI, F.; ZORZI, G.; WAN, R. Granular ratcheting phenomena behind a model retaining wall. In: SOGA, K.; KUMAR, K.; BISCONTIN, G.; KUO, M. **Geomechanics from micro to macro**. London: Taylor & Francis Group, 2005.

GANGONE, M. V.; WHELAN, M. F.; FANOYAN, K. D.; MINNETYAN, L. Experimental characterization and diagnostics of the early-age behavior of a semi-integral abutment FRP deck bridge. **Sensor Review**, v. 32, n. 4, p. 296-309, 2012.

GEOKON. **Instruction manual**: model 4800 series VW earth pressure cells. Lebanon: Geokon, 2019a.

GEOKON. **Instruction manual**: model LC-2x4 4 channel VW datalogger. Lebanon: Geokon, 2019b.

GERDAU. **Steel sheet piling**: quick reference guide. Midlothian: Gerdau, 2019.

GHADIMI, B.; NIKRAZ, H.; ROSANO, M. Dynamic simulation of a flexible pavement layers considering shakedown effects and soil-asphalt interaction. **Transportation Geotechnics**, Elsevier, v. 7, p. 40-58, 2016.

GOOGLE MAPS. **Mack Creek Bridge location**. Available on: <https://www.google.com/maps/place/31%C2%B040'29.9%22N+95%C2%B043'26.6%22W/@31.6747495,-95.7251196,17.25z/data=!4m5!3m4!1s0x0:0x0!8m2!3d31.6749722!4d-95.7240556>. Access on: Aug 29th, 2019.

HAMBLY, E. C.; BURLAND, J. B. **Bridge foundations and substructures**. [S. I.]: Crown, 1979.

HAMOUDI, M. M.; COYLE, H. M.; BARTOSKEWITZ, R. E. **Correlation of the Texas Highway Department Cone Penetrometer test with unconsolidated-undrained shear strength of cohesive soils**. Research Report 10-1. College Station: Texas Transportation Institute, 1974.

HANDY, R. L. The arch in soil arching. **Journal of Geotechnical Engineer**, ASCE, v. 111, n. 3, p. 302-318, 1985.

HASSIOTIS, S.; KHODAIR, Y.; ROMAN, E.; DEHNE, Y. **Evaluation of integral bridge abutments**. Report No NJ-2005-025. [S. I.]: Federal Highway Administration, 2006.

HEDEGAARD, B. D.; FRENCH, C. E. W.; SHIELD, C. K. Investigation of thermal gradient effects in the I-35W St. Anthony Falls Bridge. **Journal of Bridge Engineering**, ASCE, v. 18, n. 9, p. 890-900, 2013.

HOFFMAN, P. C.; MCCLURE, R. M.; WEST, H. H. Temperature study of an experimental segmental concrete bridge. **PCI Journal**, p. 78-97, 1983.

HOPPE, E. J.; GOMEZ, J. P. **Field study of an integral backwall bridge**. Final report. Virginia: Virginia Transportation Research Council, 1996.

HORVATH, J. S. Integral-abutment bridges: a complex soil-structure interaction challenge. **Geotechnical Engineering for Transportation Projects**, ASCE, p. 460-469, 2004.

HOULSBY, G. T.; ABADIE, C. N.; BEUCKELAERS, W. J. A. P.; BYRNE, B. W. A model for nonlinear hysteretic and ratcheting behaviour. **International Journal of Solids and Structures**, Elsevier, p. 1-14, 2017.

HUNTLEY, S. A.; VALSANGKAR, A. J. Field monitoring of earth pressures on integral bridge abutments. **Canadian Geotechnical Journal**, NRC Research Press, v. 50, p. 841-857, 2013.

HUSAIN, I.; BAGNARIOL, D. **Integral abutment bridges**. Report SO-96-01. St. Catharines: Ministry of Transportation, 1999.

HUSAIN, I.; BAGNARIOL, D. **Semi-integral abutment bridges**. Report BO-99-03. Toronto: Ministry of Transportation, 1999.

ILES, D. C. Integral bridges in the UK. *In*: INTERNATIONAL WORKSHOP ON THE BRIDGES WITH INTEGRAL ABUTMENTS, 2006, Lulea. **Proceedings** [...]. Lulea: Lulea University of Technology, 2006.

IMBSEN, R. A.; VANDERSHAF, D. E.; SCHAMBER, R. A.; NUTT, R. V. **Thermal effects in concrete bridge superstructures**. NCHRP Report 276. New York: Transportation Research Board, 1985.

JANBU, N. Soil compressibility as determined by oedometer and triaxial tests. *In*: EUROPEAN CONFERENCE ON SOIL MECHANICS AND FOUNDATION ENGINEERING, 1., 1963, Wiesbaden. **Proceedings** [...]. Wiesbaden: ISSMFE, 1963.

JIA, P.; KONG, L. Modeling of ratcheting accumulation of secondary deformation due to stress-controlled high-cyclic loading in granular soils. **J. Cent. South Univ.**, Springer, v. 22, p. 2306-2315, 2015.

KANG, C.; SCHNEIDER, S.; WENNER, M.; MARX, S. Development of design and construction of high-speed railway bridges in Germany. **Engineering Structures**, Elsevier, v. 163, p. 184-196, 2018.

KARALAR, M.; DICLELI, M. Fatigue in jointless bridge H-piles under axial load and thermal movements. **Journal of Constructional Steel Research**, Elsevier, v. 147, p. 504-522, 2018.

KIM, S.; AHN, J.; JUNG, C.; JANG, J.; PARK, Y. Behaviour of steel-box semi-integral abutment bridge considering temperature-earth pressure change. **International Journal of Steel Structures**, Springer, v. 14, n. 1, p. 117-140, 2014.

KIM, W.; LAMAN, J. A. Seven-year field monitoring of four integral abutment bridges. **Journal of Performance of Constructed Facilities**, ASCE, v. 26, n. 1, p. 54-64, 2012.

KNAPPETT, J. A.; CAUCIS, K.; BROWN, M. J.; JEFFREY, J. R.; BALL, J. D. CHD pile performance: part II – numerical modelling. **Proceedings of the Institution of Civil Engineers – Geotechnical Engineering**, ICE, v. 169, n. 5, p. 436-454, 2016.

KONG, B.; CAI, C. S.; KONG, X. Field monitoring study of an integral abutment bridge supported by prestressed precast concrete piles on soft soil. **Engineering Structures**, Elsevier, v. 104, p. 18-31, 2015.

KONG, B.; CAI, C. S.; ZHANG, Y. Parametric study of an integral abutment bridge supported by prestressed precast concrete piles. **Engineering Structures**, Elsevier, v. 120, p. 37-48, 2016.

KULHAWY, F. H.; MAYNE, P. W. **Manual on estimating soil properties for foundation design**. Final Report. Res. Proj. 1493-6. New York: Cornell University, 1990.

KUNIN, J.; ALAMPALLI, S. Integral abutment bridges: current practice in United States and Canada. **Journal of Performance of Constructed Facilities**, ASCE, v. 14, n. 3, p. 104-111, 2000.

LADE, P. V.; NELSON, R. B. Modelling the elastic behaviour of granular materials. **International Journal for Numerical and Analytical Methods in Geomechanics**, Wiley, v. 11, n. 5, p. 521-542, 1987.

LAMAN, J. A.; KIM, W. S. **Monitoring of integral abutment bridges and design criteria development**. FHWA-PA-2009-005-PSU 002. University Park: The Pennsylvania State University, 2009.

LAN, C.; BRISEGHIELLA, B.; FENU, L.; XUE, J.; ZORDAN, T. The optimal shapes of piles in integral abutment bridges. **Journal of Traffic and Transportation Engineering**, Elsevier, v. 4, n. 6, p. 576-593, 2017.

LAN, C. **On the performance of super-long integral abutment bridges: parametric analyses and design optimization**. 2012. 210 f. Thesis (Master's Degree) – University of Trento, Trento, 2012.

- LAWSON, W. D.; TERRELL, E. O.; SURLES, J. G.; MOGHADDAM, R. B.; SEO, H.; JAYAWICKRAMA, P. W. Side-by-side correlation of Texas Cone Penetration and Standard Penetration test blowcount values. **Geotechnical and Geological Engineering**, Springer, v. 36, p. 2769-2787, 2018.
- LEE, D. J. **Bridge bearings and expansion joints**. 2 ed. London: E & FN Spon, 1994.
- LEHANE, B. M. Lateral soil stiffness adjacent to deep integral bridge abutments. **Géotechnique**, ICE, v. 61, n. 7, p. 593-603, 2011.
- MAHENDRAN, M. The modulus of elasticity of steel: is it 200 GPa?. *In*: 13th INTERNATIONAL SPECIALTY CONFERENCE ON COLD-FORMED STEEL STRUCTURES, 13., 1996, Missouri. **Proceedings** [...]. Missouri: Missouri University of Science and Technology, 1996.
- MARTHA, L. F. **Ftool**: two-dimensional frame analysis tool. Rio de Janeiro: Pontifical Catholic University of Rio de Janeiro, 2018.
- MARURI, R. F.; PETRO, S. H. Integral abutments and jointless bridges (IAJB) 2004 survey summary. *In*: THE 2005 – FHWA CONFERENCE, 2005, Baltimore. **Proceedings** [...]. Baltimore: West Virginia University, 2005.
- MESRI, G. Discussion on “New design procedure for stability of soft clays”. **J. Geotech. Eng. Div.**, ASCE, v. 101, p. 409-412, 1975.
- MISTRY, V. C. Integral abutment and jointless bridges. *In*: THE 2005 – FHWA CONFERENCE, 2005, Baltimore. **Proceedings** [...]. Baltimore: West Virginia University, 2005.
- MITOULIS, S. A.; PALAIOCHORINOU, A.; GEORGIADIS, I.; ARGYROUDIS, S. Extending the application of integral frame abutment bridges in earthquake-prone areas by using novel isolators of recycled materials. **Earthquake Engineering & Structural Dynamics**, International Association for Earthquake Engineering, v. 45, p. 2283-2301, 2016.
- MOGHADDAM, R. B. **Evaluation of the TxDOT Texas Cone Penetration test and foundation design method including correction factors, allowable total capacity, and resistance factors at serviceability limit state**. 2016. 153 f. Dissertation (Doctor's Degree of Philosophy) – Texas Tech University, Lubbock, 2016.
- MOORTY, S.; ROEDER, C. W. Temperature-dependent bridge movements. **Journal of Structural Engineering**, ASCE, v. 118, n. 4, p. 1090-1105, 1992.
- MUNOZ, H.; TATSUOKA, F.; HIRAKAWA, D.; NISHIKIORI, H.; SOMA, R.; TATEYAMA, M.; WATANABE, K. Dynamic stability of geosynthetic-reinforced soil integral bridge. **Geosynthetics International**, Thomas Telford, v. 19, n. 1, p. 11-38, 2012.
- MURPHY, B.; YARNOLD, M. Temperature-driven structural identification of a steel girder bridge with an integral abutment. **Engineering Structures**, Elsevier, v. 155, p. 209-221, 2018.

MUSZYNSKI, Z.; WYJADLOWSKI, M. Assessment of the shear strength of pile-to-soil interfaces based on pile surface topography using laser scanning. **Sensors**, MPDI, v. 19, n. 5, p. 1-21, 2019.

NAVAL FACILITIES ENGINEERING COMMAND. **Foundation and earth structures**. Alexandria: Naval Facilities Engineering Command, 1986.

NG, C. W. W.; SPRINGMAN, S. M.; NORRISH, A. R. M. Centrifuge modeling of spread-base integral bridge abutments. **Journal of Geotechnical and Geoenvironmental Engineering**, v. 124, n. 5, p. 376-388, 1998.

OESTERLE, R. G.; TABATABAI, H. Design considerations for integral abutment/jointless bridges in the USA. *In*: 1ST INTERNATIONAL WORKSHOP ON INTEGRAL ABUTMENT/JOINTLESS BRIDGES, 2014, China. **Proceedings** [...]. China: Fuzhou University, 2014.

OLSON, S. M.; HOLLOWAY, K. P.; BUENKER, J. M.; LONG, J. H.; LAFAVE, J. M. **Thermal behavior of IDOT integral abutment bridges and proposed design modifications**. FHWA-ICT-12-022. Urbana: University of Illinois at Urbana-Champaign, 2013.

PAIK, K. H.; SALGADO, R. Estimation of active earth pressure against rigid retaining walls considering arching effects. **Géotechnique**, v. 53, n. 7, p. 643-653, 2003.

PAK, D.; BIGELOW, H.; FELDMANN, M. Design of composite bridges with integral abutments. **Steel Construction**, v. 10, n. 1, p. 23-30, 2017.

PALLA, N.; GUDAVALLI, S.; SUBEDI, B.; JAO, M. Comparison among SPT, CPT and Texas Cone Penetration Test. *In*: ASCE TEXAS SECTION SPRING MEETING, 2008, Texas. **Proceedings** [...]. Texas: ASCE, 2008.

PANAGIOTOU, K. D.; SPILIOPOULOS, K. V. Shakedown analysis of civil engineering structural elements. **Engineering and Computational Mechanics**, ICE, p. 1-9, 2015.

PARASCHOS, A.; AMDE, A. M. A survey on the status of use, problems and costs associated with integral abutment bridges. **Better Roads Magazine**, 2011. Available on: <https://www.semanticscholar.org/paper/A-survey-on-the-status-of-use-%2C-problems-%2C-and-with-Paraschos-Amde/ac5eeb0fe9103244347437a8eac38381f8e46d68>. Access on: Aug 29th, 2019.

PERIC, D.; MILETIC, M.; SHAH, B. R.; ESMAEILY, A.; WANG, H. Thermally induced soil structure interaction in the existing integral bridge. **Engineering Structures**, Elsevier, v. 106, p. 484-494, 2016.

PLAXIS BV. **Plaxis 2D version 2016**. Delft: Plaxis bv, 2016.

POTGIETER, I. C.; GAMBLE, W. L. Nonlinear temperature distributions in bridges at different locations in the United States. **PCI Journal**, p. 80-103, 1989.

POULOS, H. G.; DAVIS, E. H. **Elastic solutions for soil and rock mechanics**. Sydney: John Wiley & Sons, 1974.

RAVJEE, S.; JACOBSZ, S. W.; WILKE, D. N.; GOVENDER, N. Discrete element model study into effects of particle shape on backfill response to cyclic loading behind an integral bridge abutment. **Granular Matter**, Springer v. 20, p. 1-14, 2018.

RAWAT, S.; GUPTA, A. K. Numerical modelling of pullout of helical soil nail. **Journal of Rock Mechanics and Geotechnical Engineering**, CSRME, v. 9, n. 4, p. 648-658, 2017.

RODRIGUEZ L. E.; BARR, P. J.; HALLING, M. W. Temperature effects on a box-girder integral-abutment bridge. **Journal of performance of constructed facilities**, ASCE, v. 28, n. 3, p. 583-591, 2014.

ROESLER, J.; HARDERS, H.; BAEKER, M. **Mechanical behaviour of engineering materials**: metals, ceramics, polymers, and composites. New York: Springer, 2007.

SALKIND, N. J. **Statistics for people who (think they) hate statistics**. 6 ed. Thousand Oaks: SAGE, 2017.

SCHANZ, T.; VERMEER, P. A. Special issue on pre-failure deformation behaviour of geomaterials. **Géotechnique**, ICE, v. 48, p. 383-387, 1998.

SHIU, K. N.; TABATABAI, H. Measured thermal response of concrete box-girder bridge. **Transportation Research Record**, Transportation Research Board, n. 1460, p. 94-105, 1994.

SOLTANI, A. A.; KUKRETI, A. R. Performance evaluation of integral abutment bridges. **Transportation Research Record**, n. 1371, p. 17-25, 1992.

SONG, Z.; XIAO, J.; SHEN, L. On temperature gradients in high-performance concrete box girder under solar radiation. **Advances in Structural Engineering**, Multi-Science Publishing, v. 15, n. 3, p. 399-415, 2012.

STEINBERG, E.; SARGAND, S. M.; BETTINGER, C. Forces in wingwalls of skewed semi-integral bridges. **Journal of Bridge Engineering**, ASCE, v. 9, n. 6, p. 563-571, 2004.

STROUD, M. A.; BUTLER, F. G. The standard penetration test and the engineering properties of glacial materials. *In*: SYMP. ON ENGINEERING PROPERTIES OF GLACIAL MATERIALS, 1975, Birmingham. **Proceedings** [...]. Birmingham: Midland Geotech. Society, 1975.

SUCHSLAND, O.; WOODSON, G. E. **Fiberboard manufacturing practices in the United States**. Washington: Department of Agriculture, 1987.

TATSUOKA, F.; HIRAKAWA, D.; NOJIRI, M.; AIZAWA, H.; NISHIKIORI, H.; SOMA, R.; TATEYAMA, M.; WATANABE, K. A new type of integral bridge comprising geosynthetic-reinforced soil walls. **Geosynthetics International**, Thomas Telford, v. 16, n. 4, p. 301-326, 2009.

TERZAGHI, K. **Theoretical soil mechanics**. New York: John Wiley & Sons, 1943.

THEPCHATRI, T.; JOHNSON, C. P.; MATLOCK, H. **Prediction of temperature and stresses in highway bridges by a numerical procedure using daily weather reports.** FHWA/TX-77-23-1. Austin: The University of Texas at Austin, 1977.

TOMLINSON, M. J. **Pile design and construction practice.** London: E & FN Spon, 1993.

TxDOT. **Geotechnical manual.** Austin: TxDOT, 2020.

TxDOT. **Plans of proposed state highway improvement:** project No. BR 2015 (260) CR 1233 Anderson County. Austin: TxDOT, 2016.

TxDOT. **TxDOT designation: Tex-132-E:** test procedure for Texas Cone Penetration. Austin: TxDOT, 1999.

VASUDEVAN, H. **Evaluation of Texas Cone Penetrometer test to predict undrained shear strength of clays.** 2005. 189 f. Thesis (Master's Degree of Science in Civil Engineering) – The University of Texas at Arlington, Arlington, 2005.

VIPULANANDAN, C.; PUPPALA, A. J.; JAO, M.; KIM, M. S.; VASUDEVAN, H.; KUMAR, P.; MO, Y. L. **Correlation of Texas Cone Penetrometer test values and shear strength of Texas soils:** technical report. TxDOT Project Report No. 0-4861-1 Final Report. Houston: University of Houston, 2008.

WALTER, J. R. **Experimental and numerical investigation of integral/semi-integral bridge abutments for Texas conditions.** 2018. 210 f. Thesis (Master's Degree of Science in Engineering) – The University of Texas at Austin, Austin, 2018.

WHITE, H. **Integral abutment bridges:** comparison of current practice between European countries and the United States of America. FHWA/NY/SR-07/152. New York: New York State Department of Transportation, 2007.

XU, M.; CLAYTON, C. R. I.; BLOODWORTH, A. G. The earth pressure behind full-height frame integral abutments supporting granular fill. **Canadian Geotechnical Journal**, NRC Research Press, v. 44, p. 284-298, 2007.

XU, M.; LIU, P. Response of full-height frame integral abutments subjected to seismic motions. **Soil Dynamics and Earthquake Engineering**, Elsevier, v. 121, p. 356-368, 2019.

XUE, J.; LIN, J.; BRISEGHIELLA, B.; TABATABAI, H.; CHEN, B. Solar radiation parameters for assessing temperature distributions on bridge cross-sections. **Applied Sciences**, MDPI, v. 8, n. 4, p. 1-27, 2018.

YANG, P.; WOLDE-TINSAE, A. M.; GREIMANN, L. F. Effects of predrilling and layered soils on piles. **Journal of Geotechnical Engineering**, ASCE, v. 111, n. 1, p. 18-31, 1985.

ZADEHMOHAMAD, M.; BAZAZ, J. B. Cyclic behaviour of geocell-reinforced backfill behind integral bridge abutment. **International Journal of Geotechnical Engineering**, Taylor & Francis, v. 13, n. 5, p. 438-450, 2019.

ZHENG, X.; PENG, H.; YU, J.; WANG, W.; LIN, W.; XU, J. Analytical ratchet limit for pressurized pipeline under cyclic nonproportional loadings. **Journal of Pipeline Systems Engineering and Practice**, ASCE, v. 8, n. 3, p. 1-8, 2017.

ZORDAN, T.; BRISEGHELLA, B.; LAN, C. Parametric and pushover analyses on integral abutment bridge. **Engineering Structures**, Elsevier, v. 33, p. 502-515, 2011.

ZORNBERG, J. G.; MOFARRAJ, B.; COSTA, Y. SILVA, P. HELWIG, T. **TxDOT project 0-6936**: development of integral/semi-integral abutments for Texas bridges. FY'19 TMB. Austin: The University of Texas at Austin and Texas Department of Transportation, 2019.

ZORZI, G.; ARTONI, R.; GABRIELI, F. Experiments and DEM simulations of granular ratcheting. *In*: POWDERS & GRAINS 2017 - 8TH INTERNATIONAL CONFERENCE ON MICROMECHANICS ON GRANULAR MEDIA, 2017, Montpellier. **Proceedings** [...]. Montpellier: EPJ Web of Conferences, 2017.